



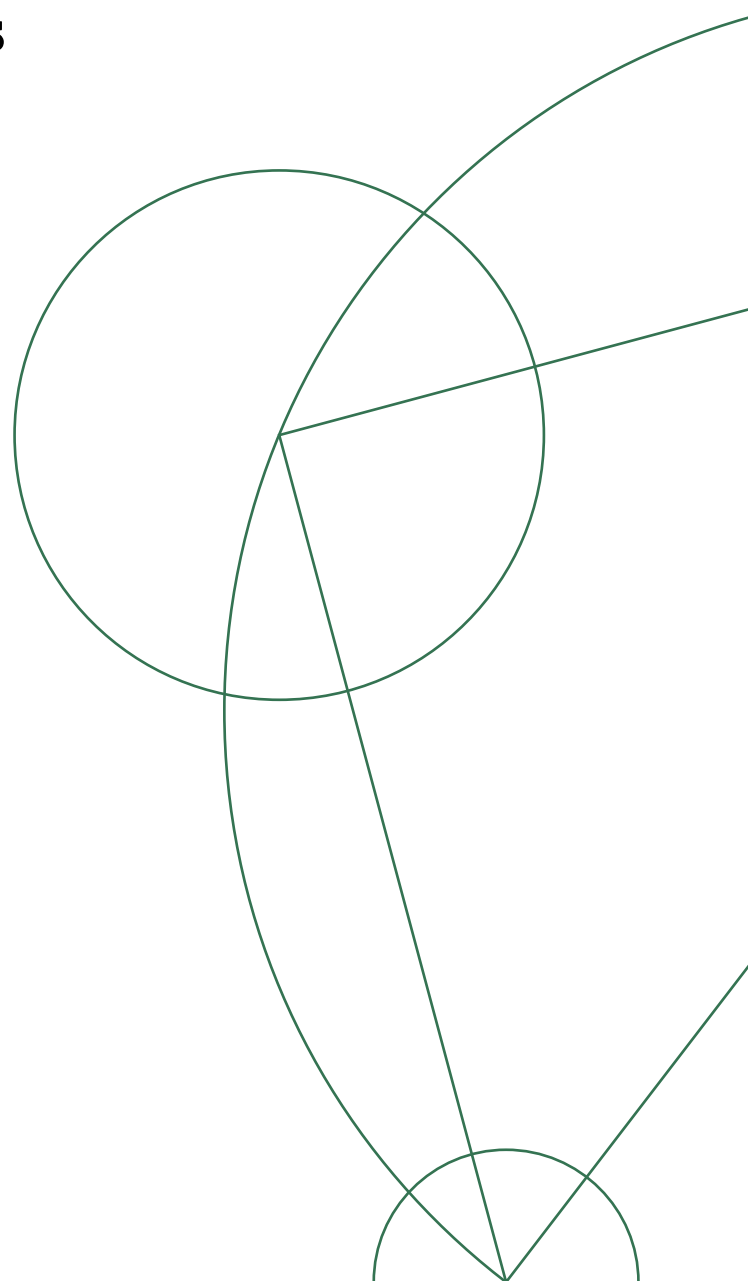
Local and nonlocal differential conductance spectroscopy of Andreev bound states in three-terminal superconducting devices

Anna Birk Hellenes

*Center for Quantum Devices
Niels Bohr Institute
University of Copenhagen*

Master's thesis in Physics
Supervisor: Karsten Flensberg

Dated: September 3, 2019



Edited for web, October 2019 version.

Abstract

In this thesis, we model a three-terminal hybrid semiconductor-superconductor device with analytical and numerical methods. The scattering region consists of a one-dimensional semiconductor, with induced superconductivity. It is attached to a superconducting lead along the wire, and to two normal leads at both ends. Contrary to a two-terminal device, the three-terminal setup allows for current, at one end of the wire, to be correlated with the bias applied between the other end of the wire and the grounded superconducting lead. In other words, the nonlocal conductance, $dI_\alpha/dV_{\bar{\alpha}}$, where $\alpha \neq \bar{\alpha}$ are lead indices for the normal metallic leads, can be non-zero. The scattering matrix formalism for non-interacting, coherent systems is used to calculate the local and nonlocal differential conductance, both analytically and numerically. We find that the differential conductance shows distinct symmetries for three-terminal devices with a superconducting scattering region. The conductance matrix of a single Andreev bound state is probed spectroscopically, and is shown to contain information about the charge at the points where the system is probed. A three-terminal, hybrid device similar to the one modeled in this thesis, was recently fabricated and measured [1]. Complicating effects, such as bias-dependent effective potentials and plunger-dependent sub-gap state energies, may be found in experiment [1] and are not accounted for in the model. The simplicity of the model, however, promotes a more transparent treatment of some, but not all, key physical phenomena in the system. The tools presented in this work, may be helpful in the pursuit of physically realizing (quasi-)Majorana bound states.

Acknowledgements

I want to thank my supervisor, Karsten Flensberg, for helping and challenging me throughout this project. Also, Jeroen Danon was an integral collaborator, and supported me when working on the numerical simulations for the publication together (see below). Furthermore, the condensed matter theory group has been a wonderful environment to spend time in this past year. I thank all its members for that. Special thanks to Gorm Steffensen and Daniel Steffensen, for teaching me about *Mathematica* and for reading parts of my thesis, and to Esben Bork Hansen, for help and insightful discussions. Thanks to Kristofer Björnsson, Raffael Gawatz, Ajit Coimbatore Balram, and Jannis Nikolas Bouchikas. Among other IT and programming-related issues, they used time and effort to get *Kwant* to run on the computer cluster.

Esben Bork Hansen provided me with his already well-developed python package. See his PhD thesis [2] for details. Among many functionalities, the version at the time implemented the Weidenmüller formula for the scattering matrix for a closed system connected to one normal lead. I adapted this part of the code to include two leads, such that the non-local conductance could be calculated.

Publication: Jeroen Danon, Anna Birk Hellenes, Esben Bork Hansen, Lucas Casparis, Andrew P. Higginbotham, Karsten Flensberg. (2019). *Nonlocal conductance spectroscopy of Andreev bound states: Symmetry relations and BCS charges*. ArXiv:1905.05438. (Pre-print as per September 3, 2019.)

Git archive with the scripts used in the numerical work in this thesis, can be found at [3].

Contents

1	Introduction	1
I	Theoretical Background	5
2	Theory of conventional superconductivity	7
2.1	Cooper Instability	7
2.2	BCS theory	9
2.2.1	$u_{\mathbf{k}}$ and $v_{\mathbf{k}}$ for the BCS ground state	11
2.2.2	The BCS quasiparticle density of states	13
3	Theory of normal-superconductor systems	15
3.1	Normal-superconductor proximity effect	15
3.2	BTK theory	20
3.2.1	Andreev Reflection	20
3.2.2	The Bogoliubov-de Gennes equation	23
3.2.3	The NS boundary at equilibrium	24
3.2.4	Probability amplitudes for scattered plane waves	28
3.2.5	Computation of probabilities	29
4	Topological Superconductivity	33
4.1	Properties of Majorana fermions	34
4.2	A p-wave superconductor can host Majorana fermions	34
4.2.1	Energy spectrum	37
4.2.2	Bulk-edge correspondence	39
4.3	The Oreg-Lutchyn model	43
4.3.1	Helical state ($\Delta = \mathbf{0}$)	44
4.3.2	State hosting Majorana fermions	45
4.3.3	Mapping to a p-wave Hamiltonian	47

5	Scattering formalism	51
5.1	Preliminary concepts	51
5.1.1	Mesoscopic systems	51
5.1.2	Transverse modes in conductors	51
5.2	S-matrix and scattering states	54
5.2.1	Definition of the S-matrix	59
5.2.2	Conservation of probability current	61
5.2.3	Calculating the current	64
5.2.4	Scattering states	66
II	Numerical Background	73
6	Tight-binding models and using <i>Kwant</i>	75
6.1	Tight-binding models	75
6.1.1	Nearest-neighbor approximation	75
6.1.2	Tight-binding Hamiltonians mapped onto a graph	79
6.1.3	Discretizing the Hamiltonian using finite differences	80
6.2	Scattering theory in <i>Kwant</i>	81
6.3	Program flow using <i>Kwant</i>	83
7	Diagonalization of a 2D hybrid system using <i>Kwant</i>	87
III	Results	93
8	Nonlocal conductance spectroscopy	95
8.1	Scattering and conductance	96
8.1.1	Scattering matrix	96
8.1.2	Weidenmüller formula for the S-matrix	96
8.1.3	Particle-hole symmetry of the S-matrix	98
8.2	Differential Conductance and its Symmetries	99
8.3	Probing charge by explicit calculation of conductance	101
8.3.1	Single Andreev level	101
8.3.2	Differential conductance spectroscopy	104
8.3.3	1D Oreg-Lutchyn model: Eigenenergy dependencies	106
8.4	Numerical Results	108
8.4.1	Construction of the S-matrix	108
8.4.2	Nonlocal antisymmetric differential conductance	110
8.4.3	Numerical conductance spectroscopy and local BCS charge	111

8.5	Nonlocal conductance simulations using <i>Kwant</i>	113
9	Discussions and Conclusions	115
9.1	Divergent peaks in the ratio $g_{LR}^{0,sym}/g_{LR}^{0,asym}$	115
9.2	Real space considerations	116
9.2.1	A function quantifying the localization of a signal	116
9.2.2	Probability density in real space	119
9.2.3	Spin polarization in real space	121
9.2.4	BCS charge in real space	123
9.2.5	Reconciliation of numerical models: Green's function approach and <i>Kwant</i>	125
9.3	Conclusion	125
9.4	Outlook	127
9.4.1	Including bias-dependence in the S-matrix.	127
9.4.2	Three-terminal model for energies above the gap	129
9.4.3	Implementing tunnel-coupling to the leads in <i>Kwant</i>	130
	Appendices	133
A	BCS theory	135
A.1	Expectation value of the number operator	135
A.2	Variance of the number operator	136
A.3	Explicit form of the free energy	138
A.4	BCS density of states derivation	139
B	BTK theory	141
B.1	Algebraic manipulation leading to eq. (3.28)	141
B.2	Derivation of continuum equation for the probability density current	141
B.3	The explicit probability currents for the scattering processes	142
B.4	The explicit forms of the probability amplitudes	143
C	Second order perturbation	145
D	S-matrix	147

Chapter 1

Introduction

Majorana bound states (MBS) are topologically protected states that localize at the ends of one-dimensional topological superconductors (TSC) [4, 5, 6]. Qubits constructed from these modes [7] can be used to encode and process information in a way that utilizes their quantum nature. Due to their topological protection, MBS are more immune to noise than other traditional qubits, making them more scalable and hence attractive for realizing quantum computers consisting of many qubits.

Topologically protected modes are theoretically predicted to arise in an array of different systems[8, 9, 10, 7, 11, 12]. Fu and Kane[8] proposed depositing a two-dimensional (2D) conventional superconducting layer on top of a three-dimensional (3D) strong (time reversal symmetric and with strong spin-orbit coupling) topological insulator (TI), allowing for tunneling of Cooper pairs in and out of the surface states. By applying a magnetic field, time-reversal symmetry is broken in the TI, by introducing a mass term in the Hamiltonians for both individual systems. By solving the superconducting Hamiltonian, they saw that chiral Majorana edge states form at the TI-superconductor interface. Since then, it was realized that the same types of topological states could be realized, by instead proximitizing a semiconductor with strong Rashba spin-orbit coupling, to a conventional superconductor[13, 5]. The perhaps simplest setup with normal-superconductor (NS) hybrid structures, is placing such a semiconducting, 1D wire, in proximity to a conventional superconductor[11, 12]. The spin-orbit coupling and an external magnetic field creates a gapped, helical energy band. Inside the gap, states are spin-locked to the momentum. In turn, the superconducting pairing couples electrons with opposite momenta, and approximately opposite spin. A gap opens at the Fermi momenta, and an effective, non-conventional superconducting (p -wave) pairing is generated inside the semiconductor. This pairing allows for the formation of *topologically protected* Majorana bound states (MBS). This (Oreg-Lutchyn) model is heavily focused on in this thesis.

A major bottleneck in the field is physically realizing topological modes. One

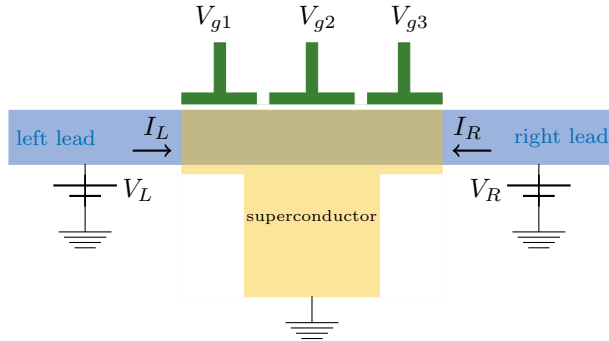


Figure 1.1: A three-terminal device, with a proximitized semiconducting central region connected to left and right normal leads (blue), as well as a grounded superconducting lead (bottom). Local gate voltages (green) and bias voltages (between the left/right leads and ground in the superconducting lead) are independent variables.

proposal that has guided experimental efforts, involves measuring the theoretically predicted zero-bias peaks, resulting from perfect Andreev reflection through the MBS in an N - TSC interface. However, this signature can also persistently emerge from trivial Andreev bound states[14]. By persistent, we imply the state is robust against changes in relevant parameters. Such parameters may include *plunger*, a global gate applied along the system, thus altering the effective chemical potential, *pincher*, which depletes the system from electron in vicinity to a point in real-space, effectively reducing the tunnel-coupling between particles on either side of said point, and the applied magnetic field. A 'smoking-gun' experiment, determining for sure that a Majorana bound state is realized in a system, could instead involve demonstrating the exchange statistics of an array of at least two pairs of Majorana modes. However, this has not been possible yet, which implies that the current experimental setups and techniques need further refinement. This is one of the areas in which theoretical work can have an essential impact on the development of the field.

Structure of thesis

In this thesis, we aim to describe the finer details which can be probed by local and non-local conductance measurements in a three-terminal device shown in figure 1.1. The differential conductance matrix

$$\begin{pmatrix} \frac{dI_L}{dV_L} & \frac{dI_L}{dV_R} \\ \frac{dI_R}{dV_L} & \frac{dI_R}{dV_R} \end{pmatrix} \quad (1.1)$$

contains the local (nonlocal) differential conductances, where the current and the voltage are measured with respect to the same (different) normal lead. With this

matrix, one can gain valuable information about the bound state and the symmetries of the system [1, 15]. We present both theory and numerical simulations to show general symmetries in these conductances. Then, we shift our attention to the detailed spectroscopic information that may be probed in the three-terminal device, where the central region is superconducting. We show how information, of both local and nonlocal natures, can be probed for the emergent near zero-energy modes in the topological superconducting phase: both by analytical, and two numerical approaches to obtaining the conductance matrix.

Part I: Theoretical background. In the first part, we build a conceptual basis needed to model the three-terminal device, namely superconductivity (ch. 2) and the proximity effect (ch. 3.1), the scattering taking place in an NS junction (ch. 3.2), the emergence of topologically protected states in a p -wave superconductor (ch. 4.3.3), and the Landauer-Büttiker scattering formalism (ch. 5) for a superconductor connected by normal leads. From the point of view of the systems being considered, the complexity increases with the progression throughout these chapters: we start with only the superconductor, then consider it together with a normal metal, and lastly, with two normal leads and one superconducting lead.

Part II: Numerical background. We start by introducing the concept of discretizing Hamiltonians. This enables one to encode the continuum Hamiltonian of interest, as a discrete matrix. In turn, we can use powerful numerical tools, such as the *Kwant* package for the *Python* language, to calculate the eigenenergies of the closed system, as well as the scattering matrix of the open system. We outline how to 'build' a scattering region, with leads attached, using *Kwant*, from which the scattering matrix and the differential conductance matrix is calculated using said package. At the end, we do a case study to see if we can reproduce the eigenenergies obtained in a previously published article[7], for a specific quasi one-dimensional topological system.

Part III: Results. The results consists of both analytical and numerical work. The general symmetries of the differential conductance matrix are presented first. Then, we describe differential conductance spectroscopy of a single Andreev bound state in the three-terminal device in figure 1.1, for biasenergies close to the bound state energy. The S-matrix is calculated numerically, by implementing the Weidenmüller formula, but also using the *Kwant* package. The majority of the presented numerical data, are obtained with the former implementation. These data include the spectroscopic details obtained analogously to in the analytical analysis. We discuss what local and non-local information can be probed with these calculations.

Part I

Theoretical Background

Chapter 2

Theory of conventional superconductivity

We start this thesis by establishing some results from Bardeen–Cooper–Schrieffer (BCS) theory, which are important for understanding what types of scattering are allowed at interfaces between non-interacting normal metals and superconductors. We introduce the Cooper instability that may occur in an electron gas, with both Coulomb and phonon-interactions. We argue that, no matter how small the effective interaction is, the scattering amplitude between time-reversed electrons of opposite spins can blow up when approaching a critical temperature from above. This is used to motivate the mean-field approach, proposed by BCS. Afterwards, we present some key results from this mean-field theory: The gapped energy spectrum in the superconducting phase, below which no *quasiparticle* excitations occur. The probability amplitudes (*coherence factors*) specifying the BCS ground state, which consists of a coherent condensation of an integer number of Cooper pairs. The quasiparticle density of states.

2.1 Cooper Instability

For frequencies lower than a certain threshold, phonons in an interacting electron gas, can induce an effectively attractive interaction between electrons. This attractive interaction is the renormalized interaction $V_{\text{eff}}^{\text{RPA}}$ in the random phase approximation (RPA). (In order for RPA to be valid, the electron density needs to be high¹.) As a result, the scattering vertex Λ diverges when electrons with momentum and spin $|\mathbf{k} \uparrow\rangle$ repeatedly scatter with their time-reversed state $|-\mathbf{k} \downarrow\rangle$, in turn giving rise to

the Cooper instability. When does this vertex diverge?

Consider the explicit form of the scattering vertex $\Lambda(\tilde{k}, \tilde{p})$, or pair interaction, between electrons with incoming momentum and frequency (\mathbf{k}, ik_n) (or four-momentum \tilde{k}), and the out-going ones with four-momentum \tilde{p} . The dominant terms are the ladder diagrams, where only time-reversed pairs of propagators interact[16, sec. 17.3.1, eq. (17.40)]:

$$(2.1)$$

Each scattering vertex conserve spin and four-momentum, and the direction of time is from left to right. The free propagators with spin σ and dispersion $\epsilon_{\mathbf{k}}$,

$$\mathcal{G}_{\sigma}^0(\tilde{k}) = \begin{array}{c} \longrightarrow \\ \tilde{k} \sigma \end{array} = \frac{1}{ik_n - \epsilon_{\mathbf{k}}}, \quad (2.2)$$

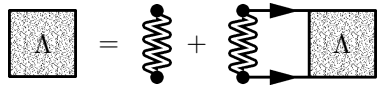
can interchange momentum via the effective, RPA-renormalized interaction $V_{\text{eff}}^{\text{RPA}}(\tilde{q})$. The RPA result[16, eq. (17.28)], an infinite sum of incoming and outgoing single, bare phonon interaction lines $V_{\text{eff}}^0(\tilde{q})$ connected by pair-bubbles with bare phonon lines in between, can be re-collected into two different contributions as[16, eq. (17.39)]

$$\begin{array}{c} -V_{\text{eff}}^{\text{RPA}}(\tilde{q}) \\ \text{---} \end{array} = \begin{array}{c} -W^{\text{RPA}}(\mathbf{q}) \\ \text{---} \end{array} + \begin{array}{c} -\frac{1}{\nu} |g_{\mathbf{q}}^{\text{RPA}}|^2 \mathcal{D}^{\text{RPA}}(\tilde{q}) \\ \text{---} \end{array} \quad (2.3)$$

Every four-momentum index \tilde{q} is internal. The first contribution in eq. (2.3), $W^{\text{RPA}}(\mathbf{q})$, is the effective, screened Coulomb interaction, which is a sum of all diagrams where the incoming and outgoing lines, as well as all lines connecting the pair-bubbles, are Coulomb interaction lines. All other terms in $V_{\text{eff}}^{\text{RPA}}(\tilde{q})$ are collected into $\frac{1}{\nu} |g_{\mathbf{q}}^{\text{RPA}}|^2 \mathcal{D}^{\text{RPA}}(\tilde{q})$. The right vertex $g_{\mathbf{q}}^{\text{RPA}}$, is the sum over all diagrams between the outgoing vertex on the right and the first phonon line (time going from left to right). Similarly, the sum over diagrams between incoming vertices on the left and the last phonon line is the left vertex $[g_{\mathbf{k}}^{\text{RPA}}]^*$. $\mathcal{D}^{\text{RPA}}(\tilde{k})$ is the sum of all diagrams in between the first and the last phonon lines. Its solution is the RPA renormalized phonon interaction[16, eq. (17.33)]. The solution to $V_{\text{eff}}^{\text{RPA}}$ is given by the second line in eq. (2.3), where $\omega_{\mathbf{q}}$ is the RPA-screened phonon frequency[16, p.321]. Suppressing

¹In an interacting electron gas, the radius of a sphere containing exactly one electron goes as[16, p.41] $r_s \propto k_F^{-1}$, which in turn can be used to identify the most important diagrams for every order in the high-density limit[16, Ch.14.1].

the external fermion lines and indices, the vertex itself is given by the solution to the Dyson equation



$$\Lambda = \text{wavy line} + \text{wavy line} \rightarrow \Lambda \quad (2.4)$$

Only *deviations* from the Coulomb interaction should contribute to an instability. Furthermore, the density of state of acoustic phonons go as their frequency squared, $\sim \omega_{ph}^2$, below the Debye frequency, and is otherwise zero. We assume the attractive interaction is a constant $-V$ below the Debye frequency. The difference $V_{eff}^{RPA} - W_{eff}^{RPA}$, see figure 2.1a, rapidly approaches zero above said frequency. Thus, we approximate the effective interaction as

$$V_{eff}^{RPA}(\mathbf{q}, iq_n) \approx \begin{cases} -V, & |iq_n| < \omega_D \\ 0 & |iq_n| > \omega_D. \end{cases} \quad (2.5)$$

Inserting for this interaction in the Dyson equation², one obtains

$$\Lambda = \frac{V}{1 - \frac{V}{\beta} \sum_{|iq_n| < \omega_D} \frac{1}{v} \sum_{\mathbf{q}} \mathcal{G}_{\uparrow}^0(\tilde{q}) \mathcal{G}_{\downarrow}^0(-\tilde{q})}. \quad (2.6)$$

For high temperatures $\beta \ll \hbar\omega_D$, the pair interaction reduces to the strength of the attractive interaction in eq. (2.5). However, lowering the temperature, the denominator in eq. (2.6) can approach zero from above: *there exists a critical temperature $\propto 1/\beta_c$ for which the denominator of Λ becomes arbitrarily small, giving rise to the Cooper instability.*

2.2 BCS theory

As a result of the Cooper instability, the Fermi surface of a normal metal destabilizes. This is sketched in figure Below the critical temperature, electrons pair up in Cooper pairs. The correlation function $\langle c_{\mathbf{k}\uparrow}^{\dagger} c_{-\mathbf{k}\downarrow}^{\dagger} \rangle \neq 0$ between these electrons are thus non-zero in the superconducting phase. Because perturbation theory is not applicable, BCS[17] proposed to make a mean-field theory instead. Consider the new ground state BCS proposed, namely

$$|\psi_{BCS}\rangle = \prod_{\mathbf{k}} \left(u_{\mathbf{k}} + v_{\mathbf{k}} c_{\mathbf{k}\uparrow}^{\dagger} c_{-\mathbf{k}\downarrow}^{\dagger} \right) |0\rangle, \quad (2.7)$$

²The vertex itself is frequency independent, with the approximation in eq. (2.5). On the left side in eq. (2.4), the vertex is thus $\Lambda(\mathbf{k}, \mathbf{p})$. On the right hand side, the internal momenta \mathbf{k}' are summed over, and the vertex is $\Lambda(\mathbf{k}', \mathbf{p})$. Firstly, since the summation on the right hand side does not contain the external momentum, \mathbf{k} , the left-hand side is $\Lambda(\mathbf{k}, \mathbf{p}) = \Lambda(\mathbf{p})$. At this point, the \mathbf{p} -dependence is only found in $\Lambda(\mathbf{p})$. Therefore, a self-consistent solution can be found by taking Λ to be a constant.

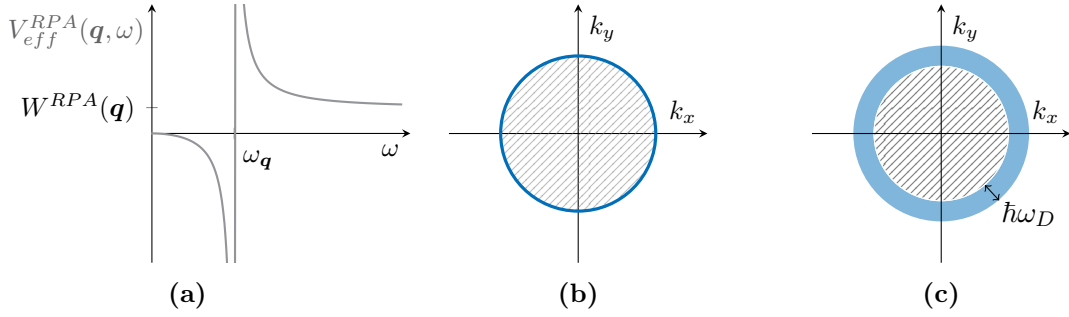


Figure 2.1: (a) For energies below the Debye frequency, V_{eff}^{RPA} is attractive. (b) States are filled up to the Fermi surface (blue circle) of two-dimensional electron gas. This surface destabilizes in a small energy range around the Fermi energy, sketched in (c).

where $u_{\mathbf{k}}$ and $v_{\mathbf{k}}$ are expansion coefficients. Each factor in the product over \mathbf{k} , represent states containing an integer number of Cooper pairs. Because the number of Cooper pairs is not deterministic (see appendix A.2 which shows that the variance of the number operator is non-zero when measured by the BCS ground state), the superconductor should be thought of as being in contact with an electron reservoir, which allows for fluctuations in the number of Cooper pairs.

Consider a Fermi liquid, with or without the pair interaction. The effective Hamiltonian modeling the system is

$$H_{BCS} = \sum_{\mathbf{k}\sigma} \xi_{\mathbf{k}} c_{\mathbf{k}\sigma}^\dagger c_{\mathbf{k}\sigma} + \sum_{\mathbf{k}\mathbf{k}'} V_{\mathbf{k}\mathbf{k}'} c_{\mathbf{k}\uparrow}^\dagger c_{-\mathbf{k}\downarrow}^\dagger c_{-\mathbf{k}'\downarrow} c_{\mathbf{k}'\uparrow}. \quad (2.8)$$

Being a Fermi liquid, first term annihilates and creates an electron quasiparticle with a well-defined kinetic energy $\xi_{\mathbf{k}} = \frac{\hbar^2 k^2}{2m} - \mu$, if and only if the quasiparticle state with momentum and spin (\mathbf{k}, σ) is occupied in the gas. If we turn on the effective phonon-mediated interaction $V_{\mathbf{k}\mathbf{k}'}$, Cooper pairs with energies near the Fermi surface (within $|\xi_{\mathbf{k}}| < \hbar\omega_D$) couple. The second term describes scattering of one Cooper pair, $(\mathbf{k}' \uparrow, -\mathbf{k}' \downarrow)$, into another pair, $(\mathbf{k} \uparrow, -\mathbf{k} \downarrow)$. In other words, instead of the initial pair evaporating, it stays within the condensate due to this scattering.

The mean-field approximation of eq. (2.8) is perfectly fine to perform, as long as we can expand in small deviations in

$$c_{\mathbf{k}\uparrow}^\dagger c_{-\mathbf{k}\downarrow}^\dagger - \langle c_{\mathbf{k}\uparrow}^\dagger c_{-\mathbf{k}\downarrow}^\dagger \rangle.$$

Performing the mean-field approximation with the Hamiltonian eq. (2.8) yields

$$H_{BCS}^{MF} = \sum_{\mathbf{k}\sigma} \xi_{\mathbf{k}} c_{\mathbf{k}\sigma}^\dagger c_{\mathbf{k}\sigma} - \sum_{\mathbf{k}} \left(\Delta_{\mathbf{k}} c_{\mathbf{k}\uparrow}^\dagger c_{-\mathbf{k}\downarrow}^\dagger + \Delta_{\mathbf{k}}^* c_{-\mathbf{k}\downarrow} c_{\mathbf{k}\uparrow} \right) \quad (2.9)$$

$$= \sum_{\mathbf{k}} \boldsymbol{\alpha}_{\mathbf{k}}^\dagger \begin{pmatrix} \xi_{\mathbf{k}} & -\Delta_{\mathbf{k}} \\ -\Delta_{\mathbf{k}}^* & -\xi_{-\mathbf{k}} \end{pmatrix} \boldsymbol{\alpha}_{\mathbf{k}}. \quad (2.10)$$

The superconducting order parameter

$$\Delta_{\mathbf{k}} = - \sum_{\mathbf{k}'} V_{\mathbf{k}\mathbf{k}'} \langle c_{-\mathbf{k}'\downarrow} c_{\mathbf{k}'\uparrow} \rangle, \quad (2.11)$$

has been introduced, and the constant $-\sum_{\mathbf{k}\mathbf{k}'} V_{\mathbf{k}\mathbf{k}'} \langle c_{\mathbf{k}\uparrow}^\dagger c_{-\mathbf{k}\downarrow}^\dagger \rangle \langle c_{-\mathbf{k}'\downarrow} c_{\mathbf{k}'\uparrow} \rangle$ is absorbed into the chemical potential. In the second line, the Hamiltonian is written the electron-hole (Nambu) basis, having introduced the Nambu spinors $\boldsymbol{\alpha}_{\mathbf{k}}^\dagger = (c_{\mathbf{k}\uparrow}^\dagger, c_{-\mathbf{k}\downarrow})$ and its Hermitian conjugate, $\boldsymbol{\alpha}_{\mathbf{k}}$. The first (second) component of $\boldsymbol{\alpha}_{\mathbf{k}}^\dagger$ creates an electron with $\mathbf{k} \uparrow$ (annihilates an electron, or creates a hole, with $-\mathbf{k} \downarrow$).

The energy spectrum is

$$E_{\mathbf{k}} = \pm \sqrt{\xi_{\mathbf{k}}^2 + |\Delta_{\mathbf{k}}|^2}. \quad (2.12)$$

There are two energy solutions for every momentum \mathbf{k} , one for electrons, and another with opposite sign for the corresponding holes. The spectrum is shown in figure 2.2. If $|\Delta_{\mathbf{k}}| \neq 0$, a gap of size $|\Delta_{\mathbf{k}}|$ opens in the energy spectrum at $\mathbf{k} = 0$. This gap, also

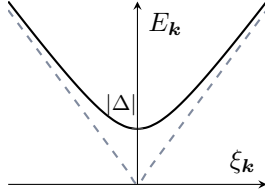


Figure 2.2: The energy spectrum of quasiparticles in a superconductor (solid black line) has a gap Δ at the Fermi energy ($\xi_{\mathbf{k}} = 0$). Letting the gap go to zero yields the electron spectrum of a normal metal (dashed line).

referred to as the superconducting gap, distinguishes superconductors from normal metals. In the latter, quasiparticles have energies $\xi_{\mathbf{k}}$ (dashed line in figure 2.2). In the superconductor, single particles are not allowed to have energies smaller than $|\Delta|$, which is also evident from the density of states (see section 2.2.2).

2.2.1 $u_{\mathbf{k}}$ and $v_{\mathbf{k}}$ for the BCS ground state

So far, we do not know much about the probability amplitudes, $u_{\mathbf{k}}$ and $v_{\mathbf{k}}$, in the proposed BCS ground state. These factors are key to understand the analytical and

numerical work in chapter 8. Therefore, we devote this section to determining their explicit energy dependence. We build upon our knowledge from the current chapter, when the normal-superconductor junction is described later (see chapter 3.2).

The same technique as is used for calculating the variance in the number operator, can be employed in finding an explicit form of the free energy

$$F \equiv \langle \psi_{BCS} | H_{BCS}^{MF} | \psi_{BCS} \rangle, \quad (2.13)$$

Without loss of generality, we parametrize the amplitudes as $u_{\mathbf{k}} = \sin(\theta_{\mathbf{k}})$ and $v_{\mathbf{k}} = \cos(\theta_{\mathbf{k}})$, and minimize the free energy with respect to the parameter $\theta_{\mathbf{k}}$. This calculation is detailed in appendix A.3 for $\mu = 0$. Re-inserting for a non-zero chemical potential yields

$$u_{\mathbf{k}}^2 = \frac{1}{2} \left(1 + \frac{\xi_{\mathbf{k}}}{E_{\mathbf{k}}} \right), \quad v_{\mathbf{k}}^2 = \frac{1}{2} \left(1 - \frac{\xi_{\mathbf{k}}}{E_{\mathbf{k}}} \right), \quad (2.14)$$

which are plotted as functions of the energy dispersion in figure 2.3 (with $\epsilon_{\mathbf{k}} = \xi_{\mathbf{k}} - \epsilon_F$). Interestingly, the variance in the number operator (see eq. (A.8)) is given by the sum, over \mathbf{k} , of all factors $|u_{\mathbf{k}}|^2 |v_{\mathbf{k}}|^2$.

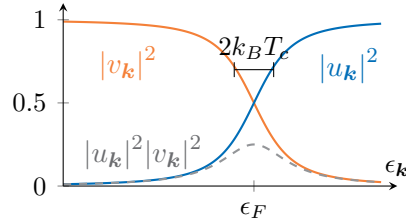


Figure 2.3: The BCS factors (blue and orange lines) as a function of energy. The variance in the number operator (gray) peaks at the fermi energy.

For energies $\epsilon_{\mathbf{k}} > \epsilon_F + (-)$ a few $k_B T_c$, the \mathbf{k} 'th component of the BCS state is dominated by the $u_{\mathbf{k}}$ ($v_{\mathbf{k}}$)-term. In the vicinity of the Fermi energy, $\epsilon_{\mathbf{k}} = \epsilon_F \pm$ a few $k_B T_c$, the variance in the number operator is significant. This is also the region where Cooper pairs prefer to form. Due to energy conservation, the difference between the quasiparticle energy $\epsilon_{\mathbf{k}}$ and the Fermi energy is necessarily the binding energy of a Cooper pair³. For the relevant value of \mathbf{k} , the BCS ground state is largely in a superposition of: one Cooper pair, with the probability amplitude $v_{\mathbf{k}}$, and no Cooper pair, with the amplitude $u_{\mathbf{k}}$.

³The binding energy is given by the energy gained when a Cooper pair is added outside a filled Fermi sea.

2.2.2 The BCS quasiparticle density of states

Not all electrons are necessarily bound in Cooper pairs below the critical temperature. Single electron or holes may excite out of the condensate. We describe such (Bogoliubov) quasiparticle excitations as a superposition of electron and hole degrees of freedom:

$$\gamma_{\mathbf{k}}^{\dagger} = u_{\mathbf{k}}c_{\mathbf{k}\uparrow}^{\dagger} - v_{\mathbf{k}}c_{-\mathbf{k}\downarrow}. \quad (2.15)$$

The number of quasiparticle states, n , per unit energy, ω (specified relative to the Fermi energy), is

$$\frac{d(\omega)}{d(0)} = \frac{\omega}{\sqrt{\omega^2 - |\Delta|^2}} \Theta(\omega - |\Delta|) \quad (2.16)$$

as is shown in figure 2.4. The derivation of eq. (2.16) is outlined in appendix A.4.

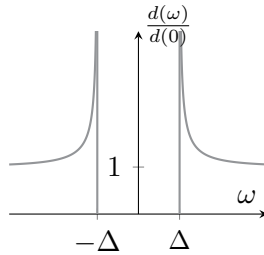


Figure 2.4: Quasiparticle density of states in a superconductor with superconducting gap Δ , as a function of energy ω .

$d(0) = \frac{dk/(2\pi)^d}{d\xi_k}$ is the density of state of a non-interacting normal metal ($\Delta_k = 0$) at the Fermi energy in d dimensions. For energies below the superconducting gap ($\omega < |\Delta|$), there are no available quasiparticle states. At the gap, also referred to as the 'gap edge' in chapter 3.2, the DOS exhibits a discontinuous peak. For quasiparticle energies $|\omega| > \Delta$, it decreases monotonically towards the asymptotic value $d(0)$. The density of states has important consequences scattering in normal-superconductor interfaces, because it implies:

Single-particle states cannot scatter into a superconductor for sub-gap energies.

This is explored in detail in chapter 3.2.

Chapter 3

Theory of normal-superconductor systems

The system of interest in this thesis is a hybrid system. The setup is illustrated in figure 1.1. In this chapter, we turn our attention to two different sub-components of the three-terminal device:

1. The central region, consisting of a semiconducting wire in proximity to an *s-wave* (conventional) superconductor.
2. The interfaces between the central region and the normal leads.

When we consider the Landauer-Büttiker formalism, and numerical transport simulations in chapters 5 and 6, the pictures we think of are similar to what we will see in the current chapter. With *Kwant*, we implement scattering between normal and superconducting leads, analogously to in BTK theory: with a potential barrier at the interface, and solving the scattering problem for this barrier. The proximity effect 'picture' works differently. In essence, we solve for the Green's function inside the normal metal, by integrating out the degrees of freedom of the superconductor. The effect from the proximity to the superconductor is implicitly included in a self-energy. In the Landauer-Büttiker formalism, the situation is similar. We treat the central scattering region as a (coherent) 'black box', and only compare wavefunctions in the leads.

3.1 Normal-superconductor proximity effect

Consider a thin semiconductor placed in proximity to a superconductor as illustrated in figure 3.1. By thin, we imply that: if an electron in the semiconductor moves with a

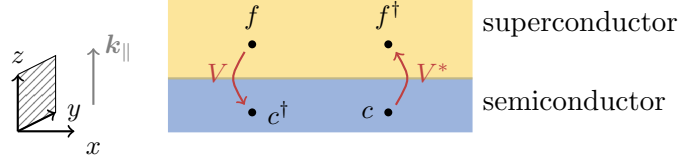


Figure 3.1: Picture of a semiconductor in proximity to a superconductor. Close to the interface between the two, tunneling may take place. Tunneling can be described as the annihilation of one fermion (c in the semiconductor, or f in the superconductor), and creation of another fermion in the adjacent conductor (f^\dagger with the tunneling amplitude V^* , and c^\dagger with the amplitude V). \mathbf{k}_\parallel is perpendicular to the x -axis, and is specified in the indicated $y - z$ plane.

momentum \mathbf{k}_\parallel , perpendicular to the longitudinal axis of the semiconductor, and if the quasiparticle density of states in the superconductor is non-zero, the electron has a tendency to exit the semiconductor via tunneling into the superconductor. The total Hamiltonian of the superconductor and semiconductor is modelled as the sum of the Hamiltonians of the individual systems, H_N and H_S , and a tunneling Hamiltonian, H_T :

$$H = H_N + H_S + H_T. \quad (3.1)$$

Denote the fermion operator of the superconductor by f , and that of the semiconductor by c . The superconducting Hamiltonian is given by the mean-field BCS Hamiltonian (see eq. (2.9)), while the tunneling term depends on a tunneling potential V . In sum,

$$H_N = \sum_{k_x, \sigma} (\epsilon_{k_x} - \mu) c_{k_x, \sigma}^\dagger c_{k_x, \sigma}, \quad \text{where } \epsilon_{k_x} = \frac{\hbar^2 k_x^2}{2m^*}, \quad (3.2)$$

$$H_S = \sum_{\mathbf{k}, \sigma} \xi_{\mathbf{k}} f_{\mathbf{k}, \sigma}^\dagger f_{\mathbf{k}, \sigma} - \sum_{\mathbf{k}} \left(\Delta_{\mathbf{k}} f_{\mathbf{k}, \uparrow}^\dagger f_{-\mathbf{k}, \downarrow}^\dagger + h.c. \right), \quad \text{where } \xi_{\mathbf{k}} = \frac{\hbar^2 k^2}{2m} - \mu, \quad (3.3)$$

and

$$H_T = \frac{1}{\sqrt{\mathcal{A}}} \sum_{\mathbf{k}, \sigma} \left(V c_{k_x, \sigma}^\dagger f_{k_x, \mathbf{k}_\parallel, \sigma} + h.c. \right). \quad (3.4)$$

The chemical potential μ is taken to be the same for both conductors. Inside the semiconductor, particles may assume the momentum k_x , while \mathbf{k} is the momentum vector in the superconductor in three spatial dimensions. \mathcal{A} is the normalization volume associated with the sum over momenta. $\Delta_{\mathbf{k}}$ is the superconducting order parameter, and $\xi_{\mathbf{k}}$ is the energy of the quasiparticle excitations in the superconductor,

with the notation $k = |\mathbf{k}|$. The creation and annihilation operators create and annihilate electronic states, with the momenta and spins given by the momentum indices and the spin index σ . The effective mass in the semiconductor, m^* , is usually one or two orders of magnitude smaller than the free electron mass, m_e . For instance, the mass of an *InAs* semiconductor is $0.026 m_e$ [18]. The effective mass, m , in the superconductor is typically larger. For instance, the effective mass in *Al* is the order of m_e [19].

Assuming the system is translationally invariant in the x -direction, the tunneling Hamiltonian conserves momentum k_x . Typically, the quasiparticle DOS of the superconductor, is much larger than that of the semiconductor for energies $E \gtrsim \Delta$ (see figure 2.4). This implicitly puts a restriction on what transverse momenta, \mathbf{k}_\parallel , will allow for particle tunneling. Therefore, we do not usually have to consider restricting the sum over \mathbf{k}_\parallel in this type of hybrid system.

Define two (Nambu) spinors, for the semiconducting and superconducting fermion operators, as

$$C_{k_x} = \begin{pmatrix} c_{k_x \uparrow} \\ c_{-k_x \downarrow}^\dagger \end{pmatrix}, \quad F_{\mathbf{k}} = \begin{pmatrix} f_{\mathbf{k} \uparrow} \\ f_{-\mathbf{k} \downarrow}^\dagger \end{pmatrix}. \quad (3.5)$$

In this basis, the Hamiltonians in eqs. (3.2) through (3.4) can be rewritten as

$$H_N = \sum_{k_x} C_{k_x}^\dagger \begin{pmatrix} \epsilon_{k_x} - \mu & 0 \\ 0 & -\epsilon_{k_x} + \mu \end{pmatrix} C_{k_x}, \quad (3.6)$$

$$H_S = \sum_{\mathbf{k}} F_{\mathbf{k}}^\dagger \begin{pmatrix} \xi_{\mathbf{k}} & -\Delta_{\mathbf{k}} \\ -\Delta_{\mathbf{k}}^* & -\xi_{\mathbf{k}} \end{pmatrix} F_{\mathbf{k}}, \quad (3.7)$$

$$H_T = \frac{1}{\mathcal{A}} \sum_{\mathbf{k}} C_{k_x}^\dagger \begin{pmatrix} V & 0 \\ 0 & -V^* \end{pmatrix} F_{\mathbf{k}} + F_{\mathbf{k}}^\dagger \begin{pmatrix} V^* & 0 \\ 0 & -V \end{pmatrix} C_{k_x}. \quad (3.8)$$

As a result of being in proximity to the superconductor, it can be shown that the full semiconductor Green's function is 'dressed' by tunneling-interactions, which is encoded in a self-energy. In the following, we derive this full Green's function, by constructing a Dyson equation that accounts for all scattering events starting and ending in the semiconductor.

The bare semiconductor and superconductor Green's functions in Nambu-space, are given by the time-ordered correlation functions

$$\mathcal{G}_S^0(\mathbf{k}, \tau) = -\langle T_\tau F_{\mathbf{k}}(\tau) \otimes F_{\mathbf{k}}^\dagger(0) \rangle, \quad \mathcal{G}_N^0(\mathbf{k}, \tau) = -\langle T_\tau C_{k_x}(\tau) \otimes C_{k_x}^\dagger(0) \rangle,$$

where T_τ is the time-ordering operator. The off-diagonal terms allow for non-zero correlations between fermionic degrees of freedom, with opposite spin and momentum.

From equation of motion (EOM) theory, their explicit form is

$$\mathcal{G}_N^0(k_x, ik_n) = [ik_n \mathbf{1} - (\epsilon_{k_x} - \mu)\tau_z]^{-1} \quad (3.9)$$

$$\mathcal{G}_S^0(\mathbf{k}, ik_n) = \frac{1}{(ik_n)^2 - E_k^2} \begin{pmatrix} ik_n + \xi_k & \Delta_{\mathbf{k}}^* \\ \Delta_{\mathbf{k}} & ik_n - \xi_k \end{pmatrix}. \quad (3.10)$$

Proving this, for instance for $\mathcal{G}_S^0(\mathbf{k}, ik_n)$, involves Fourier-transforming¹ the EOM²

$$\partial_\tau \mathcal{G}_S^0(\mathbf{k}, \tau) = -\delta(\tau) \mathbf{1} - \begin{pmatrix} \xi_k & -\Delta_{\mathbf{k}} \\ -\Delta_{\mathbf{k}}^* & -\xi_k \end{pmatrix} \mathcal{G}_S^0(\mathbf{k}, \tau),$$

and solving it for the Green's function by inverting a 2×2 matrix. The analysis can be done similarly for $\mathcal{G}_N^0(k_x, ik_n)$.

The free Green's functions (propagators) are represented by single fermion lines in the Feynman diagrams that follow. We write the Dyson equation for the full Green's function in the semiconductor, signified by double lines, as the sum over all single particle scattering events that start and end inside the normal metal. In the notation used here, we assume a picture where we do not have to explicitly write out electron and hole lines separately. Each line represents either an electron or a hole, each with four possible combinations of spin (up/down) and momentum (positive and negative). Thus, it is implied in the notation that all possible combinations of incoming electrons and holes are accounted for.

Single lines combining the scattering vertices V on the left and V^\dagger on the right, are fermion excitations (*Bogoliubons*, see eq. (2.15)) inside the superconductor. These fermionic excitations are composed by an electron and a hole component with opposite spin and momentum. The correlation between electrons and holes is mediated by Cooper pairs, described by the superconducting pairing potential (see eq. (2.11)). With these rules in place, we write the Dyson equation for the full Green's function

¹Performing a Fourier transform (FT) into frequency space, $\partial_\tau \xrightarrow{FT} -ik_n$ ($\hbar = 1$) and $\delta(\tau) \xrightarrow{FT} 1$

²Write out the derivative of $\mathcal{G}_S^0(\mathbf{k}, ik_n)$, using the product rule. The derivative of the time-ordering operator is a Dirac-delta function $\delta(\tau)$, while that of the fermion operator in Nambu space is given by the commutator $i\partial_\tau F_{\mathbf{k}}(\mathbf{k}, \tau) = -[H_{BCS}^{MF}, F_{\mathbf{k}}](\tau)$.

in the normal metal as

$$\begin{aligned}
\begin{array}{c} \text{\scriptsize (N)} \\ \blacktriangleleft\blacktriangleleft \end{array} &= \blacktriangleleft\blacktriangleleft + \blacktriangleleft\star\blacktriangleleft\star\blacktriangleleft + \blacktriangleleft\star\blacktriangleleft\star\blacktriangleleft\star\blacktriangleleft + \dots \\
&= \blacktriangleleft\blacktriangleleft + \blacktriangleleft\star\blacktriangleleft\star\left(\blacktriangleleft\blacktriangleleft + \blacktriangleleft\star\blacktriangleleft\star\blacktriangleleft + \dots \right) \\
&= \blacktriangleleft\blacktriangleleft + \blacktriangleleft\star\blacktriangleleft\star\blacktriangleleft\blacktriangleleft \\
\begin{array}{c} \text{\scriptsize (N)} \\ \blacktriangleleft\blacktriangleleft \end{array} &= \left[\left(\blacktriangleleft\blacktriangleleft \right)^{-1} - \begin{array}{c} \text{\scriptsize (S)} \\ \star\blacktriangleleft\star \end{array} \right]^{-1}
\end{aligned} \tag{3.11}$$

with the direction of time from right to left, and where the time-reversal of holes, compared to electrons, is implied in the notation³. Explicitly, eq. (3.11) is

$$\mathcal{G}_N(k_x, ik_n) = \frac{1}{[\mathcal{G}_N^0(k_x, ik_n)]^{-1} - \Sigma_{ss}(k_x, ik_n)} \tag{3.12}$$

where

$$\Sigma_{ss}(k_x, ik_n) = \frac{1}{\mathcal{A}} \sum_{\mathbf{k}_{\parallel}} V \mathcal{G}_S^0(\mathbf{k}, ik_n) V^\dagger. \tag{3.13}$$

$\Sigma_{ss}(k_x, ik_n)$ is a self-energy, which incorporates the energy renormalization that takes place in the semiconductor. This extra energy is a direct consequence of the fact that tunneling may take place between the metals.

Inserting for eq. (3.10) in eq. (3.13), the explicit form of the self-energy reads

$$\sum_{ss}(\mathbf{k}, ik_n) = d(0)|V|^2 \int_{-\infty}^{\infty} d\xi_k \frac{1}{k_n^2 + E_k^2} \begin{pmatrix} -ik_n & \Delta_{\mathbf{k}} e^{2i\phi} \\ \Delta_{\mathbf{k}}^* e^{-2i\phi} & -ik_n \end{pmatrix} \tag{3.14}$$

$$= \frac{\Gamma}{2} \frac{-ik_n \mathbf{1} + \Delta_{\mathbf{k}} \tau_x}{\sqrt{|\Delta|^2 - (ik_n)^2}}, \quad \text{where } \Gamma = 2\pi d(0)|V|^2 \tag{3.15}$$

is the tunneling energy formulated as Fermi's golden rule. The tunneling strength is defined as $V = |V|e^{i\phi}$, where ϕ is a phase, and $d(0)$ is the density of states of the superconductor at the Fermi level. In the first equality, we convert the sum over \mathbf{k}_{\parallel} in eq. (3.13) to an integral over ξ_k running from $-\infty$ to ∞ (as in eq. (A.16), now with \mathcal{A} being the normalization volume). The diagonal terms ξ_k from eq. (3.10)

³That is, we do not explicitly draw arrows in the opposite direction of what is shown here, to signify the hole propagators.

integrated over yields zero, and are thus omitted. In the second equality, we perform the integration, assigning $\Delta_{\mathbf{k}}e^{2i\phi}$ to be real without loss of generality, because the phase can be removed by a Gauge transformation.

Consider energies much smaller than the gap, $k_n \ll \Delta_{\mathbf{k}}$ (with units $\hbar = 1$). In the weak-tunneling limit, $\Gamma \ll \Delta$, we can approximate the full Green's function of the semiconductor, by neglecting ik_n in the self-energy. This yields the effective Green's function

$$\mathcal{G}_N^{eff}(k_x, ik_n) = [ik_n - (\epsilon_{k_x} - \mu)\tau_z + \Delta_{eff}\tau_x]^{-1}, \quad (3.16)$$

where

$$\Sigma_{ss} \approx \frac{\Gamma}{2} \equiv \Delta_{eff} = \pi d(0)|V|^2. \quad (3.17)$$

The corresponding effective Hamiltonian can be read off as the terms subtracted from ik_n in the effective Green's function, that is

$$H_{eff} = \sum_{k_x} C_{k_x}^\dagger \begin{pmatrix} \epsilon_{k_x} - \mu & -\Delta_{eff} \\ -\Delta_{eff} & -\epsilon_{k_x} + \mu \end{pmatrix} C_{k_x}. \quad (3.18)$$

In the strong-tunneling case, ik_n cannot be ignored in the self-energy, because they correspond to poles in $\mathcal{G}_S^0(\mathbf{k}, ik_n)$. However, as long as $\Gamma \gg \Delta$, the effective gap in the semiconductor approaches that of the parent superconductor[10]. In conclusion,

The semiconductor inherits a superconducting gap from the parent superconductor.

The normal and gapped energy spectra are shown in figure 3.2. For every electron energy (solid lines), the energy of a hole is obtained by mirroring the point about the k_x -axis.

3.2 BTK theory

In order to understand non-local transport in a the three-terminal superconducting device, it is key to introduce the concept of Andreev reflection. In this chapter, we treat a normal-superconductor (*NS*) junction, using the Blonder-Tinkham-Klapwijk (BTK) theory for scattering across the interface.

3.2.1 Andreev Reflection

Consider the incoming electron in the normal metal in figure 3.3b with energy $E_{ek} = \mu + E_k$. E_k is the kinetic energy of the electron. The chemical potentials of both met-

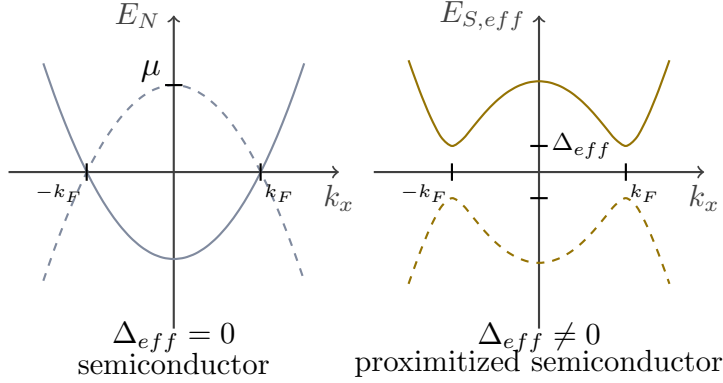


Figure 3.2: Left: The energy spectrum of a semiconductor, with the Hamiltonian in eq. (3.2), is $E_N = \pm(\epsilon_{k_x} - \mu)$. Right: The energy spectrum of the effective Hamiltonian in eq. (3.18), is $E_{S,eff} = \pm\sqrt{(\epsilon_{k_x} - \mu)^2 + \Delta_{eff}^2}$. k_F is the Fermi momentum.

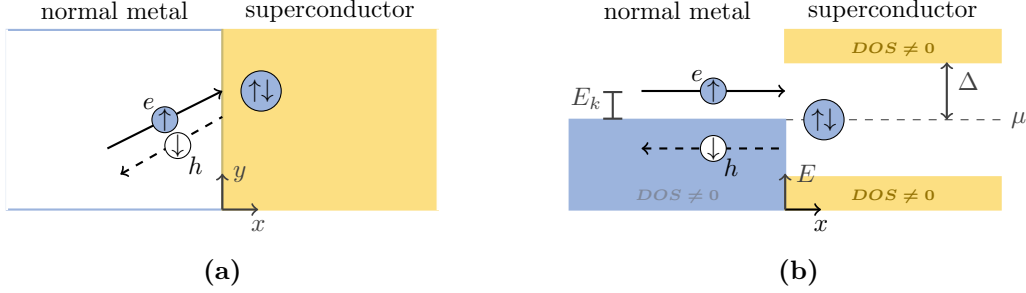


Figure 3.3: (a) Andreev reflection in real space. The hole follows the same path as the electron due to momentum conservation, because the transmitted Cooper pair has zero net momentum, assuming no momentum is transferred to a potential barrier at the NS interface. (b) Andreev reflection in energy and real space.

als, μ , are taken to be identical in this case. For energies below the superconducting gap ($|E| < \mu + \Delta$), there are no available quasiparticle states in the superconductor which the electron may transfer its momentum into in a scattering event. However, a Cooper pair can form inside the superconductor for energies equal to the Fermi energy. For instance, if the incident electron has momentum and spin $k \uparrow$, the superconductor may accept a Cooper pair ($k \uparrow, -k \downarrow$) at energy μ : momentum and energy *can* be conserved, if a hole $-k \downarrow$ reflects back into the normal metal with the energy $E_{hk} = -(\mu - E_k)$. This is known as *Andreev reflection*. The energy conservation condition reads

$$E_{ek} = E_{hk} + 2\mu, \quad \text{where } E_{ek} = \mu + E_k, \quad E_{hk} = -(\mu - E_k), \quad (3.19)$$

where $E_{e(h)k}$ is the energy of the incident electron (reflected hole). The charge $2e$ is transferred from the normal metal to the superconductor as a result of Andreev reflection.

As long as a current flows, the conductance can be measured across the NS junction as a function of an applied bias voltage, as illustrated in figure 3.4. Since there

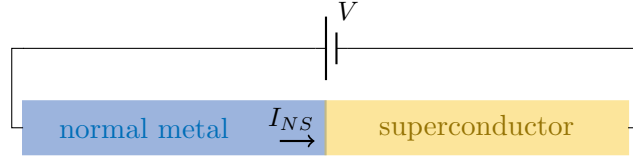


Figure 3.4: Normal-superconductor interface with an applied voltage V across. Positive current I_{NS} is taken to go from left to right.

is no normal reflection taking place for bias energies below the gap, a conductance signature inside the gap is completely due to Andreev reflection in an idealized interface with no potential barrier. If the energy is above the gap ($|E| \geq \mu + \Delta$), Andreev reflection may still take place, but it is accompanied by normal reflection and transmission.

The picture painted so far of Andreev reflection is idealized. Experimentally speaking, normal-superconductor interfaces are not ideal. Consequently, every impinging electron in the normal metal will not always Andreev reflect for energies below the gap, nor always transmit for energies above the gap. In addition, the density of the semiconductor may be lower than the superconductor, yielding a Fermi velocity mismatch [20]. Blonder, Tinkham and Klapwijk (BTK) introduces two modifications to model this [21]:

1. an interface potential barrier to model imperfect interfaces, and
2. a potential energy shift in the normal metal to model Fermi velocity mismatch.

This potential is depicted in figure 3.5a, together with the superconducting gap. For simplicity, this gap is assumed to be real and a step-function which is non-zero only inside the superconductor. The barrier is modeled as a delta-function, and a constant potential V_0 is added inside the normal metal. The total potential is

$$V(x) = H\delta(x) + V_0\Theta(-x). \quad (3.20)$$

The spatial coordinate x is taken to be perpendicular to the interface cross-section. The unitless step-function $\Theta(-x)$ is non-zero inside the normal metal, and models the applied bias between N and S (see figure 3.4). The barrier is positioned at $x = 0$.

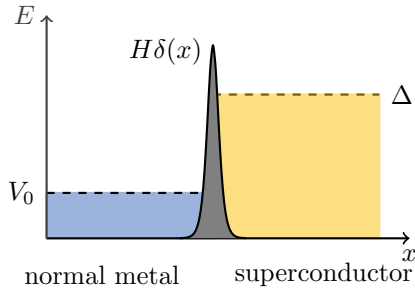


Figure 3.5: A picture of the individual potentials that are relevant in the model. The bias (blue) and the delta-function (gray) sums up to $V(x)$. The superconducting potential (yellow) is part of the superconducting Hamiltonian, and is taken to be real.

From standard introductions to quantum mechanics[22], plane waves scattering off the delta-potential, $H \delta(x)$, occurs with a transmission probability

$$T = (1 + Z^2)^{-1}, \text{ where } Z \equiv \frac{mH}{\hbar k_F} \quad (3.21)$$

is the unitless height of the barrier. The transmission is perfect ($T = 1$) if there is no barrier ($Z = 0$), thus the situation is back to the idealized case where every impinging electron on the NS barrier Andreev-reflects for energies below the superconducting gap. If the barrier strength H is increased, the transmission probability decreases.

With these ingredients in place, we can treat the interface using the Bogoliubov-de Gennes equation.

3.2.2 The Bogoliubov-de Gennes equation

The Bogoliubov-de Gennes equation enables us to keep and extract information about the energies, momenta and probability amplitudes of electrons and holes. Consider the NS interface and take both metals to be one-dimensional (1D). We assume each metal is clean enough that momentum is a good quantum number for labeling quantum states. The Bogoliubov equations can be used to determine the energies of the incident, reflected and transmitted plane waves on the NS interface. Take $f(x, t)$ and $g(x, t)$ to be components of the general solution wavefunction

$$\psi(x, t) = \begin{pmatrix} f(x, t) \\ g(x, t) \end{pmatrix}$$

of the scattering problem in the electron-hole basis. The Hamiltonian in this basis is $H = \psi^\dagger(x, t) \mathcal{H}_{\text{BdG}} \psi(x, t)$, from which we construct the BdG equation

$$i\hbar \partial_t \psi(x, t) = \mathcal{H}_{\text{BdG}} \psi(x, t), \quad (3.22)$$

where

$$\mathcal{H}_{\text{BdG}} = \begin{pmatrix} -\frac{\hbar^2 \nabla^2}{2m} - \mu(x) + V(x) & \Delta(x) \\ \Delta(x) & -\left[-\frac{\hbar^2 \nabla^2}{2m} - \mu(x) + V(x)\right] \end{pmatrix} \quad (3.23)$$

is the system Hamiltonian in the electron-hole basis. $\Delta(x) = \Delta \Theta(x)$ is real and non-zero only inside the superconductor, $\mu(x)$ is the chemical potential, and $V(x)$ is the potential inside the normal metal and the barrier potential, as given in eq. (3.20).

Writing it out explicitly, the Bogoliubov equation describes a set of two coupled differential equations of $f(x, t)$ and $g(x, t)$, namely

$$i\hbar \frac{\partial f}{\partial t} = \left[-\frac{\hbar^2 \nabla^2}{2m} - \mu(x) + V(x) \right] f(x, t) + \Delta(x) g(x, t), \quad (3.24)$$

$$i\hbar \frac{\partial g}{\partial t} = - \left[-\frac{\hbar^2 \nabla^2}{2m} - \mu(x) + V(x) \right] g(x, t) + \Delta(x) f(x, t). \quad (3.25)$$

$\Delta(x)$ couples $f(x, t)$ and $g(x, t)$. If $\Delta(x) = 0$, these relations reduce to the time-dependent Schrödinger equation for an electron (eq. (3.24)), and its time-reverse (eq. (3.25)).

3.2.3 The NS boundary at equilibrium

Consider the equilibrium case, where $V(x) = 0$ for all x . When the superconducting gap is non-zero, the energy dispersion for incident, transmitted and reflected modes with wavenumber k in the BdG equations, can be identified as the BCS quasiparticle energies

$$E_{\tau k} = \tau (\xi_k^2 + \Delta(x)^2)^{1/2}, \quad \text{where } \tau = e, h \quad (3.26)$$

as shown in figure 3.6a for $\Delta = 0$ (left) and $\Delta \neq 0$ (right). $\xi_k = \hbar^2 k^2 / 2m - \epsilon_F$ is the energy of the k 'th mode in the normal metal, and ϵ_F being the Fermi energy of said metal, set by the chemical potential. The τ factor is $+1$ for electrons ($\tau = e$) and -1 for holes ($\tau = h$). In the superconductor, a gap of size 2Δ opens at the Fermi momenta $\pm k_F$ (see figure 3.6a).

Derivation 3.2.1: Eq. (3.26) from the BdG equations

In order to see how the dispersion in eq. (3.26) comes about, from the BdG-equations, assume the simplest case where $\mu(x)$ and $\Delta(x)$ are constants. Inserting directly for plane-wave trial solutions

$$f(x, t) = u e^{ikx - iEt/\hbar}, \quad g(x, t) = v e^{ikx - iEt/\hbar},$$

into eqs. (3.24) and (3.25) (E is the energy, with the subscripts τk suppressed, and k is the wavevector), we obtain

$$\begin{aligned} Eu &= \xi_k u + \Delta v \\ Ev &= -\xi_k v + \Delta u \quad \text{for } \mu(x) = \epsilon_F; \Delta(x) = \Delta, V(x) = 0 \forall x. \end{aligned} \quad (3.27)$$

Solving these two equations for the energy is straightforward (start by squaring each side, *then* add them together). Assuming u and v are real, and using the normalization condition $u^2 + v^2 = 1$, reproduces the energy solution in eq. (3.26). It is also possible to solve eq. (3.27) for u and v . Lastly, we generalize to u and v being complex numbers, obtaining

$$|u|^2 = \frac{1}{2} \left(1 + \frac{\xi_k}{E} \right), \quad |v|^2 = 1 - |u|^2. \quad (3.28)$$

We also obtained this relation^a from BCS theory, see for instance figure 2.3. Showing eq. (3.28) requires some simple algebraic manipulations, where the normalization condition $|u|^2 + |v|^2 = 1$ is key (the calculation is shown in appendix B.1).

^aNote that u and v should be generalized to being complex. For energies below the gap, $|E| < \Delta$, u and v are complex conjugates, because $\xi_k = \sqrt{E^2 - \Delta^2}$ is purely complex.

For each energy E_k in eq. (3.26), there are four possible k -vectors, categorized by:

1. Two different *magnitudes*, k^\pm , referred to as the positive and negative branch.
2. Two *signs*, $\pm k$.

Category 1 comes about due to the fact that the momentum is squared in E_k . The explicit form for the momenta are

$$\hbar k^\pm = (2m)^{1/2} [\epsilon_F \pm (E_k^2 - \Delta^2)]^{1/2}. \quad (3.29)$$

The positive (negative) branch, k^+ (k^-), is always outside (inside) the Fermi surface. In figure 2.3, we plotted the amplitudes (coherence factors) from eq. (3.28) squared, as a function of the energy ϵ_k . For energies above (below) the Fermi energy, we saw that $|u_k| > |v_k|$ ($|v_k| > |u_k|$). The Bogoliubov excitation

$$\gamma_k^\dagger = u_k c_{k,\uparrow}^\dagger - v_k c_{-k,\downarrow}, \quad (3.30)$$

is therefore 'electron-like', $|u_k| > |v_k|$, for the k^+ branch. Similarly, hole-like excitations are of the k^- kind. Category 2 stems from the fact that the superconducting pairing potential correlates electronic particles with opposite momenta.

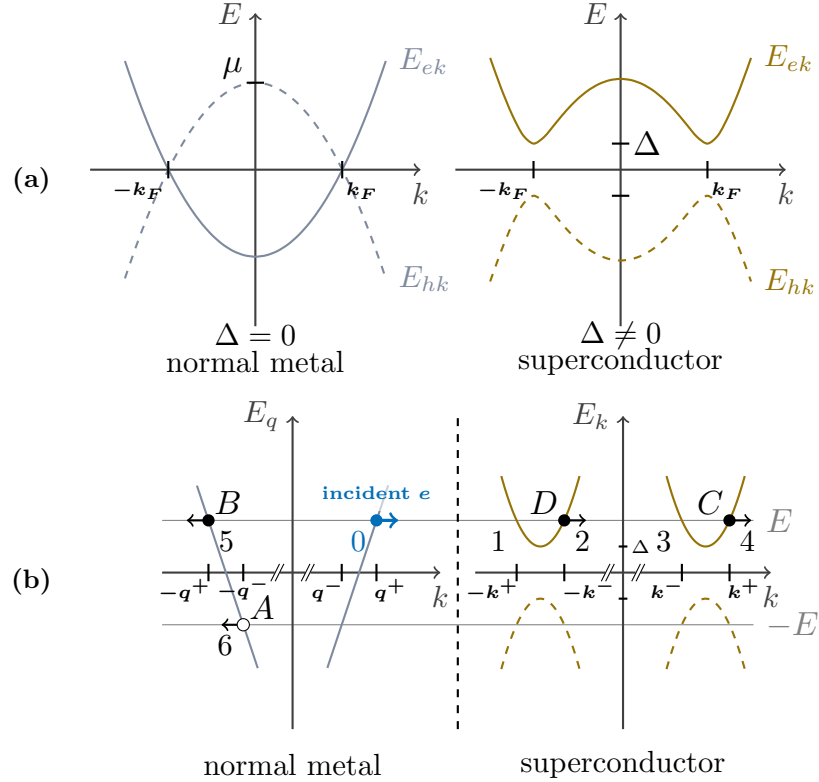


Figure 3.6: (a) The spectrum in eq. (3.26) is plotted for of electronic (solid) and hole (dashed) components. When the superconducting gap is non-zero (right), the spectrum is gapped at the Fermi momenta. If we consider only momenta close to the Fermi momentum, there are always four degenerate energies $E_{\pm k\pm}$ above the gap. (b) A diagram showing the energy spectra in (a), close to the Fermi momenta. Electrons are filled and holes are open circles. The arrows indicate the group velocity directions. An incident electron at point (0) is shown, together with the transmitted, (2, 4) and reflected (5, 6) particles.

For instance, consider an electron in N with energy E which is incident on the NS boundary. The only allowed scattering processes conserve energy, according to eq. (3.19), and particle group velocity, $dE_k/d(\hbar k)$. The energy diagram in figure 3.6b shows how energies and their slopes (arrows) need to be matched before and after the scattering event, close to the Fermi surface ($|k - k_F| \ll 1$). The momenta in the normal metal, q , are different from those in the superconductor, k , to accommodate a transfer of momentum to the boundary.

To be specific, the incident electron at point (0) may transmit with and without branch-crossing. (With: into point (2), $q^+ \rightarrow -k^-$. Without: into point (4), $q^+ \rightarrow k^+$). Crossing the branch, the momentum ends up on the opposite side of the

Fermi surface in the target system. The electron can also undergo normal reflection, which occurs without a branch crossing (into point (5), $q^+ \rightarrow -q^+$). Lastly, Andreev reflection can take place, where the electron crosses the branch in N (into point (6), $q^+ \rightarrow -q^-$). Normal reflection may only take place for a non-zero potential barrier, as we will see later in section 3.2.5. In the case of Andreev reflection, the electron is reflected as a hole ($E_{ek} \rightarrow E_{hk}$, see eq. (3.19)).

The probabilities corresponding to the physical processes are denoted A through D . $A(E)$ is the probability of the electron reflecting as a hole (Andreev reflection), leaving a Cooper pair inside the superconductor, $B(E)$ the probability of normal reflection, while $C(E)$ ($D(E)$) is the probability of transmitting as an electron quasi-particle excitation into the superconductor, with (without) a branch-crossing. Thus, conservation of probability current is

$$A(E) + B(E) + C(E) + D(E) = 1, \quad (3.31)$$

E being the energy of the incident electron.

It is also worthwhile noting that the Bogoliubov excitation γ_k^\dagger provide an overall electronic charge of $|u_k|^2 - |v_k|^2$ (see box 3.2.3).

Derivation 3.2.2: Charge conventions

The charge-operator in Nambu space, may be written as $\tau_z/2 + 1/2$, because

$$\begin{aligned} \hat{Q}_{k,\sigma} &= c_{k,\sigma}^\dagger c_{k,\sigma} = \frac{1}{2} \left(c_{k,\sigma}^\dagger c_{k,\sigma} - c_{k,\sigma} c_{k,\sigma}^\dagger + 1 \right) \\ &= \begin{pmatrix} c_{k,\sigma}^\dagger & c_{k,\sigma} \end{pmatrix} \frac{1}{2} \begin{pmatrix} 1 & 0 \\ 0 & -1 \end{pmatrix} \begin{pmatrix} c_{k,\sigma} \\ c_{k,\sigma}^\dagger \end{pmatrix} + \frac{1}{2}. \end{aligned}$$

In the first equality, the fermionic anti-commutation rule is used. Performing the expectation value of $\hat{Q}_{k,\sigma}$ with the state $|\psi_{k,\sigma}\rangle = u_{k,\sigma} |e\rangle + v_{k,\sigma} |h\rangle$, where $u_{k,\sigma}$ and $v_{k,\sigma}$ are complex numbers, and the basis vectors in electron-hole space are $|e\rangle = \begin{pmatrix} 1 & 0 \end{pmatrix}^T$, and $|h\rangle = \begin{pmatrix} 0 & 1 \end{pmatrix}^T$, yields

$$\langle \psi_{k,\sigma} | \hat{Q}_{k,\sigma} | \psi_{k,\sigma} \rangle = \frac{1}{2} \left(|u_{k,\sigma}|^2 - |v_{k,\sigma}|^2 \right) + \frac{1}{2}.$$

If the state is neither electron nor hole-like (charge neutral), then $u = v = 1/2$, which yields a charge $Q = 1/2$. In this sense, the charge of an electron is 1 and the charge of a hole is 0, not -1 . In the main text, however, the charge convention is $q = |u|^2 - |v|^2$ ($\hat{Q}_{k,\sigma} = \tau_z$), where we exclude the factor and last term of $1/2$. In the latter convention, the charges 0, 1 and -1 corresponds to the state being charge neutral, or having one electron or hole charge.

3.2.4 Probability amplitudes for scattered plane waves

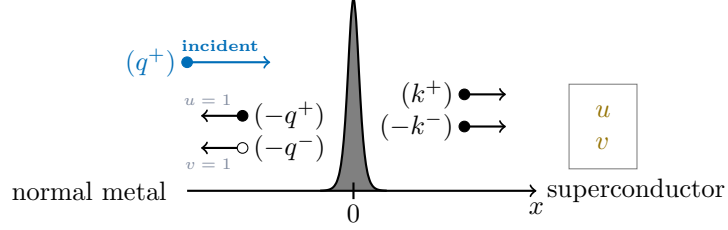


Figure 3.7: A real-space picture of these possible scattering events (see figure 3.6b) an incoming electron plane wave (blue arrow, with momentum q^+) can undergo. The explicit form of the wavefunctions are given in eq. (3.32). The vertical placement of the particles is arbitrary.

In the last section, we saw that electron-like excitations belong to the positive branch, while hole-like excitations belong to the negative branch. Inside the normal metal, in particular, particles are either electrons ($u = 1, v = 0$) or holes ($u = 0, v = 1$). For the scattering shown in figure 3.6b, the plane waves of possible incident, transmitted and reflected electrons and holes are therefore

$$\begin{aligned}\psi_{inc} &= \begin{pmatrix} 1 \\ 0 \end{pmatrix} e^{iq^+x}, \\ \psi_{refl} &= a \begin{pmatrix} 0 \\ 1 \end{pmatrix} e^{iq^-x} + b \begin{pmatrix} 1 \\ 0 \end{pmatrix} e^{-iq^+x}, \\ \psi_{trans} &= c \begin{pmatrix} u \\ v \end{pmatrix} e^{ik^+x} + d \begin{pmatrix} v \\ u \end{pmatrix} e^{-ik^-x}.\end{aligned}\quad (3.32)$$

The scattering amplitudes, constituting the probabilities $A = a^*a$ et cetera, multiplies each plane wave. The locations (whether in N or S) and directions of propagation of these wavefunctions are illustrated in figure 3.7. The branch-crossings are encoded in the momenta of the plane waves multiplying a and d , but also in the exchange of electron and hole amplitudes in the associated spinors.

In order to determine the solutions, take two boundary conditions. Denote $\psi_N(0) = \psi_S(0) \equiv \psi(0)$, $\psi_N = \psi_{inc} + \psi_{refl}$, $\psi_S = \psi_{trans}$. The first boundary condition is continuity of the wavefunctions at the boundary,

$$\psi_N(0) = \psi_S(0), \quad (3.33)$$

while the second is continuity in the difference between the derivative of the wavefunctions at the boundary. For the delta-potential barrier $H\delta(x)$, this second condition

is

$$\left. \frac{\partial \psi_S(x)}{\partial x} \right|_{x=0} - \left. \frac{\partial \psi_N(x)}{\partial x} \right|_{x=0} = \frac{2mH}{\hbar} \psi(0). \quad (3.34)$$

3.2.5 Computation of probabilities

In the following, we avoid the explicit inclusion of the density of states⁴ when considering the scattering probabilities, by assuming the probabilities already account for the canceling effects of reverse ($S \rightarrow N$) processes.

Probability and charge currents

Define the probability density of an electron or a hole by $P(x, t) = |f(x, t)|^2 + |g(x, t)|^2$, for a given time t and spacial coordinate x . From inserting the BdG equations (eq. (3.24) and (3.25)), the probability density current is⁵

$$\frac{\partial P}{\partial t} = \frac{\partial}{\partial t} (f f^\dagger) + \frac{\partial}{\partial t} (g g^\dagger) = \frac{\hbar}{m} \nabla \cdot [Im(f \nabla f^\dagger) - Im(g \nabla g^\dagger)],$$

In other words, this yields a source-less continuum equation

$$\frac{\partial P}{\partial t} + \nabla \cdot \mathbf{J}_P = 0 \quad (3.35)$$

where

$$\mathbf{J}_P = \frac{\hbar}{m} [Im(f^\dagger \nabla f) - Im(g^\dagger \nabla g)] \quad (3.36)$$

is the probability current flowing out of a closed surface. Similarly, take one unit charge for an electron (a hole) to be the elementary charge e ($-e$). With this choice, the net charge due to the excitations may be defined as $Q = e(|f|^2 - |g|^2)$. Inserting the Bogoliubov equations (eqs. (3.24) and (3.25)) into $\partial Q / \partial t$, one similarly obtains

$$\frac{\partial Q}{\partial t} + \nabla \cdot \mathbf{J}_Q = \frac{4e\Delta}{\hbar} Im(f^\dagger g) \quad (3.37)$$

$$\mathbf{J}_Q = \frac{e\hbar}{m} [Im(f^\dagger \nabla f) + Im(g^\dagger \nabla g)]. \quad (3.38)$$

⁴Because the density of states of the two metals are, in general, different, so are the incident and scattered particles are. Therefore, when we refer to probability currents canceling in equilibrium, we could have accounted for this difference in momenta, by using a formulation where we explicitly integrate over the density of states.

⁵The explicit calculation can be found in appendix B.2, and involves using the identity $\phi \nabla^2 \psi = \nabla \cdot (\phi \nabla \psi) - \nabla \phi \cdot \nabla \psi$ with the wavefunctions ϕ or ψ being the electron or hole component.

for the charge current. Contrary to the probability current, the charge current has a source (drain) term, $\frac{4e\Delta}{\hbar} \text{Im}(f^\dagger g)$. Interestingly, the source (drain) term couples f and g when Δ is finite. In a closed system, this charge should only originate from Cooper pairs splitting up. Quasiparticle current can therefore be converted to and from Cooper pair condensate current (supercurrent).

Explicit form of the scattering probabilities

The explicit forms of the probability amplitudes, a through d , are found by imposing the boundary conditions of eqs. (3.33) and (3.34) for the incident and scattered wavefunctions (see eq. (3.32)). This set of equations are solved for the four scattering amplitudes (see eqs. (B.6) through (B.9) in appendix B.4). Imposing the approximation that all momenta are at the Fermi momentum, the general form of the probabilities are (see eqs. (B.3) through (B.4)):

$$A = |a|^2 = \frac{u^2 v^2}{\gamma^2} \quad (3.39)$$

$$B = |b|^2 = \frac{(u^2 - v^2) \hbar^2 Z^2 (1 + \hbar^2 Z^2)}{\gamma^2} \quad (3.40)$$

$$C = |c|^2 (u^2 - v^2) = \frac{u^2 (u^2 - v^2) (1 + \hbar^2 Z^2)}{\gamma^2} \quad (3.41)$$

$$D = |d|^2 (u^2 - v^2) = \frac{v^2 (u^2 - v^2) \hbar^2 Z^2}{\gamma^2}, \text{ given } E > \Delta. \quad (3.42)$$

As long as $E > \Delta$, the coherence factors we insert for in these probabilities are real numbers (see eq. (3.28)).

However, if the energy is below the gap, these probabilities are complex numbers, and do not correspond to probability currents that correspond to physical observables. Let us see what happens if we insert for u and v (eq. (3.28)) in terms of the energy E and Δ :

$$A = \frac{\Delta^2}{E^2 + (\Delta^2 - E^2)(1 + 2Z^2)^2}, \quad B = 1 - A, \quad C = D = 0, \text{ given } E < \Delta. \quad (3.43)$$

In fact, no factors $E^2 - \Delta^2$ are present in eq. (3.43), thus we have explicitly ensured that these probabilities are real numbers. As noted in the introduction in this chapter, no single particle can transfer into the superconductor for energies below the gap (see for instance figure 3.3), thus C and D are zero for $E < \Delta$.

The probability currents A through D are plotted as functions of energy in figure 3.8, for barrier strengths $Z = 0, 0.3, 1.0$ and 3.0 . For no barrier and below the gap, see figure 3.8a, the electron Andreev reflects perfectly. When above the gap, A decreases

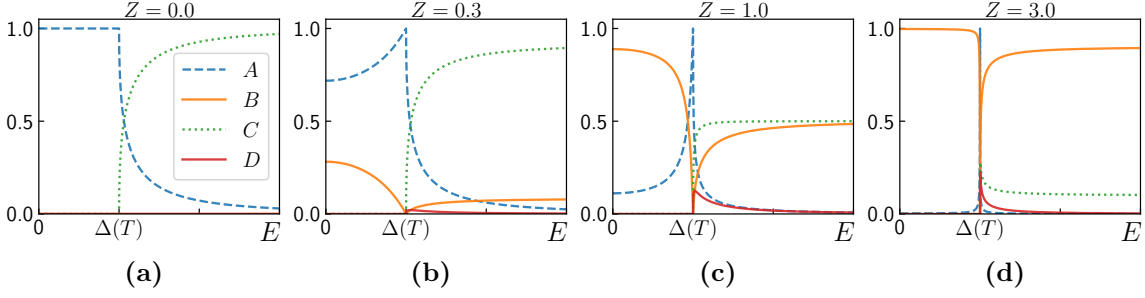


Figure 3.8: Probabilities (unitless) for Andreev reflection (A), normal reflection (B), and transmission with (C) and without (D) a branch-crossing (see figure 3.6b), as a function of energy displayed in steps of $\Delta(T)$.

monotonically as a function of E . In the absence of a barrier, explicitly inserting for $Z = 0$ in eqs. (3.39) through (3.43), yields

$$A = 1, B = C = D = 0, \text{ given } Z = 0, E < \Delta, \text{ and}$$

$$A = \frac{\Delta^2}{E^2 + (\Delta^2 - E^2)} = \frac{v^2}{u^2}, C = 1 - A, B = D = 0, \text{ given } Z = 0, E > \Delta.$$

Below the gap, all waves are perfectly Andreev reflected. Due to momentum conservation, all transmitted wavefunctions stay on the same side of the Fermi surface ($D = 0$) in this case.

When the barrier *is* present, see figures 3.8b through 3.8d, waves normally reflect off the barrier and B becomes non-zero below and above the gap. For modes with zero incoming energy E , the reflection probability is $B = 1 - A = 1 - 1/(1 + 2Z^2)^2$. As the barrier becomes larger, B therefore increases and converges towards

$$B(E = 0) = 1, \text{ when } Z \gg 1,$$

as is somewhat implied from comparing figure 3.8d ($Z = 3$) to figures 3.8b and 3.8c ($Z = 0.3$ and $Z = 1.0$, respectively). In other words, for strong barriers, most electrons undergo normal reflection.

dI/dV curves for the NS system

In chapter 5, we present the Landauer-Büttiker formalism that goes into deriving the current of the three-terminal, NSN system shown in figure 1.1. The term multiplying the Fermi distribution of the left normal lead, in resultant expression eq. (8.15), is simply the current of the NS system with no right normal lead. This current, I_{NS} , can be measured as a function of an applied voltage V , as illustrated in figure 3.4.

At zero temperature, the differential conductance is

$$\frac{dI_{NS}}{dV} = -\frac{e^2}{h} [N - B(eV) + A(eV)], \quad (3.44)$$

where N is the number of channels. The conductance is plotted in figure 3.9 for $N = 1$ channels, and different barrier strengths $Z = 0, 0.3, 1.0,$ and 3.0 . For energies

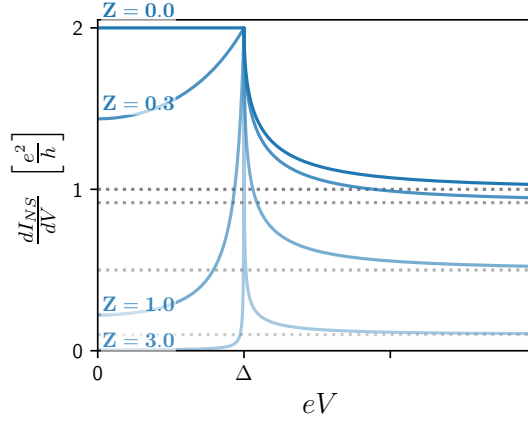


Figure 3.9: Differential conductance of a one-dimensional NS junction, for the unitless barrier strengths Z shown. R_N^{-1} (dashed horizontal lines) are shown for each value of the barrier Z .

below the gap, all incoming states will Andreev reflect, unless the barrier Z is non-zero. This corresponds to a conductance signature of $2e^2/h$. For larger finite barriers, the conductance decreases both above and below the gap, because the probability of normal reflection increases. For each value of the barrier, the conductance approaches the contact resistance in an NN junction, $R_N^{-1} = \frac{e^2}{h} \frac{1}{1+Z^2}$ (dashed horizontal lines), in the high voltage limit.

In spin-full systems with two possible spins, up and down, the maximal conductance signature is $4e^2/h$ for an NS junction. Such systems have $N = 2$ spin channels for every incident electron. Below the gap, $B(eV < \Delta) = 0$ and $A(eV < \Delta) = 2$ in the differential conductance in eq. (3.44). Therefore, the maximum conductance signature is $4e^2/h$. In the future, when we consider the superconducting region of the device to be spin-full, this is the relevant signature of perfect Andreev reflection.

Chapter 4

Topological Superconductivity

An infinite, one-dimensional p -wave superconductor hosts Majorana end modes in a specific region of parameter space, the *topological regime*. The Oreg-Lutchyn model has a specific topological regime. This model is used throughout the numerical simulations in this thesis. In order to understand what is meant by a topological model, we first describe a simpler p -wave Hamiltonian. In the topological regime, the Oreg-Lutchyn Hamiltonian can be mapped onto this simpler model. Thereby, we can apply our knowledge of the p -wave Hamiltonian to define the topological regime for the Oreg-Lutchyn Hamiltonian as well. We aim to illustrate this argument with this chapter, and thereby establish the topological regime for the p -wave model we implement in the simulations. The approach used in this chapter has been inspired by [2, 20].

Definition 4.0.1: S- and p-wave pairing in superconducting order parameter

The p-wave superconducting pairing is one that is not time-reversal symmetric. In general, it takes the form

$$\Delta_p = \langle \psi_\sigma^\dagger(\mathbf{r}) (-i\hbar\nabla) \psi_\sigma^\dagger(\mathbf{r}) \rangle e^{i\theta(\mathbf{r})},$$

where $\psi_\sigma^\dagger(\mathbf{r})$ is the creation operator of an electron with spin σ at the position \mathbf{r} , and $\theta(\mathbf{r})$ is the phase.

S-wave superconductive pairing does preserve time-reversal symmetry, and pairs opposite spins. It assumes the form

$$\Delta_s = \langle \psi_\sigma^\dagger(\mathbf{r}) \psi_{-\sigma}^\dagger(\mathbf{r}) \rangle e^{i\phi},$$

where ϕ is a phase.

4.1 Properties of Majorana fermions

Consider a one-dimensional tight-binding model consisting of N fermionic qubits. Each qubit corresponds to an artificial site in the discrete model, and can be either occupied or empty. For instance, if the degree of freedom is spin, then each site can either have spin up or have no spin, the downwards direction being completely forbidden. Such a system is completely spin-polarized.

In a conventional, spin-full superconductor, Bogoliubov quasiparticle excitations take the form $uc_{\uparrow}^{\dagger} + vc_{\downarrow}$. The operator c_{σ}^{\dagger} creates an electron, with spin projection σ . Per construction, a *Majorana* operator is its own hermitian conjugate. Contrary to the general Bogoliubon operators, *Majorana* operators are thus in an equal superposition of electron and hole, $|u| = |v| = \frac{1}{2}$, and both fermion operators must have identical spin. In other words, *Majorana* operators are a superposition of the real and imaginary component of a single fermion operator,

$$\gamma = uc_{\sigma}^{\dagger} + u^*c_{\sigma}, \quad (4.1)$$

and correspond to half a fermionic degree of freedom.

Every fermionic site, j , can be represented as a superposition of two Majorana sites, $j, 1$ and $j, 2$. Without loss of generality, assume the coherence factor from the representation in eq. (4.1) is real. Hence, we define the fermion annihilation and creation operators at site j as

$$c_j = \frac{1}{2}(\gamma_{j,1} + i\gamma_{j,2}), \quad c_j^{\dagger} = \frac{1}{2}(\gamma_{j,1} - i\gamma_{j,2}). \quad (4.2)$$

Inverting eq. (4.2) yields

$$\gamma_{j,1} = c_j^{\dagger} + c_j, \quad \gamma_{j,2} = i(c_j^{\dagger} - c_j), \quad (4.3)$$

which clearly satisfy

$$\gamma_{\nu}^{\dagger} = \gamma_{\nu}, \quad \{\gamma_{\mu}, \gamma_{\nu}\} = 2\delta_{\mu\nu} \quad (\mu, \nu \in \{j, 1, j, 2\}). \quad (4.4)$$

The first relation states that the Majorana is its own anti-particle. In the second relation, the fermionic anti-commutation rule $\{c_j, c_k^{\dagger}\} = \delta_{jk}$ has been employed. Even though Majorana operators are fermionic, only superpositions like those in eq. (4.2) are physically observable.

4.2 A p-wave superconductor can host Majorana fermions

The Kitaev model describes a discrete, one-dimensional (1D) system with a nearest-neighbor hopping, t , a spatially homogenous chemical potential, μ , and a complex

superconducting order parameter, $\Delta = |\Delta|e^{i\theta}$. The tight-binding Hamiltonian, illustrated in figure 4.1a, reads

$$H_{\text{chain}} = \sum_{j=0}^N \left(-t \left(c_j c_{j+1}^\dagger + c_{j+1}^\dagger c_j \right) - \mu \left(c_j^\dagger c_j - \frac{1}{2} \right) + \Delta c_j c_{j+1} + \Delta^* c_j^\dagger c_{j+1}^\dagger \right) \quad (4.5)$$

in the fermionic basis.

In this model, there is a regime in parameter space where Majorana modes $\gamma_{1,1}$ and $\gamma_{N,2}$ at the ends of the wire decouple from the rest of the Majorana sites. For

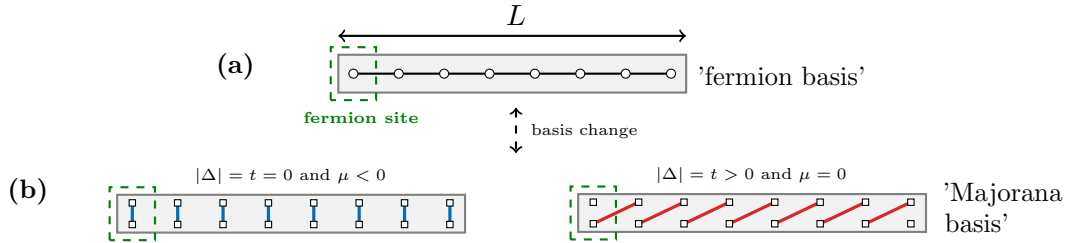


Figure 4.1: (a) A tight-binding model of a one-dimensional p-wave superconductor. Circles are fermionic lattice sites, and the lines connecting them is the hopping $-t$. (b) Each fermionic site corresponds to two Majorana sites (see (??)). Left: every Majorana site couple (via blue lines, $-t + |\Delta|$) within their corresponding fermionic site. Right: each Majorana couples (with red lines, $t + |\Delta|$) to the neighboring fermionic site, leaving two Majorana sites uncoupled at the edges.

example, the Hamiltonian in the case $\Delta \in \text{Re}$, $\Delta = t > 0$, and $\mu = 0$ is

$$\mathcal{H}_{\text{chain}} = it \sum_{j=1}^{N-1} \gamma_{i,2} \gamma_{j+1,1}. \quad (4.6)$$

To observe this, follow ¹. Majorana modes at neighboring sites pair up, as illustrated on the right in figure 4.1b.

An ordinary fermion requires a non-zero energy to be occupied. This is seen, for instance, in the case $t = \Delta$, $\mu = 0$. We introduce the non-local operators

$$\tilde{c}_i = \frac{1}{2} (\gamma_{i+1,1} + i\gamma_{i,2}), \quad \tilde{c}_i^\dagger = \frac{1}{2} (\gamma_{i+1,1} - i\gamma_{i,2}), \quad (4.7)$$

composed from Majorana operators from neighboring fermion sites. This yields $2\tilde{c}_i^\dagger \tilde{c}_i = 1 + i\gamma_{i+1,1} \gamma_{i,2}$. Inserting for this into eq. (4.6), one obtains

$$\mathcal{H}_{\text{chain}} = -t \sum_{i=1}^{N-1} \left(1 - 2\tilde{c}_i^\dagger \tilde{c}_i \right). \quad (4.8)$$

Transforming between the fermion and Majorana representations, eqs. (4.6) and (4.8), respectively, just changes the mathematical representation of the Hamiltonian. Two Majorana modes, paired between neighboring fermionic sites, correspond to ordinary fermions. Diagonalizing the Hamiltonian in the fermion representation, eq. (4.8), we see these fermions require an energy $2t$ to form.

Contrary to ordinary fermions, zero energy is required to occupy Majorana fermions. The Hamiltonian in eq. (4.6) does not contain $\gamma_{1,1}$ and $\gamma_{N,2}$. These sites are therefore de-coupled. This implies that there exists a non-local operator

$$\tilde{c}_M = \frac{1}{2} (\gamma_{N,2} + i\gamma_{1,1}) \quad (4.9)$$

which minimizes the energy of the chain. If the wire is infinitely long, the wavefunction, corresponding to the two Majorana modes at the ends, does not overlap. In that case, the fermion \tilde{c}_M , a superposition of the two end modes, requires zero energy to be occupied. In finite wires, the end state wavefunctions do overlap, and the excitation energy of this fermion is finite. We refer to such modes as near-Majorana modes.

Contrary to normal superconductors, where all fermions form Cooper pairs at sub-gap energies, the p-wave Hamiltonian allows for an even *or* an odd number of fermionic quasiparticle excitations. For example, if a Majorana is occupied at each end, the system hosts an odd number of occupied fermions at zero energy. If there are no Majorana end states, all Majoranas are paired up, forming only ordinary fermions. The latter situation is sketched on the left in figure 4.1b. The fermionic parity therefore corresponds to the eigenvalue, 1 (0), of number operator $\tilde{c}_M^\dagger \tilde{c}_M$, when applied to the occupied (unoccupied) ground state eigenfunctions, $|1\rangle_M$ ($|0\rangle_M$). We define the fermion parity as

$$\langle \mathcal{P} \rangle = \langle -i \prod_{j=1}^N \gamma_{j,1} \gamma_{j,2} \rangle = \langle -i \gamma_{1,1} \gamma_{N,2} \rangle = \langle 2\tilde{c}_M^\dagger \tilde{c}_M - 1 \rangle, \quad (4.10)$$

which measures to -1 ($+1$) when $|\cdot\rangle_M$ is occupied (unoccupied), corresponding to an odd (even) parity.

Majorana fermions always exist in pairs and cannot occupy the same site: they would annihilate each other due to being each others' anti-particle. Thus, the corresponding total wavefunction is *always* non-local. We stress that it is the *occupancy* of the Majorana sites that needs to be non-local. The wavefunction of an ordinary fermion can be *either* local or non-local, but two ordinary fermions cannot occupy the same site, due to the Pauli exclusion principle. Therefore, a non-local state can be either a Majorana pair, or consist of ordinary fermions. A local wavefunction cannot be a Majorana pair. Hence, finding a way to measure non-locality, in itself, is not a "smoking-gun" for determining whether or not a system hosts Majorana end modes.

In this thesis, we do not claim to propose a "smoking-gun" measurement. One such proposal involves adiabatically braiding Majorana modes from two different pairs of Majorana end states, to demonstrate their *non-abelian* (non-commuting) braiding statistics [6].

In experiments, one may test the 'robustness' of a gapped state, is to introduce changes in independent variables, such as the chemical potential, an applied magnetic field, or by introducing local gates, and see if the emergent bound states are robust to these variations. Such robustness has been observed in experiments, but does not constitute a definite proof of Majorana modes [14, 1].

So far, we have seen two very particular examples where the Kitaev chain does, and does not, host Majorana end states. There is, however, a whole range of parameters where the system hosts end states.

4.2.1 Energy spectrum

Fourier-transforming each fermionic operator to k -space ($c_j = \sum_k e^{-ikj} c_k$ with the inter-site spacing set to 1 in length-units) in eq. (4.5), yields

$$\mathcal{H}(k) = -\xi_k \tau_z + 2\Delta \sin(k) \tau_y \quad (\xi_k = 2t \cos(k) + \mu) \quad (4.12)$$

in the electron-hole basis, spanned by spinors $\Psi_k = (c_k, c_{-k}^\dagger)^T$ and its hermitian conjugate. The Hamiltonian in eq. (4.12) can be identified as the tight-binding approximation to a general p -wave Dirac Hamiltonian of the form

$$\mathcal{H}_{p\text{-wave}}(k) = m\tau_z + vk\tau_y, \quad \text{with } m = -2t \cos(k) - \mu, \quad vk = 2\Delta \sin(k). \quad (4.13)$$

m is a mass-term, which can open a gap in the energy spectrum, and v is a velocity.

The energy spectrum of the p -wave Hamiltonian in eq. (4.13) is

$$E_{e/h}(k) = \pm \sqrt{m(x)^2 + (vk)^2}, \quad (4.14)$$

¹One may start by specifying the general Majorana operators as

$$\gamma_{j,1} = e^{i\frac{\theta}{2}} c_j + e^{-i\frac{\theta}{2}} c_j^\dagger, \quad \gamma_{j,2} = -ie^{i\frac{\theta}{2}} c_j + ie^{-i\frac{\theta}{2}} c_j^\dagger \quad (j = 1, \dots, N),$$

similarly to in eq. (4.3), but where we have included the phase from the superconducting order parameter. Inserting for this in eq. (4.5) yields

$$H_{chain} = \frac{i}{2} \sum_j^L (-\mu \gamma_{2j-1} \gamma_{2j} + (t + |\Delta|) \gamma_{2j} \gamma_{2j+1} + (-t + |\Delta|) \gamma_{2j-1} \gamma_{2j+2}). \quad (4.11)$$

With the parameters in the main text, the Hamiltonian takes the form of eq. (4.6).

where the $+$ sign is for electrons and $-$ for holes. From here on in this section, we assume Δ is real and positive, and explicitly include a spatial dependence in the mass term. We want to use linearization in the vicinity of the gap closings later, in order to map the Oreg-Lutchyn model onto this p -wave model.

The energy dispersion of the tight-binding Hamiltonian is

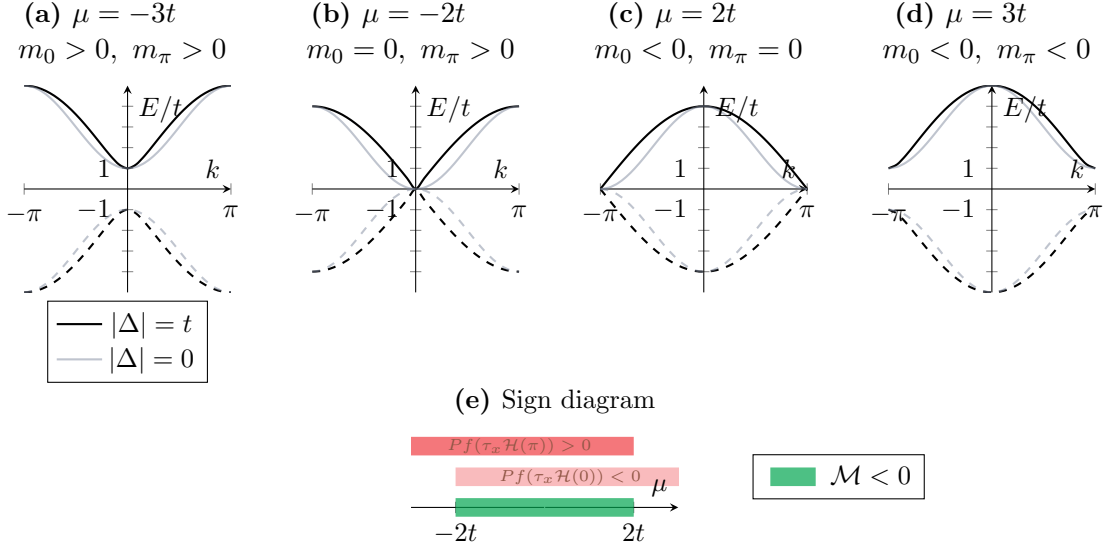


Figure 4.2: (a)-(d): The energy dispersion in eq. (4.15), outside the topological region in (a) and (d), and at the topological phase transition in (b) and (c). (e): The topological index (see eq. (4.18)) is non-trivial (-1) inside the region $|\mu| < 2t$. Everywhere else, the index is trivial ($+1$).

$$E_{e/h}^{t-b}(k) = \pm \sqrt{(2t \cos(k) + \mu(x))^2 + 4\Delta^2 \sin^2(k)}. \quad (4.15)$$

The dispersion is plotted in figure 4.2a through (d), for different values of the chemical potential.

When this spectrum in eq. (4.15) is linearized about $k \approx 0$, or $k \approx \pi$, the mass term is

$$m_k(x) = \begin{cases} -\mu(x) - 2t & \text{when } k \approx 0 \\ \mu(x) - 2t & \text{when } k \approx \pi. \end{cases} \quad (4.16)$$

The gap closes at $k = 0$, for $\mu(x) = -2t$, and for $k = \pi$, when $\mu(x) = 2t$. See figures 4.2b and (c). Both these points have an associated mass term $m_{0/\pi} = 0$. The total parity of the system changes as the gap closes and re-opens. Resultantly, the ground

state changes from one, to the other one of the two degenerate ground states. The *topological index*, \mathcal{M} , changes sign during such a transition. It is not to be confused with the total parity of the system.

With $|\Delta| \neq 0$, the spectrum is linear in k around the gap closings. Comparatively, if the gap is zero (faint line), the spectrum is not linear for $k \sim 0, \pi$. Thus, the non-zero gap is what enables us to linearize the spectrum.

During a topological phase transition, the system will change between being topologically non-trivial, having two topologically protected end states (in 1D), and being topologically trivial, having no topological end states. This is much like the two special cases displayed in figure 4.1b. In principle, one way to *measure* whether a wire has end states or not, is to (i) attach it (in real space) to another wire, with a known topology, and then to (ii) measure the fermionic parity of the total system. We elaborate on both points, after introducing the *bulk-edge correspondence*.

4.2.2 Bulk-edge correspondence

The eigenstates of eq. (4.13) are specified in the electron-hole basis, and we denote them by $\phi(x) = (\tilde{u}(x), \tilde{v}(x))^T$. We seek a zero energy solution. The time-independent Schrödinger equation with a zero energy eigenvalue,

$$\mathcal{H}\phi(x) = (m(x)\tau_z + vk\tau_y)\phi(x) = 0,$$

multiplied on both sides by τ_y from the left, reads

$$\tau_y\mathcal{H}\phi(x) = (m(x) \times 2i\tau_x + v(-i\partial_x))\phi(x) = 0,$$

where $k = -i\partial_x$ ($\hbar = 1$). When re-arranged for $\partial_x\phi(x)$, it is equivalent to the differential equation

$$\partial_x\phi(x) = \frac{2m(x)}{v}\tau_x\phi(x).$$

Integrating both sides and solving it, by inserting for the eigenstates $(1, \pm 1)^T$ of τ_x , yields

$$\phi_{\pm}(x) = \exp\left[\pm \int_0^x \frac{2m(x_1)}{v} dx_1\right] \begin{pmatrix} 1 \\ \pm 1 \end{pmatrix},$$

where the \pm index and phase factor correspond to the two eigenstates of τ_x . The only way this can be normalizable, is if it decays exponentially, which is the case when the sign of the exponential

$$\underbrace{\pm}_{\tau_x \text{ eig.state}} \text{sign}\left(\lim_{x \rightarrow \pm\infty} m(x) \times x\right) < 0 \quad (4.17)$$

is negative. Lastly, assume that $m(x_1)$ is a step-function, which takes some constant value for $x = +\infty$, and another constant value, with opposite sign, for $x = -\infty$.

For simplicity, we take a parametrization such that the sign of $\mu(x)$ is the same as that of x^2 . First, consider the case $k \approx 0$, for which $m(x) \approx m_0(x) = -\mu(x) - 2t$ (see eq. (4.16)). In this case, only the (+) phase yields a normalizable solution, according

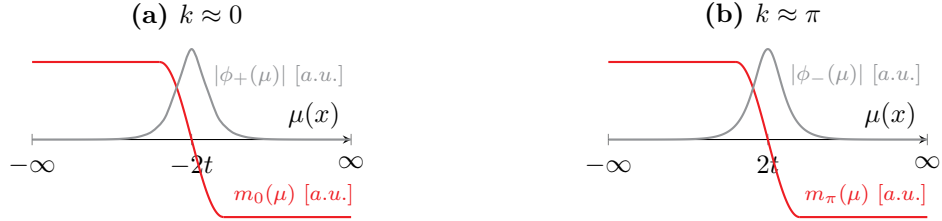


Figure 4.3: The eigenfunction of the p-wave Hamiltonian in eq. (4.13) is localized at the point where the mass term changes sign.

to eq. (4.17). This solution, $\phi_+(x)$, is localized at the position $\mu(x) = -2t$ where the mass term $m_0(x)$ changes sign, as illustrated in figure 4.3a. Similarly, when $k \approx \pi$ and $\mu(x) = 2t$, the mass $m_\pi(x)$ changes sign, see figure 4.3b. Therefore,

At the interface between sections with positive and negative mass terms in real space, there exists a localized zero energy mode for the p-wave Hamiltonian in eq. (4.13).

If we attach two wires, where the mass of both wires have the same sign, there is no localized state. When $m(x)$ does not change sign, it does not cross zero, and the energy gap is not allowed to close. As we will see next, the fermionic parity of the system can therefore not change as a result of "attaching" the wires, and both wires either do, or do not have two end states.

Fermion parity switches when the energy gap changes sign. The fermionic parity is a physical observable that measures whether the system has a odd or even number of fermions. As a thought experiment, consider the specific set-up where the wire of interest (Kitaev wire 1) is attached to another, auxiliary wire (Kitaev wire 2) in both ends. This is illustrated in figure 4.4a through (d) for all four possible combinations of wires, with positive and negative mass terms.

These examples illustrate how the fermionic parity of the total system can distinguish the topological and trivial phase of wire (1), given that we know the topology

²If we assume the opposite sign, namely $\text{sign}(\mu(x)) = \mp \text{sign}(x)$, the normalizable solutions for $k \approx 0$ and $k \approx \pi$ interchange, see eq. (4.17).

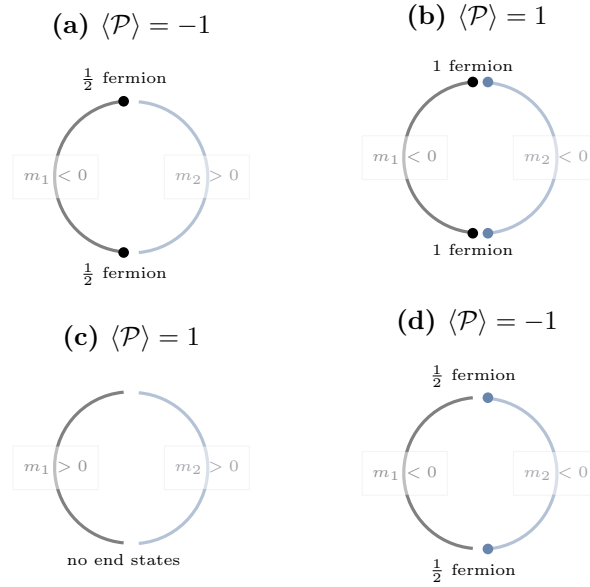


Figure 4.4: (a)-(d): Left (gray) wires: system of interest. Right (faint blue) wires: an auxiliary system is attached in both ends of the wire, such that the total parity can distinguish between a total system with, from one without end states.

of wire (2). Say the auxiliary wire is trivial. Then, if the wire of interest hosts end states, the total parity of the system is odd when the two wires are attached, as shown in figure 4.4a, because the end states do not annihilate. If the system of interest is trivial, as shown in 4.4c, both wires have an even number of fermions, such that the measured parity is even. On the other hand, if the auxiliary system does host end states, shown in figures 4.4b and (d), the measured parity is necessarily opposite to in (a) and (b), respectively. In summary, whenever the sign of the mass of systems (1) and (2), m_1 and m_2 , are different (the same), the total system hosts (no) end states and the parity is odd (even). This, we can associate with the expectation value of the parity operator being -1 ($+1$). In other words, the parity of the combined system is

$$\langle \mathcal{P} \rangle = \text{sign} [m_1 \cdot m_2].$$

Therefore, whenever the gap of one of the two systems closes, the parity changes. Now, we are done with the thought experiment.

In BCS theory, we describe superconductors as a bosonic Cooper pair condensate, with Bogoliunov quasiparticle excitations. The latter is the only fermionic degree of freedom of the system. Thus, the addition or subtraction of such a quasiparticle is the way in which the superconductor can change its parity. The superconductor should be thought of as being in contact with a reservoir, such that a quasiparticle must be moved to the reservoir in order to conserve the *total* parity of the system and the reservoir altogether.

For every position x in real space, the Hamiltonian describes states with a continuum of different k -values. Since the parity only can change when the gap closes, which may occur for $k = 0$ and $k = \pi$, these are the only momenta which determine whether the gap in the energy spectrum closes. Thus, we need only consider $k = 0, \pi$, and not the whole continuum of k -values. Hence, the picture with the two wires in figure 4.4 is an analogy to the parity of the actual system, which is determined by the sign of the product of masses $m_{0/\pi}$, that is,

$$\langle \mathcal{P} \rangle = \text{sign} [m_0 \cdot m_\pi],$$

instead of the product with $m_{1/2}$.

In terms of the system parameters, the fermion parity is easily accessible from the Hamiltonian directly. First, make the Hamiltonian skew-symmetric by multiplying it by τ_x at $k \approx 0$,

$$\tau_x H(k \approx 0) = \begin{pmatrix} 0 & -m(x) \\ m(x) & 0 \end{pmatrix},$$

and similarly for $k \approx \pm\pi$ (where $m(x) \rightarrow -m(x)$). Then, we can access the mass term by taking the Pfaffian. The topological properties of the Hamiltonian is given by the \mathbb{Z}_2 topological index, or *Majorana number*

$$\mathcal{M} = \text{sign} [Pf(\tau_x \mathcal{H}(0)) \cdot Pf(\tau_x \mathcal{H}(\pi))], \quad (4.18)$$

which is -1 for the topological phase, and 1 in the trivial case. This topological invariant is based on deeper topology arguments, and not the parity, as could seem to be implied in this discussion³. For the present Hamiltonian, we do see that these Pfaffians coincide with a parity measure. To recap:

³We could also have introduced a more general classification of topological phases in this thesis, in terms of the symmetries a Hamiltonian exhibits in a given dimension. For instance, in one dimension, a negative mass is associated with a non-trivial winding number. The one-dimensional, single-particle p -wave Hamiltonian considered here, belongs to the universal symmetry class BDI [23]. The p -wave Hamiltonian considered here is particle-hole antisymmetric ($\Gamma \mathcal{H} \Gamma^{-1} = -\mathcal{H}$, with $\Gamma = \tau_x \mathcal{K}$, and \mathcal{K} the complex conjugation operator). It is also time-reversal symmetric ($\Theta \mathcal{H} \Theta^{-1} = \mathcal{H}$), if we transform the Hamiltonian using a pseudo time reversal operator, $\Theta' = \tau_z \mathcal{K}$.

Whenever the sign of one Pfaffian in eq. (4.18) changes, the mass term at one of the k -values changes sign, and the gap closes and re-opens at that particular k -value. The bulk-edge correspondence predicts that, when the energy spectrum is gapped and in the topological regime, there exists zero-energy end states for the p-wave Hamiltonian.

The sign diagram in figure 4.2e illustrates that the system is in *the topological regime* ($\mathcal{M} < 0$) for

$$|\mu(x)| < 2t$$

in the tight-binding model. Inserting for the parametrization, this corresponds to:

$$m_{0/\pi} < 0$$

in the topological regime for the continuum p -wave Hamiltonian in eq. (4.13).

4.3 The Oreg-Lutchyn model

In order to physically realize a topological p-wave superconductor, the system needs to

1. be effectively spinless, and
2. have p -wave pairing at the Fermi energy.

Both can be approximately satisfied in a spin-orbit coupled semiconducting wire in proximity to an s-wave superconductor, when subject to a magnetic field. This is modeled by the Oreg-Lutchyn Hamiltonian. In this chapter, we show how these two criteria may be satisfied in this model.

Consider a one-dimensional semiconducting wire on top of a three-dimensional s-wave superconductor, as outlined in figure 4.5. Due to the proximity effect, the semiconductor inherits an effective p-wave superconducting gap. See chapter 3.1 for a demonstration of how the self-energy in the semiconductor incorporates this effect. The Hamiltonian of the proximitized semiconducting wire along the z -direction is

³The Pfaffian of any skew-symmetric matrix $\begin{pmatrix} 0 & -a \\ a & 0 \end{pmatrix}$ is a . Contrary to the determinant, if the sign of a changes, the information of this sign stays encoded in the Pfaffian.

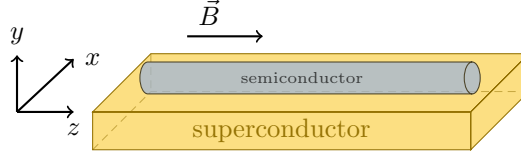


Figure 4.5: A thin semiconducting wire proximitized by a three-dimensional superconductor with an applied magnetic field along the wire.

given by the Oreg-Lutchyn Hamiltonian [11, 12]

$$\begin{aligned}
 H &= \int \Psi^\dagger(z) \mathcal{H} \Psi(z) dz, \quad \text{where} \\
 \mathcal{H} &= \left(\frac{\mathbf{p}^2}{2m^*} - \mu + \tilde{\alpha}_R (\mathbf{E} \times \mathbf{p}) \cdot \boldsymbol{\sigma} \right) \tau_z + \frac{1}{2} g \mu_B \mathbf{B}(\mathbf{r}) \cdot \boldsymbol{\sigma} + \Delta \tau_x \\
 &= \left(-\frac{\hbar^2 \partial_z^2}{2m^*} - \mu - i \alpha_R \partial_z \sigma_x \right) \tau_z + V_Z \sigma_z + \Delta \tau_x.
 \end{aligned} \tag{4.19}$$

The Hamiltonian is specified in Nambu space, where the Nambu spinor is $\Psi^\dagger = (\psi_\uparrow^\dagger, \psi_\downarrow^\dagger, \psi_\downarrow, -\psi_\uparrow)$, and σ and τ are Pauli matrices in spin and electron-hole space, respectively. In the second line for \mathcal{H} , we assume the electric field \mathbf{E} that gives rise to the Rashba spin-orbit coupling, points in the y -direction. The chemical potential of the wire is μ , while $\alpha_R = |\mathbf{E}| \tilde{\alpha}_R$ and $V_Z = B_Z/2$ parametrizes the Rashba spin-orbit coupling and the Zeeman field, where $B_Z = g \mu_B B$ is the Zeeman splitting of an electron due to the applied parallel magnetic field B , and g is the gyromagnetic ratio in the wire. Δ is the induced superconducting gap, taken to be real for convenience.

The energy spectrum

$$E_\pm^2 = \xi_p^2 + u^2 p^2 + V_Z^2 + \Delta^2 \pm 2 \sqrt{V_Z^2 \Delta^2 + \xi_p^2 V_Z^2 + \xi_p^2 u^2 p^2}, \tag{4.20}$$

is found by squaring both sides of the Hamiltonian in eq. (8.37), and using the anti-commutation relations for the Pauli matrices. We introduce the notations $\xi_p = p^2/2m^* - \mu$, $u = \alpha_R/\hbar$, $p = -i\hbar\partial_z$, and $up = -i\alpha_R\partial_z$.

4.3.1 Helical state ($\Delta = 0$)

With no magnetic field nor superconducting gap, the dispersion from eq. (4.20) is

$$E_\pm(k; \Delta = V_Z = 0) = (\xi_k \pm \alpha_R k). \tag{4.21}$$

When the spin-orbit coupling (the second term) is zero, this is just the normal quadratic dispersion ξ_k , shown in figure 4.6a for positive energies. As the spin-orbit

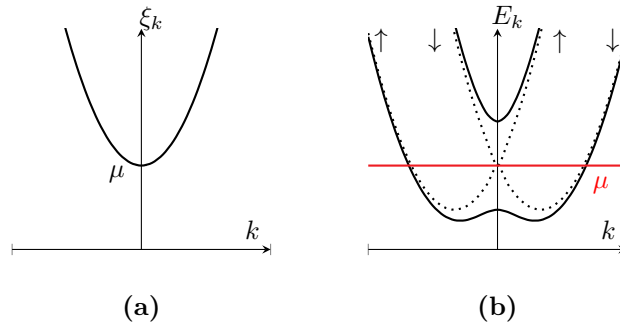


Figure 4.6: (a) Quadratic dispersion for normal metal. (b) Spin-split bands when $V_Z = \Delta = 0$ (dotted) turn into helical bands (solid) when V_Z is non-zero.

coupling increases, the band spin-splits. If the state has, say spin up (down) corresponding to $+(-)\alpha_R k$, the band shifts to the left (right). The spectrum is gap-less, and each band is completely spin-polarized.

Turning on the magnetic field too, the dispersion from eq. (4.20) can be written as (by completing the square)

$$E_{\pm}(k; \Delta = 0) = \left(\xi_k \pm \sqrt{\alpha_R^2 k^2 + V_Z^2} \right). \quad (4.22)$$

This spectrum (dotted lines) is shown in figure 4.6b. The corresponding Hamiltonian is the full Hamiltonian for the spin-orbit coupled semiconductor, without the superconducting pairing. The *helical regime* is obtained by applying a magnetic field (perpendicular to) the electric spin-orbit field. It opens a gap at $k = 0$. If the chemical potential is set to be inside the gap, the state is in a mixture of spin up and down, depending on what momentum it has. This is the helical regime, which, as we will see in the later chapter, is a pre-cursor[20] to the topological state: If the topological gap is set to be non-zero when in the helical regime, the topological phase emerges, because the system Hamiltonian can be mapped to an effectively spinless, p-wave Hamiltonian.

4.3.2 State hosting Majorana fermions

The first criterion of being spinless is already fulfilled in the helical state. Here, spinless is understood as the state being non-degenerate and locked to a given momentum. Turning on Δ , which is weak compared to V_Z , effectively p-wave couples fermionic pairs in the lower energy band, at momenta $-k$ and k , where the chemical potential crosses the lower band when placed inside the band gap. At these (Fermi) points, due to the applied magnetic field, the spins align. This drives the system into the

topological phase. However, if the gap is larger than the Zeeman energy, states from the upper band are intermixed with the lower band through the superconducting coupling, and the system is no longer in the spin-less regime, and thus does not host topological states anymore. We elaborate on these points in the following.

The gap at $k = 0$ is key for the emergence of Majorana end modes in the wire. At $k = 0$, the energy E_- (see eq. (4.20)) is

$$E_0 = E_-(k = 0) = \left| V_Z - \sqrt{\Delta^2 + \mu^2} \right|. \quad (4.23)$$

This gap closes at $V_Z^2 = \Delta^2 + \mu^2$, which is where a topological phase transition occurs. For $V_Z^2 > \Delta^2 + \mu^2$, the gap E_0 is called "field-dominated". The phase is topological because the spins at the Fermi points are in the same direction, in turn giving rise to an effective p-wave superconducting pairing. This is shown in the next section, by linearizing the Hamiltonian around $k = 0$. When $V_Z^2 < \Delta^2 + \mu^2$, the gap is "pairing dominated", and the phase is trivial. The Majorana states can emerge in many

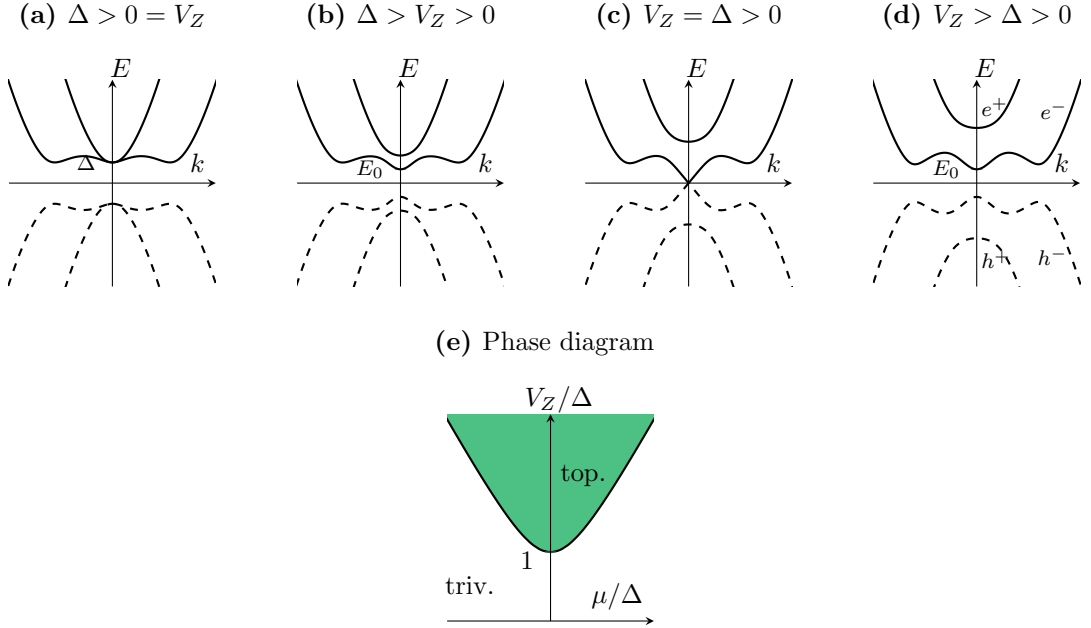


Figure 4.7: (a) Through (e): Energy spectrum for the Oreg-Lutchyn model, with $\mu = 0$. (a) and (b): The gap E_0 at $k = 0$ (see eq. (4.23)) is pairing dominated, and the phase is trivial. (c) The gap closes at $k = 0$, and the system undergoes a topological phase transition. The spectrum is approximately linear in the vicinity of $k = 0$. (d) E_0 is field-dominated, and the system is topological. (e): The topological phase diagram. Green: the topological region ($V_Z^2 > \Delta^2 + \mu^2$). Elsewhere: the trivial region.

ways, because the gap E_0 depends on three different parameters (see [11, fig. 2]).

For instance, Δ could be spatially varying to model a normal-superconductor-normal junction ([11, fig. 2c]), while keeping a constant applied field and chemical potential in all three components.

4.3.3 Mapping to a p-wave Hamiltonian

The total Hamiltonian in eq. (8.37), describing the wire in figure 4.5, can be separated into the normal (N) and superconducting (S) components

$$\mathcal{H}_N = \xi_k \tau_z + \alpha_R k \sigma_x \tau_z + V_Z \sigma_z \quad (4.24)$$

$$\mathcal{H}_S = \Delta \tau_x. \quad (4.25)$$

In order to identify the eigenbasis for the total Hamiltonian, corresponding to the different energy bands in figures 4.7, we rotate the Hamiltonian. Consider the following unitary transformation $\mathcal{U}^\dagger \mathcal{H} \mathcal{U}$, where

$$\begin{aligned} \mathcal{U} &= e^{i\frac{\theta}{2}\sigma_y\tau_z} \\ e^{i\theta\sigma_y\tau_z} &= V_Z \kappa^{-1} + i\alpha_R k \kappa^{-1} \sigma_y \tau_z \\ \cos(\theta) &= V_Z \kappa^{-1}, \quad \sin(\theta) = i\alpha_R k \kappa^{-1}, \end{aligned} \quad (4.26)$$

and $\kappa = \sqrt{\alpha_R^2 k^2 + V_Z^2}$, yielding

$$\begin{aligned} \mathcal{U}^\dagger \mathcal{H}_N \mathcal{U} &= \xi_k \tau_z + \alpha_R k e^{-i\theta\sigma_y\tau_z} \sigma_x \tau_z + V_Z e^{-i\theta\sigma_y\tau_z} \sigma_z \\ &= \xi_k \tau_z + (V_Z \kappa^{-1} + i\alpha_R k \kappa^{-1} \sigma_y \tau_z) (\alpha_R k \sigma_x \tau_z + V_Z \sigma_z) \\ &= \xi_k \tau_z + \kappa \sigma_z. \end{aligned} \quad (4.27)$$

We use the anti-commutator relation $\{\sigma_{x_i}, \sigma_{x_j}\} = 0$ for $i \neq j$, and the commutator $[\sigma_{x_i}, \sigma_{x_i}] = 0$ in the first line, to move the Pauli matrices to the right, yielding an extra minus sign in the exponential whenever the matrices belonging to the same space are different. Afterwards, the identity $\sigma_{x_i} \sigma_{x_j} = i\epsilon_{ijk} \sigma_{x_k}$ is inserted for, as well as the definitions in eq. (4.26). The Hamiltonian in eq. (4.27) has exactly the helical dispersion given by eq. (4.22) and which is plotted in figure 4.6b. Electron and hole components are yet to be coupled by the pairing potential Δ . Similarly,

$$\mathcal{U}^\dagger \mathcal{H}_S \mathcal{U} = V_Z \Delta \kappa^{-1} \tau_x + \alpha_R k \Delta \kappa^{-1} \sigma_y \tau_y$$

and thus the total Hamiltonian is

$$\mathcal{U}^\dagger \mathcal{H} \mathcal{U} = \begin{array}{c} \text{hel. basis} \\ \begin{array}{c} e^+ \\ e^- \\ h^- \\ h^+ \end{array} \end{array} \left[\begin{array}{cc|cc} e^+ & \xi_k + \kappa & 0 & \Delta_s \\ e^- & 0 & \xi_k - \kappa & \Delta_p \\ \hline h^- & \Delta_s & \Delta_p & -\xi_k + \kappa \\ h^+ & -\Delta_p & \Delta_s & 0 \\ \hline & & & 0 \end{array} \right] \begin{array}{c} h^- \\ h^+ \\ \\ \end{array} \quad (4.28)$$

with $\Delta_s = V_Z \Delta \kappa^{-1}$ and $\Delta_p = \alpha_R k \Delta \kappa^{-1}$. Eq. (4.28) is given in the helical basis. We call the basis vector $\Psi_{\text{hel.}} = (e^+, e^-, h^-, h^+)^T$, and the different components are as indicated in the matrix. We may identify three types of terms in (4.28).

- Diagonal terms $\xi_k \tau_z + \kappa \sigma_z$ are equivalent to the dispersion of \mathcal{H}_N alone, namely $E_{\pm}(k, \Delta = 0)$ (see figure 4.6).
- *Anti-diagonal* terms $\Delta_p \sigma_y \tau_y$ parametrize the *p*-wave pairing between *same* bands.
- Other off-diagonal terms $\Delta_s \tau_x$ parametrize a *s*-wave pairing between *different* bands.

So far, we can conclude that: The diagonal terms the Hamiltonian, indeed represent the helical bands in figure 4.6b for electrons and holes separately. The off-diagonal terms are the coupling between electron and hole bands, opening the gap at the fermi energy, leading to the dispersions illustrated in figures 4.7a through d.

Projection onto lower energy band

We postulate that, by removal of the upper bands with strong magnetic fields, $V_Z \gg \alpha_R k$, the lower energy sector of the Hamiltonian in eq. (4.28) describes an effective theory for the lower bands. We justify this in appendix C. The argument presented is that, in the high field limit the second-order perturbation, from the lower-energy sector to the higher-energy sector and back, is small compared to the zeroth order perturbation in the low-energy sector. That is, in the $\Psi_- = (e^-, h^-)$ sub-space, the effective Hamiltonian is

$$\tilde{\mathcal{H}}_{2 \times 2}(k) = (\xi_k - \kappa) \tau_z + \frac{\alpha_R k \Delta}{\kappa} \tau_x.$$

Linearizing around small k , where the topological gap closes at the phase-transition,

$$\tilde{\mathcal{H}}_{2 \times 2}(k \approx 0) = -|V_Z| \tau_z + \alpha_R |k| \frac{\Delta}{|V_Z|} \tau_x,$$

having employed $\kappa \gg \xi_k$.

We are free to rotate the Hamiltonian by $R = e^{i\frac{\pi}{4}\tau_z}$, into a basis

$$R \tilde{\mathcal{H}}_{2 \times 2}(k \approx 0) R^\dagger = -|V_Z| \tau_z - \alpha_R |k| \frac{\Delta}{|V_Z|} \tau_y, \quad (4.29)$$

which is directly comparable to the *p*-wave Hamiltonian in eq. (4.13).

- $-|V_Z| \tau_z$ in eq. (4.29) corresponding to $m \tau_z$ in eq. (4.13):

The field (here) plays the role of the mass-term in the general p -wave Hamiltonian.

- $-\alpha_R |k| \frac{\Delta}{|V_Z|} \tau_y$ in eq. (4.29) corresponding to $vk\tau_y$ in (4.13):

The off-diagonal p -wave pairing in Oreg-Lutchyn model is more realistic, as it explicitly accounts for a compromise between the topological phase, and the destruction of the effective superconducting gap, when V_Z increases. In the large field limit, the states at the fermi points become more spin-polarized, hence diminishing the coupling between Cooper pairs.

In conclusion,

In proximity to a s -wave superconductor, whose Hamiltonian is given by eq. (4.25), and in the presence of a strong magnetic field, a semiconducting wire with large spin-orbit coupling (see eq. (4.24)) effectively acquires a p -wave pairing. Thus, there exists a topological regime in parameter space for said system.

Chapter 5

Scattering formalism

5.1 Preliminary concepts

5.1.1 Mesoscopic systems

A mesoscopic system is large, while also being coherent throughout. We assume the Fermi liquid picture, where quasiparticles are well-defined quantum mechanically for a short enough time scale such that they do not decay due to scattering, while also existing long enough for their energy to be well-defined. Transport is seen as a scattering problem, where scattering states extend throughout the sample. These are the key assumptions we will use when presenting the Landauer-Büttiger formalism.

The conductance is a sample-specific quantity, and in large, mesoscopic systems, it cannot be assumed to be homogenous throughout the sample. Therefore, it is inadequate to describe the system conductance locally if we want to determine the conductance of a sample. Thus, we instead employ the scattering-matrix formalism. The transmission and reflection amplitudes specifying the incoming and outgoing states make up the scattering matrix, and these can be used to solve the system, without knowing the explicit form of the wavefunction solution in the scattering region.

5.1.2 Transverse modes in conductors

Dynamics of conduction band electrons in a two-dimensional semiconductor can be modeled by the effective mass equation[24]

$$\left[E_0 + \frac{(i\hbar\nabla + e\mathbf{A})^2}{2m^*} + U(y) \right] \Psi(\mathbf{r}) = E\Psi(\mathbf{r}) \quad (5.1)$$

where E_0 is the energy at the edge of the conduction band, m^* is the constant effective mass of the electrons, and the momentum operator is given by $p_{x_i} = -i\hbar\partial_{x_i}$. \mathbf{A} is the vector-potential, $U(y)$ is a confining potential in the transverse y -direction (see figure 5.1), $\Psi(x, y)$ is the electron wavefunction, and E their eigenenergy. The solutions to

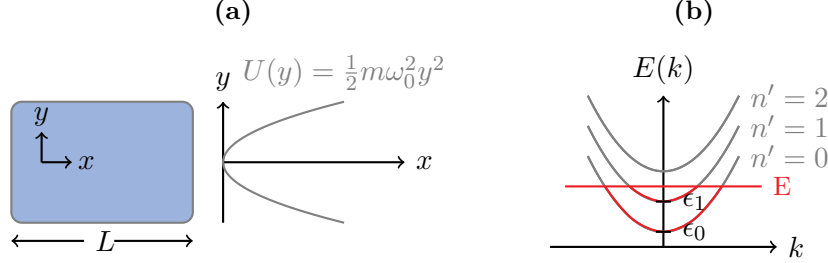


Figure 5.1: (a) A rectangular conductor of length L with a confining potential $U(y)$. This potential is assumed to be uniform in the x -direction. (b) Example of energy where states are filled up to the energy E and the number of modes is $M(E) = 2 = \Theta(E - \epsilon_0) + \Theta(E - \epsilon_1)$.

eq. (5.1) are plane waves

$$\Psi(x, y) = \frac{1}{\sqrt{L}} e^{ik_x x} \chi(y) \quad (5.2)$$

where $\chi(y)$ are transverse functions that satisfy the effective mass equation in the y -direction. We assume $|\chi(y)|$ vanishes at the edges of the conductor. Therefore, its eigenenergies are [25, sec. 13]

$$E(n, k_x) = E_0 + \frac{\hbar^2 k_x^2}{2m^*} + \left(n + \frac{1}{2}\right) \hbar\omega_0, \quad n = 0, 1, 2, \dots \quad (5.3)$$

where the n indices indicate different sub-bands, $\hbar\omega_0$ is the energy shift between each band, $\hbar^2 k_x^2 / 2m^*$ is the kinetic energy in the direction of propagation, and $\epsilon_0 = E_0 + \frac{\hbar\omega_0}{2}$ is the cut-off energy of the 0'th band. The bands are shown in figure 5.1b. Each energy mode has a lower cut-off energy $\epsilon_{n'} = E(n', k = 0)$ above which the mode can propagate. Thus, we can count the number of transverse modes available at the energy E as

$$M(E) = \sum_{n'} \Theta(E - \epsilon_{n'}) \quad (5.4)$$

where Θ is a heavy-side step-function (see figure 5.1b).

The current that each transverse mode n' carries, separately add up to the total current through the conductor, which can be measured across the sample via contacts, as shown in figure 5.2a. Without an applied bias, both contacts are at the same chemical potential $\mu_L = \mu_R$. In that case, the Fermi level of all states with some

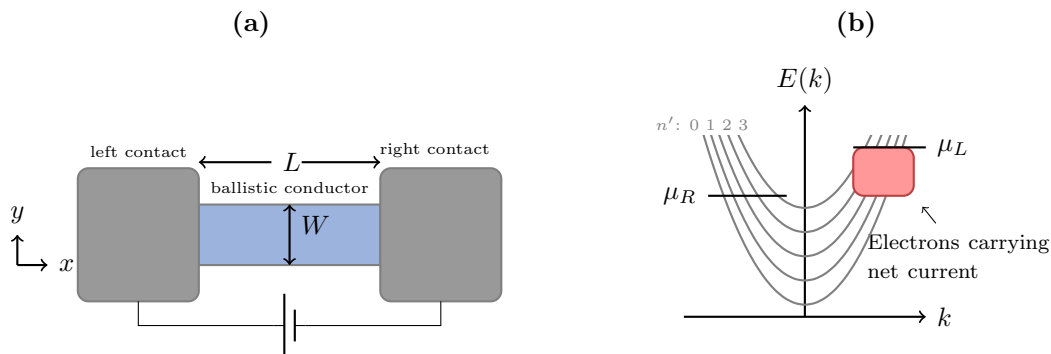


Figure 5.2: (a) A narrow conductor is connected to two wide reflectionless contacts. An external voltage bias is applied across the contacts. "Reflectionless" means electrons will scatter through the conductor-contact interface with negligible probability of reflection. "Ballistic" means there is no scattering taking place within the conductor. (b) Dispersion of the narrow conductor for different modes (sub-bands) indexed by n' . If the contacts are reflectionless, electrons with $+k_x$ wavenumber in the only originate from the left contact, while those with $-k_x$ come entirely from the right contact. The quasi-Fermi level of the $+k_x$ ($-k_x$) state is thus μ_L (μ_R).

momentum k_x (in the x -direction, assuming the conductor is sufficiently narrow that current from transverse momenta is negligible) is $\mu_L = \mu_R$. Applying a bias such that the chemical potential at the right contact is $\mu_R \neq \mu_L$, does not affect the Fermi energy of the left contact, because $+k_x$ (taking the direction of positive momentum to be left to right) states are only occupied by electrons originating from the left contact. No state from the right contact can transition into this state. Therefore, the quasi-Fermi level F_L^+ of the left lead for the $+k_x$ states is always equal to μ_L , even with an applied bias. Similarly, it can be argued that F_R^- at the right lead, belonging to the $-k_x$ states, always equals μ_R . In sum, at zero temperature and a bias such that $\mu_L > \mu_R$ (see figure 5.2b), the net current in a conductor is carried by $+k_x$ states between energies μ_L and μ_R that travel from the left to the right contact.

In the normal conductors considered so far in the current chapter, we have assumed that every mode n' that transfers current, for a given energy E (see figure 5.1b), corresponds to a single degree of freedom, and thus only one possible channel. When we consider transport in a superconductor, we need to account for four degrees of freedom per transverse mode n' , namely electrons and holes, $\{e, h\}$, and spins up or down for each of these fermions. Thus, for every mode n' (or energy band shown in figures 5.1b and 5.2b), we need to consider four channels $\{e \uparrow, e \downarrow, h \uparrow, h \downarrow\}$ in the superconductor.

5.2 S-matrix and scattering states

Consider a two-terminal system as illustrated in figure 5.3a. The system consists of

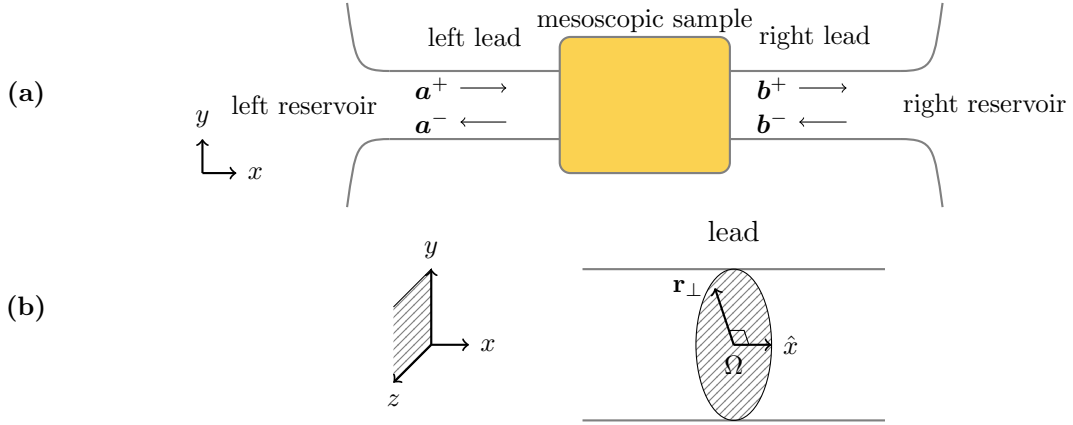


Figure 5.3: (a) Geometry of two-terminal device considered. The leads are perfect and reflectionless at their interface with the reservoirs. Eigenstates of the left and right lead are in equilibrium ('thermalized') with the very large set of states in the broad reservoirs. (b) A lead with a constant cross-section Ω in the yz -plane.

left and right reservoirs connected to two leads, left (L) and right (R), which are attached to the mesoscopic sample. For now, we do not specify if this sample is for instance a normal metal or a superconductor. The sample acts as a 'black box', where incoming probability amplitudes of transverse modes in the leads, \mathbf{a}^+ and \mathbf{b}^- , reflect or transmit into modes with amplitudes \mathbf{a}^- and \mathbf{b}^+ . The reservoirs are so wide that we can think of them as having an infinite number of transverse modes. The leads are reflectionless and the eigenstates of the leads are in equilibrium with corresponding states provided by the reservoirs (thermalized).

Assume the leads have a constant cross-section Ω along the x -direction, see figure 5.3b, and have impenetrable walls at the boundaries $\partial\Omega$. The coordinates are divided into x and a coordinate \mathbf{r}_\perp , where the latter is an arbitrary vector that lives in the yz -plane, $(x, y, z) = (x, \mathbf{r}_\perp)$. We also assume the inter-band spacing in the leads to be much larger than the relevant energy scales of the electrons and holes carrying current¹. In this way, the total number of lead channels does not depend on the energy of incident waves.

The kinetic Hamiltonian in the leads $\alpha = L, R$ can be divided into two different components: one is perpendicular ($H_{\alpha,\perp}$) and the other is parallel to the x -axis. In

¹The contacts are much wider than the leads. The smallest energy spacing between transverse modes, n and $n + 1$, is $\Delta E_n \propto (W)^{-2}$, where W is the width of the lead or the contact. With this scaling, the energy levels in the leads is necessarily much larger than said spacing in the contacts.

electron-hole space, the Hamiltonian inside the leads ($\mathbf{r}_\perp \in \Omega$) is

$$H_\alpha = \frac{p_x^2}{2m} \tau_z + \underbrace{\frac{p_\perp^2}{2m}}_{H_{\alpha,\perp}} \tau_z, \quad \text{with } \alpha = L, R, \quad (5.5)$$

where τ_z is the Pauli matrix in said space, m is the effective mass, p_x is the momentum in the x -direction, and p_\perp that in the yz -plane. The n 'th eigenstate inside the leads is a transverse wave $\chi_n(\mathbf{r}_\perp)$ moving in the positive or negative x -direction (\pm), with wave-numbers k_n , and is given by

$$\phi_{\alpha n \tau E}^\pm(x, \mathbf{r}_\perp) = \frac{1}{\sqrt{k_n(E)}} \mathbf{v}_\tau \chi_n(\mathbf{r}_\perp) e^{\pm i k_n(E) x} \quad (5.6)$$

$$\equiv \begin{pmatrix} \delta_{\tau,e} \phi_{\alpha n e E}^\pm(x, \mathbf{r}_\perp) \\ \delta_{\tau,h} \phi_{\alpha n h E}^\pm(x, \mathbf{r}_\perp) \end{pmatrix}, \quad \text{with } \tau = e, h \quad (5.7)$$

where the coordinate (x, \mathbf{r}_\perp) lies in lead α . This wavefunction is one-dimensional with units $L^{-1/2}$, L being a length unit. $\delta_{\tau,\tau'}$ is a Kronecker delta. Inspired from the BTK formalism,

$$\mathbf{v}_e = \begin{pmatrix} 1 \\ 0 \end{pmatrix}, \quad \mathbf{v}_h = \begin{pmatrix} 0 \\ 1 \end{pmatrix}$$

are respectively electron and hole spinors in electron-hole space. Note our notation where each electron or hole component $\phi_{\alpha n \tau E}^\pm(x, \mathbf{r}_\perp)$ are complex functions, while $\phi_{\alpha n \tau E}^\pm(x, \mathbf{r}_\perp)$ is a vector in electron-hole space. In the following, when τ is an index, it is either e or h , while if it is part of an expression, it is $+1$ for electrons and -1 for holes. n is the transverse mode quantum number specifying the energy band

$$E = \frac{\hbar^2 k_n^2}{2m} + \tilde{\epsilon}_n \Leftrightarrow k_n = \pm \sqrt{2m(E - \tilde{\epsilon}_n)} \quad (5.8)$$

and the transverse modes $\chi_n(\mathbf{r}_\perp)$ are the eigenstates of the perpendicular Hamiltonian with eigenenergies $\tilde{\epsilon}_n$

$$H_{\alpha,\perp} \chi_n(\mathbf{r}_\perp) = \tilde{\epsilon}_n \chi_n(\mathbf{r}_\perp). \quad (5.9)$$

Here, we simply choose the condition that the transverse Hamiltonian eigenfunctions vanish at the boundaries

$$\chi_n(\mathbf{r}_\perp = \partial\Omega) = 0$$

and do not worry about the explicit form of ϵ_n . Lastly, we assume a basis where the transverse eigenfunctions are orthogonal:

$$\langle \chi_n(\mathbf{r}_\perp) | \chi_m(\mathbf{r}_\perp) \rangle = \delta_{nm}. \quad (5.10)$$

Considerations about the probability current

The absolute probability current carried by each transverse electron or hole component in eq. (5.7) ($\lambda_\tau = \alpha n \tau E$) with velocity p_x/m through the cross-section Ω , is a constant given by

$$\int_{\Omega} d\mathbf{r}_{\perp} (\phi_{\lambda_\tau}^{\pm}(x, \mathbf{r}_{\perp}))^* \frac{p_x}{m} (\phi_{\lambda_\tau}^{\pm}(x, \mathbf{r}_{\perp})) = \pm \frac{\hbar}{m}, \quad (5.11)$$

and has units $L^2 T^{-1}$, where T is a time unit². The constant \hbar/m is independent of the momentum of the n 'th mode, k_n . In other words, we are not weighing the probability of each mode by the velocity of the mode. Instead, every mode carries the same probability current.

In order to verify eq. (5.11), we first note that one can re-write it in terms of the current density operator (with units $L T^{-1}$), given by

$$\overleftrightarrow{J}_x = \frac{\hbar}{2mi} \left(\overrightarrow{\partial}_x - \overleftarrow{\partial}_x \right), \quad (5.12)$$

such that

$$\int_{\Omega} d\mathbf{r}_{\perp} (\phi_{\lambda_\tau}^{\pm}(x, \mathbf{r}_{\perp}))^* \overleftrightarrow{J}_x (\phi_{\lambda_\tau}^{\pm}(x, \mathbf{r}_{\perp})) = \pm \frac{\hbar}{m}. \quad (5.13)$$

The arrows indicate which direction the differential operator acts. From eqs. (5.7) and (5.10), we know that the derivatives and the integral can be performed according to

$$\partial_x \phi_{\lambda_\tau}^{\pm}(x, \mathbf{r}_{\perp}) = \pm i k_n \phi_{\lambda_\tau}^{\pm}(x, \mathbf{r}_{\perp}), \quad \int d\mathbf{r}_{\perp} (\phi_{\lambda_\tau}^{\pm}(x, \mathbf{r}_{\perp}))^* \phi_{\lambda_\tau}^{\pm}(x, \mathbf{r}_{\perp}) = \frac{1}{k_n},$$

hence yielding eq. (5.11). Similarly, one obtains that states moving in opposite directions, but which are otherwise identical, yield zero net current:

$$\int_{\Omega} d\mathbf{r}_{\perp} (\phi_{\lambda_\tau}^{\pm}(x, \mathbf{r}_{\perp}))^* \overleftrightarrow{J}_x (\phi_{\lambda_\tau}^{\mp}(x, \mathbf{r}_{\perp})) = 0. \quad (5.14)$$

Eqs. (5.11) and (5.14) will become useful later.

The states in eq. (5.6) are normalized with respect to the wavenumber k in the direction of propagation x (the longitudinal lead direction), taking the form $\phi_k = \frac{1}{\sqrt{k}} e^{ikx}$ in terms of these longitudinal variables. We need to establish a sum rule that

²The unit of the one-dimensional transverse mode, for a given position x along the wire, is $[\phi_{\lambda_\tau}] = 1/L^{1/2}$, while that of the integral over the cross-section is L^2 .

relates ϕ_k to states with the usual normalization, namely $\tilde{\phi}_k = \frac{1}{\sqrt{\mathcal{L}'}} e^{ikx}$, where \mathcal{L}' is a normalization length associated with the *transverse* modes in the leads. Therefore, consider the expectation value of an arbitrary observable \hat{A} , with respect to $\tilde{\phi}_k$, and take the continuum limit for the sum over k :

$$\begin{aligned}
\sum_{k>0} \langle \tilde{\phi}_k | \hat{A} | \tilde{\phi}_k \rangle &\rightarrow \mathcal{L}' \int_0^\infty \frac{dk}{2\pi} \langle \tilde{\phi}_k | \hat{A} | \tilde{\phi}_k \rangle \\
&= \int_0^\infty \frac{dk}{2\pi} k \langle \phi_k | \hat{A} | \phi_k \rangle \\
&= \int_0^\infty \frac{dE}{2\pi} \frac{dk}{dE} k \langle \phi_k | \hat{A} | \phi_k \rangle \\
&= \frac{m}{2\pi\hbar^2} \int_0^\infty dE \langle \phi_k | \hat{A} | \phi_k \rangle
\end{aligned} \tag{5.15}$$

In the last equality, we insert for the derivative of the energy in eq. (5.8), with the notation $k = k_n$. Note that ϕ_k are not compatible with the units of the probability current in eqs. (5.11) and (5.13). Later (in eq. (5.49)), we will convert between the two representations, using eq. (5.15), when summing over all k to obtain the total current through any cross-section Ω , assuming ω is constant and identical in both leads.

Lead eigenstates in electron-hole space

The eigenstates of the leads are a linear combination of the transverse modes in eq. (5.6). Each mode ($\alpha n \tau E$) is weighed by their corresponding probability amplitude $\{a_{\tau,n}^\pm\}$ in the left lead and $\{b_{\tau,n}^\pm\}$ in the right lead, as indicated in figure 5.3a. Carefully collecting these transverse mode functions and amplitudes into vectors in a specific way that we will outline now, the lead eigenstates in electron-hole space can be written as

$$\boldsymbol{\psi}_E(x, \mathbf{r}_\perp) = \begin{pmatrix} \psi_{e,E}(x, \mathbf{r}_\perp) \\ \psi_{h,E}(x, \mathbf{r}_\perp) \end{pmatrix} \tag{5.16}$$

$$= \begin{cases} \langle \mathbf{a}^+, \boldsymbol{\phi}_{L,E}^+(x, \mathbf{r}_\perp) \rangle + \langle \mathbf{a}^-, \boldsymbol{\phi}_{L,E}^-(x, \mathbf{r}_\perp) \rangle, & (x, \mathbf{r}_\perp) \in L \\ \psi_{M,E}(x, \mathbf{r}_\perp), & (x, \mathbf{r}_\perp) \in M \\ \langle \mathbf{b}^+, \boldsymbol{\phi}_{R,E}^+(x, \mathbf{r}_\perp) \rangle + \langle \mathbf{b}^-, \boldsymbol{\phi}_{R,E}^-(x, \mathbf{r}_\perp) \rangle, & (x, \mathbf{r}_\perp) \in R, \end{cases} \tag{5.17}$$

where $\langle \cdot, \cdot \rangle$ is a product that will be defined shortly, and

$$\mathbf{a}^\pm = \begin{pmatrix} \mathbf{a}_e^\pm \\ \mathbf{a}_h^\pm \end{pmatrix}, \quad \mathbf{b}^\pm = \begin{pmatrix} \mathbf{b}_e^\pm \\ \mathbf{b}_h^\pm \end{pmatrix} \tag{5.18}$$

and $\mathbf{a}_\tau^\pm = (a_{\tau,1}^\pm, a_{\tau,2}^\pm, \dots, a_{\tau,n}^\pm, \dots)^T$ and $\mathbf{b}_\tau^\pm = (b_{\tau,1}^\pm, b_{\tau,2}^\pm, \dots, b_{\tau,n}^\pm, \dots)^T$ are vectors containing the amplitudes. Similarly, temporarily suppressing the (x, \mathbf{r}_\perp) dependence for ease of notation, we also collect the transverse modes in electron-hole space as

$$\boldsymbol{\phi}_{\alpha,E}^\pm = \left(\boldsymbol{\phi}_{\alpha e E}^\pm \quad \boldsymbol{\phi}_{\alpha h E}^\pm \right) \quad (5.19)$$

Here, the transverse modes from eq. (5.7) are assembled into the vectors $\boldsymbol{\phi}_{\alpha\tau E}^\pm$ as

$$\boldsymbol{\phi}_{\alpha\tau E}^\pm = (\phi_{\alpha 1\tau E}^\pm, \phi_{\alpha 2\tau E}^\pm, \dots, \phi_{\alpha n\tau E}^\pm, \dots).$$

$\psi_{M,E}(x, \mathbf{r}_\perp)$ and its derivative matches the lead eigenfunctions at the sample-lead interfaces. This could in principle be used to solve for the scattering amplitudes. We will instead employ the scattering formalism and the scattering-matrix, where the latter will be introduced in section 5.2.1.

The product $\langle \cdot, \cdot \rangle$ in eq. (5.17) is defined such that the resultant vector, as indicated in eq. (5.16), is a 2×1 matrix in electron-hole space with complex components. The dimension of the amplitude vectors in eq. (5.18) are $2N_L \times 1$ for the modes \mathbf{a}^\pm in the left lead, where N_L is the number of transverse modes in said lead. Analogously, \mathbf{b}^\pm has dimension $2N_R \times 1$. The vectors $\boldsymbol{\phi}_{\alpha,E}^\pm$ are of dimension $1 \times 2N_\alpha$. Simply multiplying $\mathbf{a}^+ \boldsymbol{\phi}_{L,E}^+$ would therefore yield a $2N_L \times 2N_L$ matrix. In order to have the eigenstate on the 2×1 form in eq. (5.16), we would then need to trace the diagonal electron and hole blocks separately, and have each such trace make up the electron and hole components in the eigenstate. Instead, the following product has been defined:

$$\begin{aligned} \langle \mathbf{a}^+, \boldsymbol{\phi}_{L,E}^+ \rangle &\equiv \mathbf{a}^+ \cdot (\boldsymbol{\phi}_{L,E}^+) \boldsymbol{\delta}_\phi & (5.20) \\ &\equiv \mathbf{a}^+ \left(\cdot \boldsymbol{\phi}_{LeE}^+ \quad \cdot \boldsymbol{\phi}_{LhE}^+ \right) \begin{pmatrix} \delta_{\tau(\phi),e} \\ \delta_{\tau(\phi),h} \end{pmatrix} \\ &= \begin{pmatrix} \mathbf{a}_e^+ \\ \mathbf{a}_h^+ \end{pmatrix} \left(\cdot \boldsymbol{\phi}_{LeE}^+ \delta_{\tau(\phi),e} + \cdot \boldsymbol{\phi}_{LhE}^+ \delta_{\tau(\phi),h} \right) \\ &= \begin{pmatrix} \mathbf{a}_e^+ \cdot \boldsymbol{\phi}_{LeE}^+ \times 1 + \mathbf{a}_e^+ \cdot \boldsymbol{\phi}_{LhE}^+ \times 0 \\ \mathbf{a}_h^+ \cdot \boldsymbol{\phi}_{LeE}^+ \times 0 + \mathbf{a}_h^+ \cdot \boldsymbol{\phi}_{LhE}^+ \times 1 \end{pmatrix} \\ &= \begin{pmatrix} \mathbf{a}_e^+ \cdot \boldsymbol{\phi}_{LeE}^+ \\ \mathbf{a}_h^+ \cdot \boldsymbol{\phi}_{LhE}^+ \end{pmatrix}. & (5.21) \end{aligned}$$

The Kronecker-delta $\delta_{\tau(\phi),\tau'}$ is non-zero if and only if the electron-hole index of the vector $\boldsymbol{\phi}_{L\tau E}^+$, denoted $\tau(\phi)$, equals τ' . Because the dimension of \mathbf{a}_τ^+ is $1 \times N_L$ and the dimension of $\boldsymbol{\phi}_{L\tau E}^+$ is $N_L \times 1$, each mode n are summed over implicitly inside the dot products in the last line. Therefore, the product in eq. (5.20) can be written in the

more useful component form

$$\langle \mathbf{a}^\pm, \phi_{L,E}^\pm \rangle = \sum_n \begin{pmatrix} a_{e,n}^\pm \phi_{LneE}^\pm \\ a_{h,n}^\pm \phi_{LneE}^\pm \end{pmatrix}. \quad (5.22)$$

In this form, each electron and hole block is a complex number. Eq. (5.22) is useful because we can directly insert for the relations we found for the transverse modes. The integrals (probability currents) in eqs. (5.13) and (5.14) will be most important when we calculate the current in the left and right leads in section 5.2.3. In the right lead, we analogously define the product $\langle \mathbf{b}^\pm, \phi_{L,E}^\pm \rangle$.

5.2.1 Definition of the S-matrix

The scattering matrix contains the transmission and reflection amplitudes relating modes in different leads attached to a coherent conductor. The scattering matrix the set-up depicted in figure 5.3 relates the amplitudes \mathbf{a}^+ and \mathbf{b}^- (of incoming waves $\phi_{L,E}^+$ and $\phi_{R,E}^-$ at a particular energy), to the outgoing wave amplitudes \mathbf{a}^- and \mathbf{b}^+ (of $\phi_{L,E}^-$ and $\phi_{R,E}^+$). What relates these amplitudes for the lead eigenstates is the probability amplitudes of reflection and transmission of the particular modes

$$\mathbf{c}_{\text{out}} = \mathbf{S} \mathbf{c}_{\text{in}} \quad \text{or} \quad \begin{pmatrix} \mathbf{a}^- \\ \mathbf{b}^+ \end{pmatrix} = \begin{pmatrix} \mathbf{r}_L(E) & \mathbf{t}_{LR}(E) \\ \mathbf{t}_{RL}(E) & \mathbf{r}_R(E) \end{pmatrix} \begin{pmatrix} \mathbf{a}^+ \\ \mathbf{b}^- \end{pmatrix} \quad (5.23)$$

We have defined $\mathbf{c}_{\text{out}} \equiv \begin{pmatrix} \mathbf{a}^- \\ \mathbf{b}^+ \end{pmatrix}$, $\mathbf{c}_{\text{in}} \equiv \begin{pmatrix} \mathbf{a}^+ \\ \mathbf{b}^- \end{pmatrix}$ and importantly, the scattering matrix (S-matrix) at the energy E is

$$\mathbf{S}(E) = \begin{pmatrix} \mathbf{r}_L(E) & \mathbf{t}_{LR}(E) \\ \mathbf{t}_{RL}(E) & \mathbf{r}_R(E) \end{pmatrix}. \quad (5.24)$$

For example, \mathbf{r}_L is the $N_L \times N_L$ reflection matrix relating all possible incoming with all possible outgoing electron and/or hole channels in the left lead. The scattering amplitudes (see eq. (5.18)), as well as the scattering matrices

$$\mathbf{r}_\alpha = \begin{pmatrix} r_{ee,\alpha} & r_{eh,\alpha} \\ r_{he,\alpha} & r_{hh,\alpha} \end{pmatrix}, \quad \mathbf{t}_{\bar{\alpha}\alpha} = \begin{pmatrix} t_{ee,\bar{\alpha}\alpha} & t_{eh,\bar{\alpha}\alpha} \\ t_{he,\bar{\alpha}\alpha} & t_{hh,\bar{\alpha}\alpha} \end{pmatrix}, \quad (5.25)$$

are specified as 2×2 blocks in electron-hole space, where the dimension of each component of these matrices is given by the number of channels in each lead.

Number of channels and probabilities from the S-matrix

Let $\{a_i\}$ be the incident mode and $\{b_i\}$ be the outgoing mode amplitudes, and the index i denote the channel. For instance, with a total of three channels, the S-matrix relates the two as follows:

$$\begin{pmatrix} b_1 \\ b_2 \\ b_3 \end{pmatrix} = \begin{pmatrix} s_{11} & s_{12} & s_{13} \\ s_{21} & s_{22} & s_{23} \\ s_{31} & s_{32} & s_{33} \end{pmatrix} \begin{pmatrix} a_1 \\ a_2 \\ a_3 \end{pmatrix}.$$

The S-matrix has dimension 3×3 and is specified at an energy E . Note that we have not specified a geometry of the sample. This scattering matrix could represent both a one, two and three-terminal set-up.

In general, the total number of channels at an energy E , is the sum over all channels $N_\alpha(E)$ for each lead α ,

$$N_{\text{total channels}}(E) = \sum_{\alpha} N_{\alpha}(E),$$

and the S-matrix must have the dimension

$$N_{\text{total channels}}(E) \times N_{\text{total channels}}(E).$$

The transmission or reflection probability $T_{n'n}$ of each scattering event from channel n to n' of some lead(s), is given by the absolute square of the probability amplitude $|s_{n'n}(E)|^2$, where $s_{n'n}(E)$ is the (n', n) matrix element of the S-matrix.

Let the number of modes in the left and right leads be N_L and N_R , respectively. Then, the S-matrix is a block matrix with dimensions

$$\left(\begin{array}{c|c} N_L \times N_L & N_L \times N_R \\ \hline N_R \times N_L & N_R \times N_R \end{array} \right) \text{ or } 2 \times 2 \text{ in lead space.}$$

In every channel in the leads, an incoming electron or hole has to undergo one of the possible physical scattering processes. The individual blocks $r_{ee,\alpha}$ ($t_{ee,\bar{\alpha}\alpha}$) et cetera are $N_\alpha \times N_\alpha$ ($N_{\bar{\alpha}} \times N_\alpha$) dimensional matrices, containing the scattering amplitudes of electrons and holes incident in N_α channels and reflecting (transmitting) into N_α ($N_{\bar{\alpha}}$) lead channels.

When the sample is superconducting, an electron in the left lead can undergo either normal reflection, reflecting back as an electron (with reflection amplitudes $r_{ee,L}$), normal transmission, transmitting to the opposite lead as an electron ($t_{ee,RL}$), Andreev reflection, reflecting as an electron and transmitting a Cooper pair into the superconductor ($r_{he,L}$), or *crossed Andreev reflection* (CAR), transmitting through to the opposite lead as a hole ($t_{he,RL}$). The same types of processes occur for an

electron incident in the right lead ($\alpha = R$). For every electron scattering, such as those contained in $r_{ee,\alpha}$, there are corresponding hole processes, such as $r_{hh,\alpha}$. The corresponding probability amplitudes are all contained in the matrices in eq. (5.25).

As an illustration of how the scattering matrices can account for all these processes, consider writing out eq. (5.23) explicitly as

$$\begin{pmatrix} \mathbf{a}^- \\ \mathbf{b}^+ \end{pmatrix} = \begin{pmatrix} \mathbf{r}_L \mathbf{a}^+ + \mathbf{t}_{LR} \mathbf{b}^- \\ \mathbf{t}_{RL} \mathbf{a}^+ + \mathbf{r}_R \mathbf{b}^- \end{pmatrix}. \quad (5.26)$$

Eq. (5.26) has amplitudes such as

$$\mathbf{r}_L \mathbf{a}^+ = \begin{pmatrix} r_{L,ee} \mathbf{a}_e^+ + r_{L,eh} \mathbf{a}_h^+ \\ r_{L,he} \mathbf{a}_e^+ + r_{L,hh} \mathbf{a}_h^+ \end{pmatrix} = \begin{pmatrix} e \text{ reflected out L from } e \text{ or } h \\ h \text{ reflected out L from } e \text{ or } h \end{pmatrix}$$

which incorporates all normal and Andreev reflection processes, by which incoming electrons (first line) and holes (second line) in the left lead are reflected back into the same lead. Similarly, transmission from states originating in the right lead give rise to amplitudes

$$\mathbf{t}_{LR} \mathbf{b}^- = \begin{pmatrix} e \text{ transmitted in L from } e \text{ or } h \\ h \text{ transmitted in L from } e \text{ or } h \end{pmatrix}$$

in the left lead. The sum of these reflected and transmitted components make up \mathbf{a}^- , which is the resultant total amplitude of modes going out of the left lead, given in electron-hole space. Similarly, \mathbf{b}^+ is the sum of all outgoing amplitudes in the right lead.

5.2.2 Conservation of probability current

The scattering matrix formalism is powerful and simple due to the conservation of probability current. This conservation law demands that:

The incoming probability of an electron *or* hole through a cross-section Ω somewhere in lead α (summing over all n channels of incoming electrons *or* holes), must equal the sum over all outgoing (reflected and transmitted) probabilities through the same cross-section.

In terms of \mathbf{c}_{in} and \mathbf{c}_{out} , the conservation of probability current reads

$$\sum_n |c_{\text{in},n}|^2 = \sum_n |c_{\text{out},n}|^2 \quad \text{or} \quad \mathbf{c}_{\text{in}}^\dagger \mathbf{c}_{\text{in}} = \mathbf{c}_{\text{out}}^\dagger \mathbf{c}_{\text{out}}. \quad (5.27)$$

Considering eq. (5.27) and inserting for \mathbf{c}_{out} from eq. (5.23), we obtain

$$\mathbf{c}_{\text{in}}^\dagger \mathbf{c}_{\text{in}} = \mathbf{c}_{\text{in}}^\dagger \mathbf{S}^\dagger \mathbf{S} \mathbf{c}_{\text{in}}.$$

The only way for this to hold is if *the S-matrix is unitary*, which explicitly means that

$$\mathbf{S}^\dagger \mathbf{S} = \mathbf{1} \text{ or } \begin{cases} \mathbf{1}_{N_L \times N_L} = \mathbf{r}_L^\dagger \mathbf{r}_L + \mathbf{t}_{RL}^\dagger \mathbf{t}_{RL}, & \mathbf{1}_{N_R \times N_R} = \mathbf{r}_R^\dagger \mathbf{r}_R + \mathbf{t}_{LR}^\dagger \mathbf{t}_{LR} \\ \mathbf{0}_{N_L \times N_R} = \mathbf{r}_L^\dagger \mathbf{t}_{LR} + \mathbf{t}_{RL}^\dagger \mathbf{r}_R, & \mathbf{0}_{N_R \times N_L} = \mathbf{r}_R^\dagger \mathbf{t}_{RL} + \mathbf{t}_{LR}^\dagger \mathbf{r}_L, \end{cases} \quad (5.28)$$

for incoming electrons and holes separately. The identity matrix $\mathbf{1}$ has dimension $(N_L + N_R) \times (N_L + N_R)$. Similarly,

$$\mathbf{S} \mathbf{S}^\dagger = \mathbf{1} \text{ or } \begin{cases} \mathbf{1}_{N_L \times N_L} = \mathbf{r}_L \mathbf{r}_L^\dagger + \mathbf{t}_{LR} \mathbf{t}_{LR}^\dagger, & \mathbf{1}_{N_R \times N_R} = \mathbf{r}_R \mathbf{r}_R^\dagger + \mathbf{t}_{RL} \mathbf{t}_{RL}^\dagger \\ \mathbf{0}_{N_L \times N_R} = \mathbf{r}_L \mathbf{t}_{RL}^\dagger + \mathbf{t}_{LR} \mathbf{r}_R^\dagger, & \mathbf{0}_{N_R \times N_L} = \mathbf{r}_R \mathbf{t}_{LR}^\dagger + \mathbf{t}_{RL} \mathbf{r}_L^\dagger. \end{cases} \quad (5.29)$$

In eqs. (5.28) and (5.29), there are four equations that are equal to the identity. These correspond to the diagonal (α, α) blocks of $\mathbf{S}^\dagger \mathbf{S}$ and $\mathbf{S} \mathbf{S}^\dagger$ in lead space. If we trace over all the channels in each of these blocks, we obtain that the number of modes ($\text{Tr} \mathbf{1}_{N_\alpha \times N_\alpha} = \sum_n^{N_\alpha} 1 = N_\alpha$ on the left hand side), must equal the sum of all scattering probabilities (right hand side) for processes ending up in lead α . For ease of notation, we re-cast the traces for incoming electrons in lead α as

$$\begin{aligned} R_\alpha^e &= \text{Tr} \{ r_{ee,\alpha}^\dagger r_{ee,\alpha} \}, & T_{\bar{\alpha}\alpha}^e &= \text{Tr} \{ t_{ee,\bar{\alpha}\alpha}^\dagger t_{ee,\bar{\alpha}\alpha} \} \\ A_\alpha^e &= \text{Tr} \{ r_{he,\alpha}^\dagger r_{he,\alpha} \}, & A_{\bar{\alpha}\alpha}^e &= \text{Tr} \{ t_{he,\bar{\alpha}\alpha}^\dagger t_{he,\bar{\alpha}\alpha} \}. \end{aligned} \quad (5.30)$$

where the energy-dependence is implied. Respectively, $R_\alpha^e(E)$ and $A_\alpha^e(E)$ are the normal and Andreev reflection probabilities of an incident electron in lead α . The transmission probability of an electron from lead α to lead $\bar{\alpha}$ is $T_{\bar{\alpha}\alpha}^e(E)$, while $A_{\bar{\alpha}\alpha}^e(E)$ is the probability of CAR of an electron in lead α *transmitting as a hole* into lead $\bar{\alpha}$. Analogous probabilities can be defined for incoming holes.

Tracing over the diagonal blocks of $\mathbf{S}^\dagger \mathbf{S}$ in eq. (5.28) for incoming electrons, and inserting for the probabilities in eq. (5.30), yields

$$R_\alpha^e(E) + A_\alpha^e(E) + T_{\bar{\alpha}\alpha}^e(E) + A_{\bar{\alpha}\alpha}^e(E) = N_\alpha. \quad (5.31)$$

The total probability of all possible scattering processes an electron with energy E in lead α can undergo (the left-hand side of eq. (5.31)), must equal the total number of channels in the same lead (right-hand side). This conservation law is illustrated in figure 5.4a for an electron originating from the left lead ($\alpha = L$). The picture

in figure 5.4a is valid for energies above and below the superconducting gap alike, because we only consider probabilities that may be measured in the normal leads, while what goes on inside the sample and the superconducting lead is a "black box". If the energy of the incident electron is lower than the superconducting gap of the

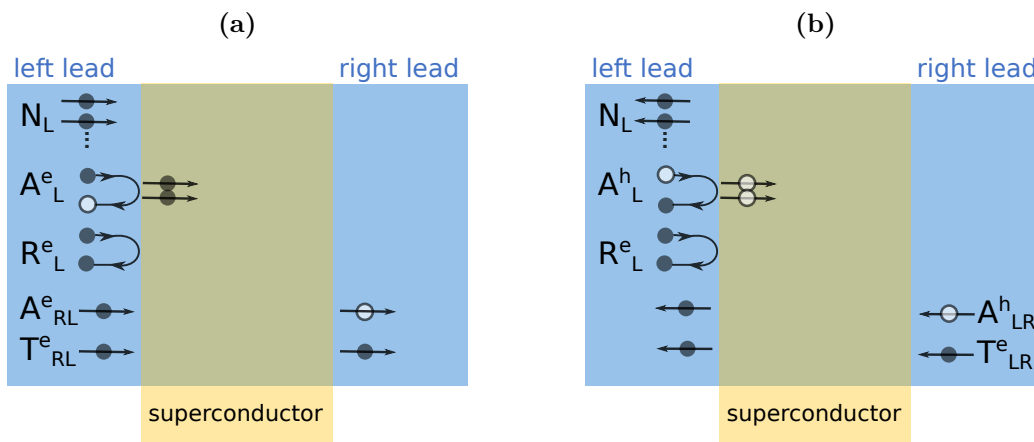


Figure 5.4: Illustration of the possible scattering processes for an electron, that sum up to the total number of channels in the left lead for a given energy. (a) Shows processes that incoming electrons can undergo, while (b) shows where outgoing electrons may originate from. This figure is meant to serve as a pictorial: In reality, it is the total probability currents that are conserved, thus we cannot actually access these depicted probability amplitudes individually.

proximitized superconductor, only Cooper pairs may carry current inside the sample. In terms of quasiparticle current, the three-terminal device thus becomes two-terminal for sub-gap energies.

Similarly, by tracing over the diagonal blocks of $\mathbf{S}\mathbf{S}^\dagger$ in eq. (5.29) for an incoming electron, we obtain another conservation law, namely

$$R_\alpha^e(E) + A_\alpha^h(E) + T_{\alpha\bar{\alpha}}^e(E) + A_{\alpha\bar{\alpha}}^h(E) = N_\alpha. \quad (5.32)$$

This law describes the fact that the electrons filling up the total number of channels in lead α must have originated from somewhere. This is illustrated in figure 5.4b. Similar conservation laws are obtained for holes (interchanging e and h indices in eqs. (5.31) and (5.32)), and results from tracing over the hole block in the diagonal blocks of eqs. (5.28) and (5.29), instead of the electron blocks. The two laws of eqs. (5.31) and (5.32) become key in our treatment of symmetry relations in the differential conductance later, in chapter 8.

5.2.3 Calculating the current

In the following, we derive the explicit expression for the current in either lead, as a function of the scattering amplitudes. This enables one to utilize the power of the scattering formalism presented in section 5.2. In particular, the conservation of probability current, as summarized by eqs. (5.31) and (5.32), and the unitarity of the S-matrix are key.

The electronic particle current through a cross-section Ω for a given wavefunction in electron-hole space, $\Psi(x, \mathbf{r}_\perp) = (\Psi_e(x, \mathbf{r}_\perp), \Psi_h(x, \mathbf{r}_\perp))^T$, is commonly given in the form

$$I(x) = \frac{1}{2mi} \int_{\Omega} d\mathbf{r}_\perp \Psi(x, \mathbf{r}_\perp)^\dagger \tau_z [\partial_x \Psi(x, \mathbf{r}_\perp)] - [\partial_x \Psi(x, \mathbf{r}_\perp)^\dagger] \tau_z \Psi(x, \mathbf{r}_\perp).$$

We re-write this expression, in terms of the current density operator (see eq. (5.12)), as

$$\begin{aligned} I(x) &= \int_{\Omega} d\mathbf{r}_\perp \Psi^\dagger(x, \mathbf{r}_\perp) \overset{\leftrightarrow}{J}_x \tau_z \Psi(x, \mathbf{r}_\perp) \\ &= \int_{\Omega} d\mathbf{r}_\perp \left(\Psi_e^*(x, \mathbf{r}_\perp) \overset{\leftrightarrow}{J}_x \Psi_e(x, \mathbf{r}_\perp) - \Psi_h^*(x, \mathbf{r}_\perp) \overset{\leftrightarrow}{J}_x \Psi_h(x, \mathbf{r}_\perp) \right). \end{aligned} \quad (5.33)$$

In the last line, we see explicitly that the Pauli matrix τ_z in electron-hole space ensures there is an extra minus sign in front of contributions from holes.

In order to relate the current in eq. (5.33) to the probability amplitudes in each lead, we can insert for the eigenstate wavefunction $\psi_E(x, \mathbf{r}_\perp)$ (see eq. (5.17)). Doing this in the left lead, $(x, \mathbf{r}_\perp) \in L$, we have the following total current from both electrons and holes of energy E :

$$I_{L,E}(x) = \int d\mathbf{r}_\perp (\langle \mathbf{a}^+, \phi_{L,E}^+ \rangle + \langle \mathbf{a}^-, \phi_{L,E}^- \rangle)^\dagger \overset{\leftrightarrow}{J}_x \tau_z (\langle \mathbf{a}^+, \phi_{L,E}^+ \rangle + \langle \mathbf{a}^-, \phi_{L,E}^- \rangle) \quad (5.34)$$

We expand the brackets in eq. (5.34). Writing out the products (see eq. (5.22)) and using the normalization condition in eq. (5.13), and the orthogonality relation in eq.

(5.14), the term with waves moving in the same and positive direction is

$$\begin{aligned}
& \int d\mathbf{r}_\perp \langle \mathbf{a}^+, \boldsymbol{\phi}_{L,E}^+ \rangle^\dagger \overleftrightarrow{J}_x \tau_z \langle \mathbf{a}^+, \boldsymbol{\phi}_{L,E}^+ \rangle \\
&= \int d\mathbf{r}_\perp \sum_n \left((a_{e,n}^+ \phi_{LneE}^+)^*, (a_{h,n}^+ \phi_{LnhE}^+)^* \right) \overleftrightarrow{J}_x \sum_{n'} \begin{pmatrix} a_{e,n'}^+ \phi_{Ln'eE}^+ \\ -a_{h,n'}^+ \phi_{Ln'eE}^+ \end{pmatrix} \\
&= \frac{\hbar}{m} \sum_{nm'} \left((a_{e,n}^+)^* a_{e,n'}^+ - (a_{h,n}^+)^* a_{h,n'}^+ \right) \delta_{n,n'} \\
&= \frac{\hbar}{m} \left(|\mathbf{a}_e^+|^2 - |\mathbf{a}_h^+|^2 \right) = \frac{\hbar}{m} (\mathbf{a}^+)^\dagger \tau_z (\mathbf{a}^+).
\end{aligned}$$

This renders the current independent of the x -coordinate in the lead, as is expected because the current through every cross-section in the lead must be identical if current is conserved throughout the lead. The cross-terms are each zero, due to the orthogonality condition which can be expressed as in eq. (5.14). Similarly, the left-moving waves are

$$\int d\mathbf{r}_\perp \langle \mathbf{a}^-, \boldsymbol{\phi}_{L,E}^- \rangle^\dagger \overleftrightarrow{J}_x \tau_z \langle \mathbf{a}^-, \boldsymbol{\phi}_{L,E}^- \rangle = \frac{\hbar}{m} (\mathbf{a}^-)^\dagger \tau_z (\mathbf{a}^-).$$

From the definition of the S-matrix (see eq. (5.23)), the outgoing amplitudes \mathbf{a}^- can be re-written in terms of *only incident amplitudes*, as in eq. (5.26). Thus, the total current in the left lead, from left and right-moving modes, becomes

$$\begin{aligned}
I_{L,E} &= \frac{\hbar}{m} \left[(\mathbf{a}^+)^\dagger \tau_z (\mathbf{a}^+) - (\mathbf{a}^-)^\dagger \tau_z (\mathbf{a}^-) \right] \\
&= \frac{\hbar}{m} \left(\underbrace{(\mathbf{a}^+)^\dagger \tau_z (\mathbf{a}^+)}_{\text{incident}} - \underbrace{(\mathbf{r}_L \mathbf{a}^+ + \mathbf{t}_{LR} \mathbf{b}^-)^\dagger \tau_z (\mathbf{r}_L \mathbf{a}^+ + \mathbf{t}_{LR} \mathbf{b}^-)}_{\text{scattered}} \right), \quad (5.35)
\end{aligned}$$

where terms with the incident and scattered amplitudes are separate.

Inserting for the eigenstate in the right lead, similarly to in eq. (5.34), and carrying out the same steps as was done through to eq. (5.35) (this time inserting for \mathbf{b}^+ given in eq. (5.26)), yields

$$I_{R,E} = \frac{\hbar}{m} \left(- \underbrace{(\mathbf{b}^-)^\dagger \tau_z (\mathbf{b}^-)}_{\text{incident}} + \underbrace{(\mathbf{t}_{RL} \mathbf{a}^+ + \mathbf{r}_R \mathbf{b}^-)^\dagger \tau_z (\mathbf{t}_{RL} \mathbf{a}^+ + \mathbf{r}_R \mathbf{b}^-)}_{\text{scattered}} \right). \quad (5.36)$$

Now that we have the electronic current in each lead, expressed in terms of the incident scattering amplitudes \mathbf{a}^+ and \mathbf{b}^- , it is time to insert for *scattering states*.

5.2.1: Term-wise identical left and right currents

We may also introduce a slight re-writing by expanding the squares in eqs. (5.35) and (5.36) and collecting terms with the same amplitudes as

$$I_{L,E} = \frac{\hbar}{m} \left\{ (\mathbf{a}^+)^\dagger \left(\tau_z - \mathbf{r}_L^\dagger \tau_z \mathbf{r}_L \right) \mathbf{a}^+ - (\mathbf{b}^-)^\dagger \mathbf{t}_{LR}^\dagger \tau_z \mathbf{t}_{LR} \mathbf{b}^- \right. \\ \left. - 2Re \left[(\mathbf{a}^+)^\dagger \mathbf{r}_L^\dagger \tau_z \mathbf{t}_{LR} \mathbf{b}^- \right] \right\} \quad (5.37)$$

and

$$I_{R,E} = \frac{\hbar}{m} \left\{ (\mathbf{b}^-)^\dagger \left(-\tau_z + \mathbf{r}_R^\dagger \tau_z \mathbf{r}_R \right) \mathbf{b}^- + (\mathbf{a}^+)^\dagger \mathbf{t}_{RL}^\dagger \tau_z \mathbf{t}_{RL} \mathbf{a}^+ \right. \\ \left. + 2Re \left[(\mathbf{a}^+)^\dagger \mathbf{t}_{RL}^\dagger \tau_z \mathbf{r}_R \mathbf{b}^- \right] \right\} \quad (5.38)$$

In this form, the incident and scattered contributions are no longer grouped separately. Since the left and right leads are identical, our model does not distinguish between the two. To be specific, each incoming and outgoing term in eqs. (5.37) and (5.38) must match, which corresponds exactly to the S-matrix being unitary (see eq. (5.28)).

5.2.4 Scattering states

In calculating the current, we have so far considered a mesoscopic sample with leads connected to reservoirs (see figure 5.3a). Let us now focus our attention on only the sample and the leads, as depicted in figure 5.5a, while keeping the assumptions of the reservoirs (the thermalization of transverse lead modes with said reservoirs) implicit.

When the scattering region is coupled to the leads, the lead eigenstates $\psi_{E,\alpha}(x, \mathbf{r}_\perp)$ become *scattering states*. If transport is coherent along the whole sample, a single wavefunction, the *scattering state*, extends all the way from one lead to another in the set-up. Therefore, as long as the scattering state is occupied in one lead, it may carry current to and from another lead. We restrict our attention to incident modes in the normal leads with sub-gap energies, such that there is no quasiparticle current in the superconducting regions.

Scattering states, $\Psi_{\alpha n \tau E}$, in a two-terminal device, consist of:

1. an incoming wave in a transverse lead mode ($\phi_{\alpha n \tau E}^+$ for lead α , see eq. (5.7)),

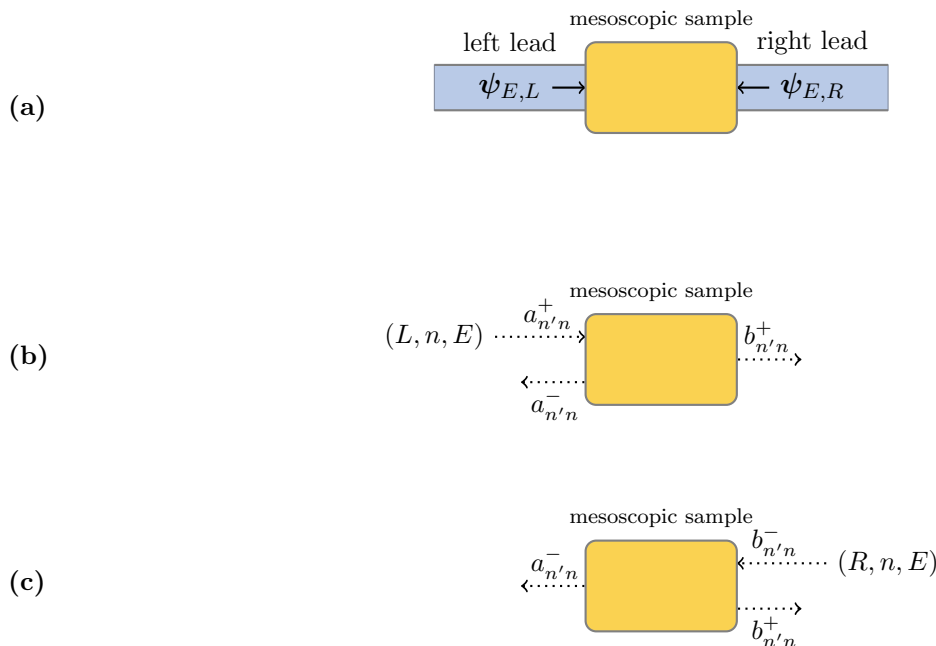


Figure 5.5: (a) Lead eigenstates incident on the mesoscopic sample. The left (b) and right (c) scattering states $\psi_{\alpha n E}$ possible in a two-terminal set-up, each consisting of incident and scattered waves inside the leads, each with their own incoming and outgoing coefficients specifying the probability amplitude of scattering into mode n' . All τ indices have been suppressed in (c) and (d).

2. the reflected wave in the same lead, *and*
3. a transmitted wave in the opposite lead.

The possible incident and scattered states are denoted by indices (α', n', τ', E) , while the total scattering state, which sums over all these possible states, have different indices (α, n, τ, E) (except for the energy, which is conserved). The probability amplitudes, associated with scattering states in the left ($a_{n'n}^\pm$ scattering from mode n to n' in the left lead) and right ($b_{n'n}^\pm$) leads, are illustrated in figure 5.5b and 5.5c. The τ index is suppressed to avoid cluttering.

If the sample is superconducting, the picture in these two figures needs to be applied to both electrons and holes. For instance, if the incident mode is an electron, this mode can reflect and transmit into either an electron or a hole. Therefore, the scattering state consists of an incident wave, which is either an electron or a hole, plus the sum over both reflected and transmitted electron and hole waves. In what follows,

we assume the sample is superconducting, and explicitly show how to incorporate both the electron and hole degrees of freedom in the formalism.

For the two-terminal set-up with a coherent, superconducting sample, these waves in the different sections, the left lead (L), the scattering region in the middle (M), and the right lead (R), constitute the following scattering state in the left lead:

$$\Psi_{Ln\tau E}(x, \mathbf{r}_\perp) = \begin{cases} \sum_{n'} \left[\delta_{n'n} \phi_{Ln'\tau E}^+(x, \mathbf{r}_\perp) + \sum_{\tau'} (r_{\tau'\tau, L})_{n'n} \phi_{Ln'\tau' E}^-(x, \mathbf{r}_\perp) \right], & (x, \mathbf{r}_\perp) \in L \\ \psi_{M, E}(x, \mathbf{r}_\perp), & (x, \mathbf{r}_\perp) \in M \\ \sum_{n'} \sum_{\tau'} (t_{\tau'\tau, RL})_{n'n} \phi_{Rn'\tau' E}^+(x, \mathbf{r}_\perp), & (x, \mathbf{r}_\perp) \in R. \end{cases} \quad (5.39)$$

1. The first line is the contribution from the incident wave (shown with the amplitude of the wave, $a_{n'n}^+$, in figure 5.5b), and
2. the two reflected waves ($a_{n'n}^-$ in figure 5.5b), as seen by simply splitting up the sum over τ' into two parts: one for normal reflection, with the coefficient $(r_{\tau\tau, L})_{nn'}$, and another accounting for Andreev reflection, with the coefficient $(r_{\bar{\tau}\tau, L})_{nn'}$, where $\bar{\tau} \neq \tau$.
3. The lowest line is the sum of the normally transmitted and cross-Andreev reflected wave in the right lead ($b_{n'n}^+$ in figure 5.5b).

We could in principle use the Dirichlét boundary conditions at the boundaries of M with L and R , and solve for the unknown wavefunction $\psi_{M, E}(x, \mathbf{r}_\perp)$ inside the sample. This is not necessary when using scattering states, because we have assumed the sample is coherent throughout. Similarly, the right scattering state is (see figure 5.5c)

$$\Psi_{Rn\tau E}(x, \mathbf{r}_\perp) = \begin{cases} \sum_{n'} \sum_{\tau'} (t_{\tau'\tau, LR})_{n'n} \phi_{Ln'E}^-(x, \mathbf{r}_\perp), & (x, \mathbf{r}_\perp) \in L \\ \psi_{M, E}(x, \mathbf{r}_\perp), & (x, \mathbf{r}_\perp) \in M \\ \sum_{n'} \left[\delta_{n'n} \phi_{Rn'\tau E}^-(x, \mathbf{r}_\perp) + \sum_{\tau'} (r_{\tau'\tau, R})_{n'n} \phi_{Rn'\tau' E}^+(x, \mathbf{r}_\perp) \right], & (x, \mathbf{r}_\perp) \in R. \end{cases} \quad (5.40)$$

The scattering states $\psi_{\alpha n \tau E}$ consist of waves in *both* the left and the right leads, and carries current as long as it is occupied. Therefore, inserting for the amplitudes of the scattering states into eqs. (5.35) and (5.36) will yield the total current in the respective leads.

Consider an incident electron or hole, denoted by the index τ . We can read off what these amplitudes \mathbf{a}^+ and \mathbf{b}^- are for the scattering states in eqs. (5.39) and

(5.40) (also see figure 5.5b and (c)) as³

$$(\mathbf{a}^+ \text{ of } \psi_{Ln\tau E})_{n'} = \delta_{nn'} \mathbf{v}_\tau, \quad (\mathbf{b}^- \text{ of } \psi_{Ln\tau E})_{n'} = 0, \quad (5.41)$$

and

$$(\mathbf{a}^+ \text{ of } \psi_{Rn\tau E})_{n'} = 0, \quad (\mathbf{b}^- \text{ of } \psi_{Rn\tau E})_{n'} = \delta_{nn'} \mathbf{v}_\tau. \quad (5.42)$$

The electron-hole spinor ensures that, if the incident mode is an electron (hole), only the electron (hole) component of \mathbf{a}^+ or \mathbf{b}^- is non-zero.

For instance, inserting for the left scattering state (eq. (5.41)) for an incident electron or hole, τ , into the current in the left lead (see eq. (5.35)), the calculation becomes simple: All terms with \mathbf{b}^- are zero, leaving only the current due to the incident modes in the left lead as

$$\begin{aligned} I_{L\tau E} &= \frac{\hbar}{m} \left((\mathbf{a}^+)^\dagger \tau_z (\mathbf{a}^+) - (\mathbf{r}_L \mathbf{a}^+)^\dagger \tau_z (\mathbf{r}_L \mathbf{a}^+) \right) \\ &= \frac{\hbar}{m} \tau (\mathbf{a}_\tau^+)^\dagger \left(1 - \left[\mathbf{r}_{\tau\tau,L}^\dagger \mathbf{r}_{\tau\tau,L} - \mathbf{r}_{\bar{\tau}\tau,L}^\dagger \mathbf{r}_{\bar{\tau}\tau,L} \right] \right) \mathbf{a}_\tau^+. \end{aligned}$$

Inserting for the explicit form of \mathbf{a}^+ from the scattering state in eq. (5.41), the first term in the above is the trace

$$(\mathbf{a}_\tau^+)^\dagger \mathbf{a}_\tau^+ = \sum_n^{N_L} (a_{\tau,n}^+)^* a_{\tau,n}^+ = Tr \{ \mathbf{1}_{N_L \times N_L} \}.$$

In the first equality, we identify the fact that \mathbf{a}_τ^+ is a $N_L \times 1$ vector, where each element n corresponds to the n 'th mode (see below eq. (5.18)). From eq. (5.41), all these amplitudes are 1, which can be written as the trace over modes n as shown, or simply N_L . Similarly, and inserting for the normal and Andreev reflection probabilities (see eq. (5.30)), the second term in $I_{L\tau E}$ becomes

$$(\mathbf{a}_\tau^+)^\dagger \left[\mathbf{r}_{\tau\tau,L}^\dagger \mathbf{r}_{\tau\tau,L} - \mathbf{r}_{\bar{\tau}\tau,L}^\dagger \mathbf{r}_{\bar{\tau}\tau,L} \right] \mathbf{a}_\tau^+ = Tr \left\{ \mathbf{r}_{\tau\tau,L}^\dagger \mathbf{r}_{\tau\tau,L} - \mathbf{r}_{\bar{\tau}\tau,L}^\dagger \mathbf{r}_{\bar{\tau}\tau,L} \right\}.$$

In other words,

$$I_{L\tau E} = \frac{\hbar}{m} \tau Tr \left\{ \mathbf{1}_{N_L \times N_L} - \left[\mathbf{r}_{\tau\tau,L}^\dagger \mathbf{r}_{\tau\tau,L} - \mathbf{r}_{\bar{\tau}\tau,L}^\dagger \mathbf{r}_{\bar{\tau}\tau,L} \right] \right\}. \quad (5.43)$$

³Since the scattering state is always occupied, the amplitudes are either exactly 1 or 0 as described in eqs. (5.41) and (5.42).

Similarly, we insert for the scattering state originating from incident modes in the right lead (eq. (5.42)) into eq. (5.36). The resulting current due to electronic or hole modes, τ , incident in the right lead is

$$I_{R\tau E} = -\frac{\hbar}{m} \tau \text{Tr} \left\{ \mathbf{1}_{N_R \times N_R} - \left[\mathbf{r}_{\tau\tau,R}^\dagger \mathbf{r}_{\tau\tau,R} - \mathbf{r}_{\bar{\tau}\tau,R}^\dagger \mathbf{r}_{\bar{\tau}\tau,R} \right] \right\}. \quad (5.44)$$

The direction of positive current is into the scattering region. Thus the direction $I_{R\tau E}$ is opposite to that of $I_{L\tau E}$ when compared in real space, and the form in eq. (5.44) has an extra negative sign compared to eq. (5.43).

Explicitly accounting for the sign of the holes in the unitarity conditions in eq. (5.28), we have that, for general leads $\alpha \neq \bar{\alpha}$,

$$\mathbf{1}_{2N_\alpha \times 2N_\alpha} - \mathbf{r}_{\alpha\tau}^\dagger \tau_z \mathbf{r}_\alpha = \mathbf{t}_{\bar{\alpha}\alpha}^\dagger \tau_z \mathbf{t}_{\bar{\alpha}\alpha}.$$

Inserting for this into eq. (5.44), one obtains the current in the left lead, due to the incident electron or hole (τ) modes in the right lead:

$$I_{LR\tau E} = -\frac{\hbar}{m} \tau \text{Tr} \left\{ \mathbf{t}_{\tau\tau,LR}^\dagger \mathbf{t}_{\tau\tau,LR} - \mathbf{t}_{\bar{\tau}\tau,LR}^\dagger \mathbf{t}_{\bar{\tau}\tau,LR} \right\} \quad (5.45)$$

The result of these traces are given by the reflection and transmission probabilities (see eq. (5.30)). The calculations leading to the local current in the left lead in eq. (5.43), and the nonlocal current in eq. (5.45), are identical when interchanging the lead indices, due to the inversion-symmetry of the system. Therefore, the local and nonlocal currents, at any cross-section in lead α , are

$$I_{\alpha\tau E} = \frac{\hbar}{m} \tau \{ N_\alpha - [R_\alpha^\tau(E) - A_\alpha^\tau(E)] \}, \quad (5.46)$$

$$I_{\alpha\bar{\alpha}\tau E} = -\frac{\hbar}{m} \tau \{ T_{\alpha\bar{\alpha}}^e(E) - A_{\alpha\bar{\alpha}}^e(E) \}. \quad (5.47)$$

We remind the reader that the local current in lead α originates from the scattering state incident in the same lead, while the non-local current in lead α is due to the scattering state forming from incident modes in lead $\bar{\alpha}$. The sign convention is such that the direction of positive current is from lead α into the sample.

As argued earlier, with wide contacts and reflectionless leads, electrons and holes incident on the sample have the same chemical potential μ_α as the reservoir that is connected to the lead. Thus, a particle in lead α with energy E has the occupation given by integrating the Fermi-Dirac distribution

$$f(E - \mu_\alpha) \quad (5.48)$$

with respect to energy, where $f(E) = [e^{\beta E} + 1]^{-1}$, $\beta = 1/k_B T$ is the inverse temperature, and k_B is the Boltzmann constant. For each mode n in either lead, the total electric current is found by integrating over the local and nonlocal probability currents, weighed by the probability distribution of the lead where the scattering state originated from, for each energy E . The corresponding total local or nonlocal current through any cross-section of either lead is then found by summing over all channels in the respective lead. We choose to multiply by the electronic charge $-e$ to incorporate the charge unit. Hence, the total electric current measured at any cross-section in lead α is

$$I_{e,\alpha} = -e \times \left[\sum_n^{N_\alpha} \sum_k I_{\alpha n e E} f_\alpha(E) + \sum_n^{N_{\bar{\alpha}}} \sum_k I_{\alpha \bar{\alpha} n e E} f_{\bar{\alpha}}(E) \right], \quad (5.49)$$

where each energy E depends on k .

We transform the sum over wavenumbers to an energy integral, by inserting for \hat{A} being unity in eq. (5.15). Since the lower energy cut-off in the energy bands of the leads are ϵ_n (and not zero as written in the version in eq. (5.15)), one obtains

$$\sum_{k>0} \rightarrow \frac{m}{2\pi\hbar^2} \int_{\epsilon_n}^{\infty} dE$$

in the continuum limit. Spin degrees of freedom are still part of the reflection and transmission matrices (and is, in other words, incorporated into the number of channels N_α), and are not summed over explicitly in eq. (5.49).

Assume the leads and the scattering region all have the same, uniform chemical potential μ , and imagine introducing applied voltages, V_α , in each lead separately. These voltages shift changes the chemical potential of the leads to a new value

$$\mu_\alpha = \mu - eV_\alpha.$$

we choose the chemical potential to coincide with the lower-cut-off energy ϵ_n , such that the lower limit of the energy integral becomes zero. At this point, the sums over n in eq. (5.49) can be moved inside the energy integral. Inserting for the local and nonlocal currents in eqs. (5.46) and (5.47) into the total electronic current in eq. (5.49), therefore yields

$$I_{e,\alpha}(V_\alpha, V_{\bar{\alpha}}) = \frac{-e}{h} \int_0^\infty dE f(E - \mu + eV_\alpha) [N_\alpha - (R_\alpha^e(E) - A_\alpha^e(E))] - f(E - \mu + eV_{\bar{\alpha}}) [T_{\alpha\bar{\alpha}}^e(E) - A_{\alpha\bar{\alpha}}^e(E)]. \quad (5.50)$$

The energy E should be measured relative to the lower cut-off energy of the lead energy bands. When we calculate differential conductances in chapter 8, we employ a

different notion for the energy-dependence for the scattering probabilities. We assume the band-width of the leads is much larger than the energy-window

$$\mu - \text{a few } k_B T < \omega < \mu + \text{a few } k_B T$$

for which transport is important. The energy-dependence of the transmission and reflection probabilities is different at the bottom of a lead, compared to in the middle of a lead (where the band is approximately linear in the wave-vector k). Therefore, whenever we refer to the probabilities as functions of ω in the future, we implicitly refer to this second picture (being in the middle of the band). Since the energy-window for transport does not have a lower band in this picture, we integrate ω from $-\infty$ to ∞ , and the only states that contribute to transport lie in the range $\tilde{f}_\alpha(\omega) = f(\omega + eV_\alpha) - f(\omega)$.

Part II

Numerical Background

Chapter 6

Tight-binding models and using *Kwant*

6.1 Tight-binding models

A tight binding model is a Hamiltonian that has a set of discrete degrees of freedom $\{i\}$ and $\{j\}$, such that it can be decomposed as

$$H = \sum_{ij} t_{ij} |i\rangle \langle j|. \quad (6.1)$$

$|i\rangle$ corresponds to the degrees of freedom and may usually be written as $|i\rangle = |\mathbf{r}\alpha\rangle$ where \mathbf{r} is the spatial coordinate of an artificial lattice site and α corresponds to the internal degree of freedom of the site, such as spin and particle-hole degrees of freedom. In other words, the Hamiltonian coupling sites \mathbf{r} and \mathbf{r}' can be written as

$$H_{\mathbf{r}\mathbf{r}'} = \sum_{\alpha\alpha'} H_{\mathbf{r}\alpha\mathbf{r}'\alpha'} |\mathbf{r}\alpha\rangle \langle \mathbf{r}'\alpha'|. \quad (6.2)$$

This form arises naturally when discretizing a continuum Hamiltonian, which will be illustrated in section 6.1.3. Section 6.1.1 serves the purpose of introducing the intuition behind approximating continuum Hamiltonians with a tight-binding Hamiltonian, and is largely based on [26, sec. 4.3].

6.1.1 Nearest-neighbor approximation

Consider a translationally invariant Hamiltonian obeying the symmetry

$$[H, \tau(a)] = 0, \quad (6.3)$$

where $\tau(a)|x\rangle = |x+a\rangle$, $\tau(a)$ being the translation operator. Consider, for example, an electron moving in a one-dimensional (1D) chain of positive ions equally spaced with a lattice spacing of a . The system Hamiltonian may be modeled as a periodic potential with periodicity a , in addition to the kinetic energy of the electron, $\hbar^2 k^2/2m_e$, where $\hbar k$ is its momentum and m_e is the electron mass. Define a general translation operator $\tau(l)$ as

$$\tau(l)|x\rangle = |x+l\rangle. \quad (6.4)$$

where l is an arbitrary length for which the spatial coordinate x is translated. The kinetic energy is independent of the position and is thus translationally invariant, whilst the potential energy the electron experiences in the vicinity of a positive ion is invariant if and only if $l = a$.

If the potential barriers at the lattice sites is made to go to infinity, as illustrated in figure 6.1, the ground state of the system is one where the electron is completely

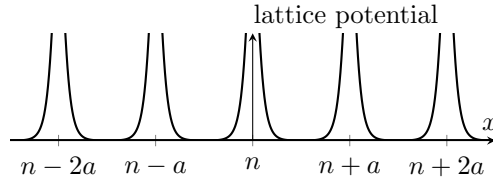


Figure 6.1: With a lattice potential going to infinity at every site, the particles are completely localized. Hence, the tight-binding approximation $\langle n'|H|n\rangle = \delta_{n',n}$ describes the system perfectly, because there is no finite overlap between sites.

localized at the n 'th lattice site, and $H|n\rangle = E_0|n\rangle$, where $|n\rangle$ is the corresponding eigenstate and E_0 is its eigenenergy. Since the system is translationally invariant, the energy E_0 is the same for any n going from $-\infty$ to $+\infty$. In other words, the ground-state energy of this system is infinite-fold degenerate.

Note that $|n\rangle$ is not an eigenstate of the translation operator because $\tau(a)|n\rangle = |n+1\rangle$ shifts the electron to the neighboring lattice site. However, the linear combination

$$|ka\rangle \equiv \sum_{n=-\infty}^{\infty} e^{inka} |n\rangle \quad (6.5)$$

is a simultaneous eigenket of not only H , but also $\tau(a)$, as one is free to absorb the extra index in $|n+1\rangle$ by re-defining the summing index¹.

¹When performing calculations with discretized Hamiltonians, one may employ an equivalent notation in terms of creation and annihilation operators specified in discrete real and momentum space. In that case, the basic tight-binding Hamiltonian can be written as $H^{tb} = \sum_{i,j} t_{ij} c_i^\dagger c_j$, c_i^\dagger creating a particle with the degree of freedom(s) given by j (such as position, and spin σ). For

Letting the potential barriers decrease to a finite value, as illustrated in figure 6.2, the localized ket $|n\rangle$ can still be constructed, and will still obey $\tau(a)|n\rangle = |n+1\rangle$.

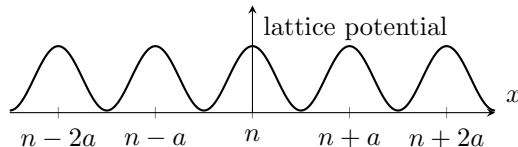


Figure 6.2: With a finite lattice potential, the tight-binding approximation to the m 'th nearest neighbor is imperfect, because the ground state wavefunction at one site leaks into neighboring sites.

Also, the diagonal elements of the Hamiltonian $\langle n|H|n\rangle = E_0$ is still independent of which lattice site is considered. However, the wavefunction $\langle x|n\rangle$ will have a finite tail leaking into other sites, whence the off-diagonal elements of H , $\langle n'|H|n\rangle \neq 0$ if $n' \neq n$, become finite.

Assuming the potential barriers are sufficiently high, the overlap between more distant neighbors can be considered to be negligible. For example, a "nearest neighbor" approximation

$$\langle n'|H|n\rangle \begin{cases} \neq 0 & \text{if } n' = n, n \pm 1 \\ = 0 & \text{elsewhere} \end{cases} \quad (6.6)$$

means all other off-diagonal elements, corresponding to second, third (and so on) nearest neighbors is assumed to be zero. Importantly, this lifts the energy degeneracy between sites. Let the onsite and the nearest neighbor hopping terms be given by

example, if a spin-full Hamiltonian is initially given in position (\mathbf{r}_j) space, the momentum (\mathbf{k}) representation can be written as $H^{tb} = \sum_{\mathbf{k}\sigma,\mathbf{k}'\sigma'} \epsilon_{\mathbf{k}}^{tb} c_{\mathbf{k}\sigma}^\dagger c_{\mathbf{k}'\sigma'}$, by inserting for the discrete Fourier transforms

$$c_j^\dagger = \frac{1}{\sqrt{N}} \sum_{\mathbf{k}} e^{i\mathbf{k}\cdot\mathbf{r}_j} c_{\mathbf{k}}^\dagger$$

and its hermitian conjugate. This formalism yields equivalent results to those obtained in this section, and is a useful tool. In the free particle case, for instance, one obtains

$$t_{ij} = \frac{1}{N} \sum_{\mathbf{k}} \frac{\hbar^2 k^2}{2m} e^{i\mathbf{k}\cdot(\mathbf{r}_i - \mathbf{r}_j)}$$

where N is the number of available \mathbf{k} states, and the excitation $c_{\mathbf{r}_i,\sigma}^\dagger c_{\mathbf{r}_j,\sigma}$ moves the fermion from \mathbf{r}_j to \mathbf{r}_i while conserving spin. This function exponentially decays when \mathbf{r}_j is further away from \mathbf{r}_i . Therefore, cutting off this exponential tail for the m 'th nearest neighbor can be a reasonable approximation.

Kronecker delta functions

$$\begin{aligned}\langle n' | H | n \rangle &= E_0 \delta_{n',n} \\ \langle n' | H | n \rangle &= -t \delta_{n \pm 1, n}.\end{aligned}$$

(The so-called graph of this tight-binding model is given in figure 6.4a in section 6.1.2.) Then $|ka\rangle$ is the energy eigenstate of H , measuring an energy

$$\begin{aligned}E(k) &= \langle ka | H | ka \rangle \\ &= \sum_{n', n=-\infty}^{\infty} e^{-in'ka} e^{inka} \langle n' | H | n \rangle \\ &= \sum_{n=-\infty}^{\infty} (\langle n | H | n \rangle + e^{-ika} \langle n+1 | H | n \rangle + e^{ika} \langle n-1 | H | n \rangle) \\ &= E_0 - 2t \cos(ka),\end{aligned}\tag{6.7}$$

having inserted for the definition of the eigenstate in eq. (6.5). The third equality, the nearest-neighbor tight-binding approximation in eq. (6.6) is imposed, such that only the onsite and nearest-neighbor terms are left after summing over n' . The free

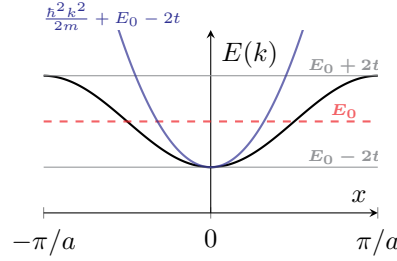


Figure 6.3: Energy dispersion (blue) and the tight-binding approximation to nearest neighbors (black) in the first Brillouin zone.

Hamiltonian thus approximates to the tight-binding Hamiltonian

$$H = \sum_{k\sigma, k'\sigma'} \frac{\hbar^2 k^2}{2m} c_{k\sigma}^\dagger c_{k'\sigma'} \approx \sum_{k,\sigma} (E_0 - 2t \cos(ka)) c_{k\sigma}^\dagger c_{k\sigma}\tag{6.8}$$

in this momentum-space representation, where $c_{k\sigma}^\dagger$ creates an electron with momentum k and spin σ . The spin serves as the internal degree of freedom at each artificial lattice site. The energy dispersion is drawn in figure 6.3 and assumes energies in the range $E(k) \in [E_0 - 2t, E_0 + 2t]$. The approximation is good for small k , as is indicated from comparing to the $\hbar^2 k^2 / 2m + \{\text{potential energy}\}$ curve (blue).

6.1.2 Tight-binding Hamiltonians mapped onto a graph

We have seen that if a Hamiltonian is translationally invariant, we can define a simultaneous eigenket, as in eq. (6.5), for both the Hamiltonian and the translational operator. We did assume a translational operator on a form that only takes us between discrete sites. As a result, we can view the model as a *mapping of the Hamiltonian onto a graph*. For instance, the graph of the translationally invariant Hamiltonian considered in the last section is shown in figure 6.4a. Another example of a graph is shown in figure 6.4b, which has nodes corresponding to each site, and lines between

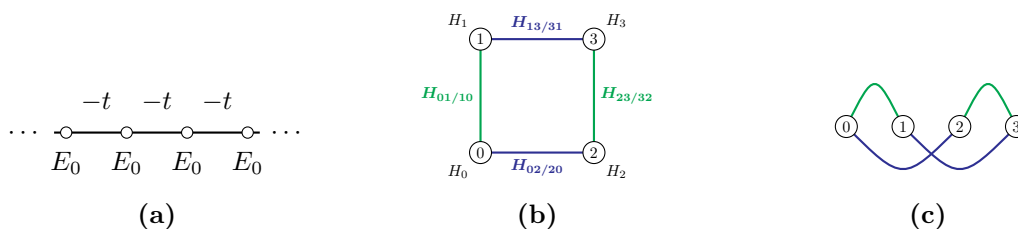


Figure 6.4: (a) Graph of the graph of the onsite and hopping terms in the nearest-neighbor tight-binding approximation given in (6.7). (b) A two-dimensional tight-binding model. Blue/green lines are nearest-neighbor hoppings H_{ij} in the x- and y-directions, respectively. Black dots signify lattice sites $i = 0, 1, 2, 3$, defining the onsite terms H_i . (c) the deformed version of (b) is equivalent, as long as the hoppings couple the same sites. This illustrates that the graph does not specify the dimensionality of the system, only inter-site hoppings.

nodes which correspond to hermitian off-diagonal elements of the Hamiltonian. This particular Hamiltonian can be represented as the matrix

$$\begin{pmatrix} H_0 & H_{01} & H_{02} & 0 \\ H_{10} & H_1 & 0 & H_{13} \\ H_{20} & 0 & H_2 & H_{23} \\ 0 & H_{31} & H_{32} & H_3 \end{pmatrix} \quad (6.9)$$

Naturally, the onsite (diagonal) terms require only one coordinate to be specified, while the 'hoppings' are specified by two sites.

A graph lives in lattice space, which does not have to be equivalent to real space. Note how we have not specified how the sites (1 through 4) are positioned in real space in the graph in figure 6.4b. For all we know, the artificial lattice sites in this graph could be positioned in one-dimensional real space. Deforming this graph by forcing the four sites to be on a straight line in one dimension, as shown in figure 6.4c, the system would now also have next nearest-neighbor hoppings $H_{13/31}$ and $H_{02/20}$. In other words, the graph just shows how different discrete sites, with some degrees of freedom, are related to each other. It does not show what real-space dimension the system lives in.

6.1.3 Discretizing the Hamiltonian using finite differences

While knowing what the tight-binding approximation is and what it looks like as graphs in site-space is important, it is practical to use the method of finite differences to describe real-space continuum Hamiltonians. The resultant matrix Hamiltonian in the fictitious lattice space can for example be represented in a computer memory. In doing so, it enables us to perform simulations with these Hamiltonians. We start with the kinetic part of the simple one-dimensional (1D) kinetic Hamiltonian already considered ($\hbar^2 k^2/2m$), and then move on to a more complicated Hamiltonian (see eq. (7.1)).

Discretizing a 1D kinetic Hamiltonian

Consider the continuum Hamiltonian

$$H_{1D,kin} = -\frac{\hbar^2}{2m^*} \frac{d^2}{dx^2} \quad (6.10)$$

where x is the spatial coordinate, \hbar is the reduced Planck's constant and m^* the effective mass of the particle. When the Hamiltonian acts on the eigenstate $\psi(x)$ in the time-independent Schrödinger equation, the differential operator operates on the eigenstate. To first order in neighbor hoppings, the differential operator can in general be approximated as

$$\begin{aligned} \frac{d\psi(x_n)}{dx} &\approx \frac{\psi(x_{n+1}) - \psi(x_{n-1}))}{2a}, \\ \frac{d^2\psi(x_n)}{dx^2} &\approx \frac{\psi(x_{n+1}) + \psi(x_{n-1}) - 2\psi(x_n)}{a^2}, \end{aligned} \quad (6.11)$$

where $x_n = na$ denotes the position of the n 'th artificial lattice site of our now discretized system, where a is the artificial lattice spacing. Hence, the Schrödinger equation reads

$$H_{1D,kin} \psi(x_n) = \frac{\hbar^2}{2m^*a^2} (2\psi(x_n) - \psi(x_{n+1}) - \psi(x_{n-1})) = E\psi(x_n). \quad (6.12)$$

We note that the coefficient $t = \frac{\hbar^2}{2m^*a^2}$ has the unit of energy. Alternatively, we may write the Hamiltonian in first quantization as

$$H_{1D,kin} = (2t|x_n\rangle - t(|x_{n+1}\rangle + |x_{n-1}\rangle))\langle x_n|. \quad (6.13)$$

Acting on the state $|x_n\rangle$, the state can either stay at its current position and have an onsite energy $2t$, or hop to its nearest neighbors with a hopping potential $-t$.

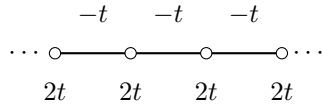


Figure 6.5: Graph of the 1D kinetic tight-binding Hamiltonian in equation (6.13).

In the current 1D case, the graph would look as in figure 6.5. The onsite energies are different from in figure 6.4, where the onsite potential energy is also included in the value E_0 , in addition to the kinetic onsite energy $2t$. For higher dimensions,

- the hopping energy is always $-t$ for each real space dimension, while
- the onsite energy is $d \cdot 2t$ in d dimensional real space.

6.2 Scattering theory in *Kwant*

Kwant is a software-package that allows for constructing tight-binding models, adding leads, and thereafter solving for the S-matrix. A strength of using the software package *Kwant*[27], is the ease of attaching leads to the central scattering region. Although the scattering region implemented in *Kwant* is finite, infinite leads may be implemented by imposing translational symmetry. In this section, we outline how the S-matrix is obtained with *Kwant*.

Start by considering attaching a single lead to the scattering region. Take the basis sorted according to the reverse distance from the scattering region, such that the unit cells of the lead furthest away from the scattering region come first (upper left) in the Hamiltonian

$$H = \begin{pmatrix} \ddots & V_L & & & \\ V_L^\dagger & H_L & V_L & & \\ & V_L^\dagger & H_L & V_{LS} & \\ & & V_{LS}^\dagger & H_S & \end{pmatrix}, \quad (6.14)$$

while the closest unit cell and then the scattering region are last (lower right). H_S is the Hamiltonian of the scattering region, H_L the unit cell Hamiltonian of the lead, V_L the coupling between the unit cells within the lead, and V_{LS} that between the lead and the system. Typically, the unit cell of the lead is much smaller than the total scattering region. This full, tri-diagonal Hamiltonian can account for a situation where more than one lead is attached.

Define the wavefunction of the system and lead as

$$(\dots, \psi^L(i), \dots, \psi^L(2), \psi^L(1), \psi^S), \quad (6.15)$$

where the wavefunction of the scattering region is ψ_S and the i 'th unit cell of the lead is $\psi^L(i)$. Due to the translational invariance of the leads, the states residing in the leads are in general a superposition of plane waves. With the leads attached, the total system, including the leads, is semi-infinite.

Let $\tau(a)$ be the translation operator that translates a state at site j by the lattice constant a , such that $\tau(a)|j\rangle = |j+a\rangle$. As seen in section 6.1.1, there exists a simultaneous eigenket of the Hamiltonian and the translation operator. In the context of *Kwant*, we denote these eigenkets by

$$\phi_n(j) = (\lambda_n)^j \chi_n, \quad (6.16)$$

with χ_n the eigenvector of the n 'th mode. Applying the translation operator, one may easily verify that this is an eigenstate² with eigenvalue λ_n . The reason for this notation is partially the fact that, contrary to before where the whole system was translationally invariant, evanescent modes may also solve the Schrödinger equation

$$\left(H_L + V_L \lambda_n^{-1} + V_L^\dagger \lambda_n \right) \chi_n = E \chi_n \quad (6.17)$$

for the system, which is a combination of translationally invariant leads and an arbitrary scattering region. In general, the absolute square of all probability amplitudes $|\lambda_n|$ sum to 1. Thus, the normalization condition is $|\lambda_n| \leq 1$, regardless of the nature of the mode, or

$$|\lambda_n| \begin{cases} < 1 & \text{if evanescent} \\ = |e^{ik_n}| & \text{if propagating,} \end{cases}$$

where k_n is the longitudinal momentum of the n 'th mode. The evanescent mode can never account for the total probability for the n 'th mode. According to the Ehrenfest theorem, the expectation value of the particle current is

$$\langle I \rangle \equiv 2 \operatorname{Im} \langle \phi_n(j) | V_L | \phi_n(j-1) \rangle = \pm 1. \quad (6.18)$$

Every propagating mode in the leads are normalized such that one unit of particle current can move in the positive (+1) or the negative (-1) current direction.

The scattering states in the leads can be written as a linear combination of the incoming mode ϕ_n^{in} , for which $\langle I \rangle = +1$ (the positive current direction is here defined as into the scattering region), the outgoing modes ϕ_n^{out} , with $\langle I \rangle = -1$, and the evanescent modes as follows:

$$\psi_n(i) = \phi_n^{in}(i) + \sum_m S_{mn} \phi_m^{out}(i) + \sum_p \tilde{S}_{pn} \phi_p^{ev}(i). \quad (6.19)$$

² $\tau(a) \phi_n(j) = (\lambda_n)^{j+1} \chi_n = \lambda_n \phi_n(j)$.

S_{nm} is the scattering matrix from the incoming mode n to the propagating mode m , and \tilde{S}_{pn} that where the incoming mode scatters into an evanescent mode p . The wavefunction inside the scattering region is

$$\psi_n(0) = \phi_n^S \quad (6.20)$$

because the 0'th unit cell of any lead is taken to be the actual scattering region, while cells 1 and upwards are inside the lead. Note that the sum over modes m does not distinguish between leads: having one or five leads does not change the form of the scattering state as it is given in eq. (6.19).

Kwant matches the wavefunctions of the leads with those inside the scattering region in order to obtain two main outputs, namely the scattering matrix S_{mn} and the wavefunction in the scattering region, ϕ_n^S . This amounts to solving the tight-binding equations $H\psi_n = E\psi_n$ with the tight-binding Hamiltonian in eq. (6.14), using the Dirichlet conditions at the boundaries.

6.3 Program flow using *Kwant*

An example of how to use *Kwant* in broader strokes, is illustrated by the program flow diagram in figure 6.6. On the left (red boxes) are important inputs to the functions being called in the pseudo-code (middle boxes). In particular, the `par` dictionary is preferably constructed as a `SimpleNamespace` *python class*³ in order for the `sys.hamiltonian_submatrix` and `kwant.smatrix` to execute correctly. If we want to look at the scattering matrix elements for electrons and holes separately, it is necessary to set `norbs` when defining the lattice *Builder object* `lat`. In constructing leads, one specifies the symmetries of the lead Hamiltonian. Translational symmetry is used to repeat the unit cell of the lead an arbitrary number of times, thus the leads can be thought of as being infinitely long. After finalizing the system, the system graph can no longer be changed. At this point, we may access and for instance diagonalize the Hamiltonian of the closed system. `H.tocsc()` returns the matrix in *Compressed Sparse Column format* from the *SciPy* package (see for instance *SciPy v.1.1.0*), which can speed up computations. The high performance of the *Kwant* library is largely because the properties of sparse linear equations[28] is utilized in the *MUMPS* library, throughout the solvers in *Kwant*. The command

$$\text{smatrix.transmission}((\alpha, \tau_1), (\beta, \tau_2)) \quad (6.21)$$

returns the scattering amplitude of an electron or hole ($\tau_1 = 1$ or 0 , respectively) in lead α , which reflects or transmits to lead β as an electron or hole ($\tau_2 = 1$ or 0). See the *Kwant 1.4.1* documentation for more details about the objects used in *Kwant*.

³See for instance the *Python 3.6.9* documentation.

On the right (white boxes) in the diagram are some examples of outputs generated by code similar to the pseudo-code. From the top to the bottom are four plots of: a closed system (blue sites with lines in between), a system with infinite leads (red sites and hoppings) attached, the energy as a function of a parallel applied magnetic field in one-dimensional Majorana wire, and the differential conductance of an NS -junction with a potential barrier at the NS interface (see chapter 3.2 on BTK theory and the theoretically predicted dI/dV curves for different barriers in figure 3.9). The Majorana wire is constructed from 70 sites, while the NS system is a wire consisting of 10 sites and a potential barrier at the 4th site⁴. The barrier strengths Z (see eq. (3.21)) are 0, 0.5, 1.5, and 5 here.

⁴The code generating these two plots are adapted versions of the example in [27, app. D.6] (the Majorana wire) and section 2.6 of the *Kwant v1.4.1* documentation (the NS wire). The particular scripts used here, as well as all model parameters, are given in [3].

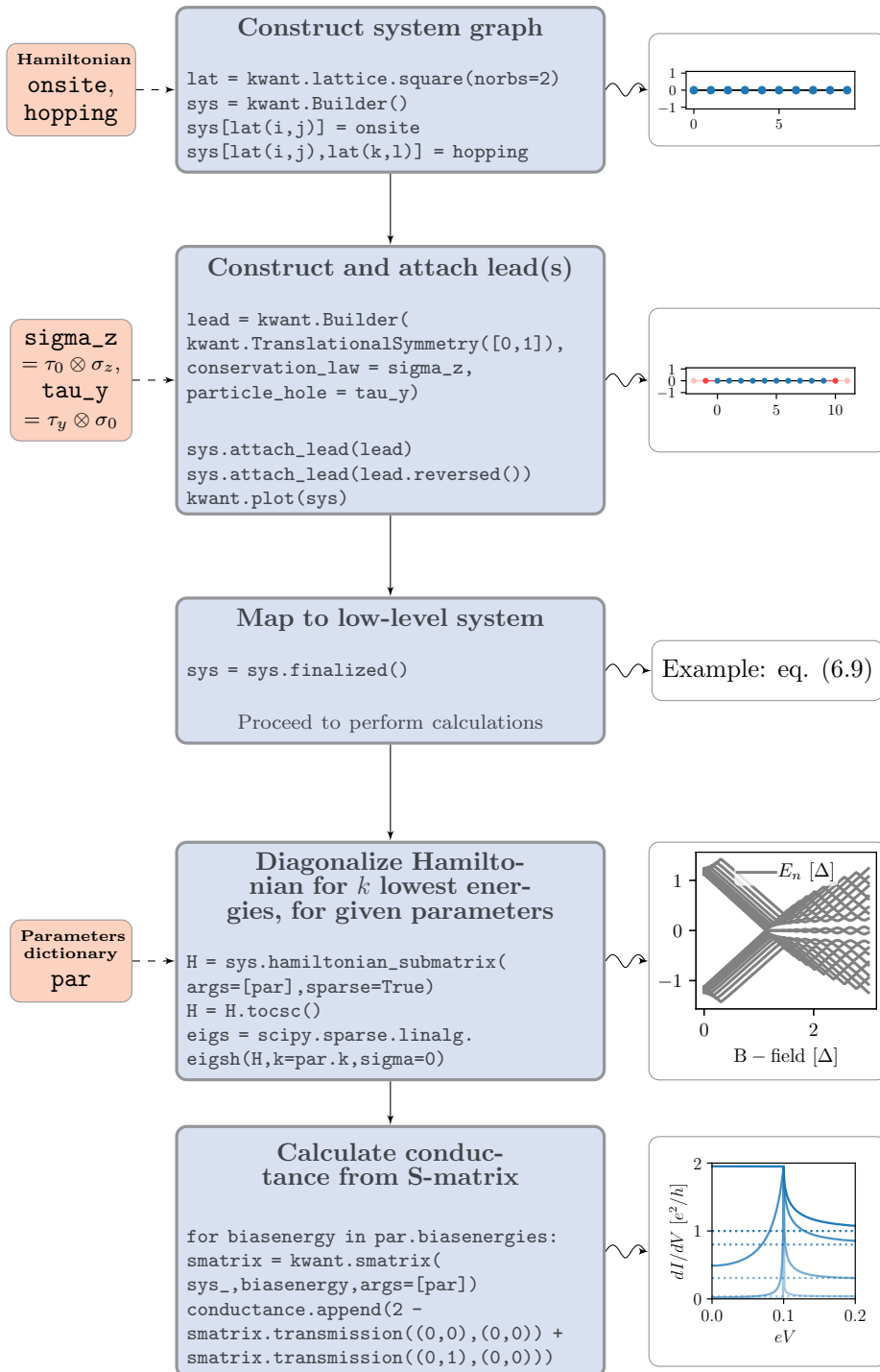


Figure 6.6: Standard program flow with pseudo-code examples using *Kwant 1.4.1*. See the main text for details.

Chapter 7

Case study: Diagonalizing a 2D hybrid system using *Kwant*

Our main goal in this chapter, is to test whether one may accurately construct and diagonalize a low-level system representation of a more complicated superconductor-semiconductor hybrid system, by using *Kwant*. To this end, we consider a closed hybrid system, consisting of three regions, as depicted in figure 7.1. This particular

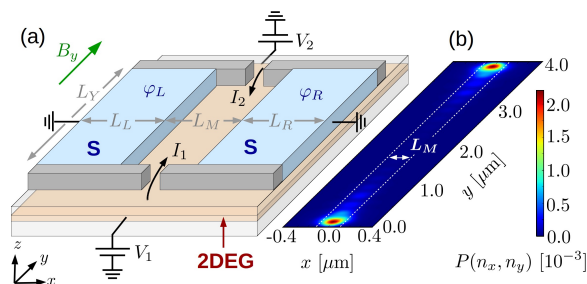


Figure 7.1: (a) The two-dimensional electron gas (2DEG) system with superconducting layers on the left and right sides, as shown. The external magnetic field is parallel to the central strip. Voltages and currents on each side are shown. (b) End states form in the strip ($P(n_x, x_y)$ is the probability density of the bound state wavefunction). Source: [7, fig. 1].

system was proposed in [7] as a platform for constructing networks of more than one Majorana qubit.

Here, we consider particular system parameters, similarly to what the authors used in [7]. The system has a spatially varying effective superconducting gap $\Gamma(x)$, which is finite and real inside the regions of the two-dimensional semiconductor (2DEG) positioned under the superconducting slabs. These superconducting regions are defined by $|y| \leq L_Y/2$ and $-(L_L + L_M/2) \leq x \leq (L_R + L_M/2)$. We assume these are

the only regions in the 2DEG subject to proximity-induced superconductivity. The two-dimensional Oreg-Lutchyn Hamiltonian is constructed as follows[7]:

$$H_{eff} = \left[-\frac{\hbar^2}{2m^*} (\partial_x^2 + \partial_y^2) - \mu \right] \tau_z - i\alpha_R (\sigma_x \partial_y - \sigma_y \partial_x) \tau_z + E_Z \sigma_y / 2 + \Gamma(x) \tau_x \quad (7.1)$$

and acts on the Nambu spinor $\Psi = (\psi_{e,\uparrow}, \psi_{e,\downarrow}, \psi_{h,\downarrow}, -\psi_{h,\uparrow})^T$. $\Gamma(x)$ is the proximity-induced effective gap, which we assume to have a superconducting phase of $\phi(x) = 0$ for all x . Both $\Gamma(x)$ and $\phi(x)$ are taken to be constants as a function of y . The 2DEG is specified with an effective mass m^* and the chemical potential μ . α_R is the Rashba spin-orbit strength, E_Z the Zeeman energy, and σ_{x_i} and τ_{x_i} are the Pauli matrices in spin and electron-hole space, respectively ($x_i = x, y, z$). The aspect ratio is assumed to be large ($L_Y \gg L_M$), implying that the central region is quasi one-dimensional. In turn, the topological states it may host are end states.

The tight-binding model for the Oreg-Lutchyn Hamiltonian is obtained by discretizing the continuous coordinates (x, y) into (x_n, y_m) , where $n \in [1, N_x]$ and $m \in [1, N_y]$ for a lattice with N_x lattice points in the x -direction and N_y in the y -direction. Similarly to the kinetic Hamiltonian seen previously, H_{eff} is split into onsite and hopping energies, where the hoppings are directionally dependent, as indicated in figure 7.2a. In obtaining the tight-binding model, we discretize the total system in a rectangular lattice, whose lattice constant in the x - and y -direction are a_x and a_y , respectively, where $a_{x_i} = L_{x_i}/N_{x_i}$. Inserting for the finite differences given in eq.

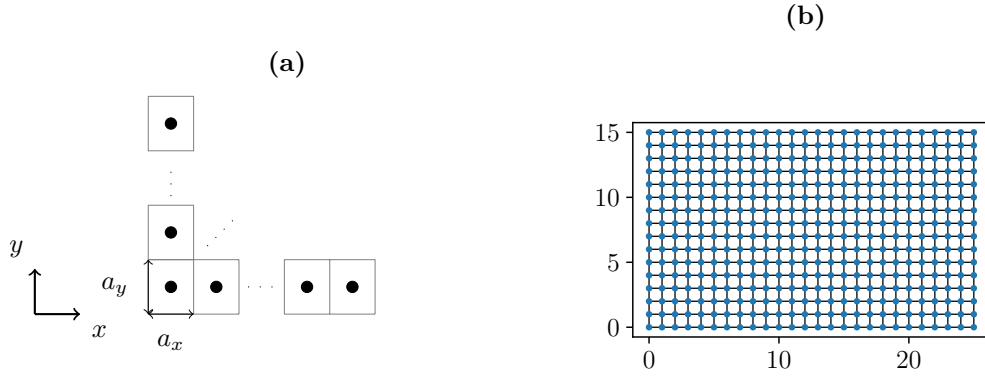


Figure 7.2: (a) Lattice sites (black dots) and lattice constants a_{x_i} , defined on a two-dimensional lattice. We center the lattice sites in the middle of each primitive cell. (b) Graph of the tight-binding Hamiltonian in eqs. (7.3) (black dots), (7.4) (horizontal lines), and (7.5) (vertical lines). The number of sites displayed here ($N_x = 26$ and $N_y = 16$) is 1/10 smaller than what is actually used in the simulation, for cosmetic reasons.

(6.11), the discrete Hamiltonian becomes

$$\begin{aligned}
H_{eff}^{t-b} &= H_{onsite} |n_x n_y \sigma \tau\rangle \langle n_x n_y \sigma \tau| \\
&+ H_{hopx} |n_{x+1} n_y \sigma \tau\rangle \langle n_x n_y \sigma \tau| + h.c. \\
&+ H_{hopty} |n_x n_{y+1} \sigma \tau\rangle \langle n_x n_y \sigma \tau| + h.c.
\end{aligned} \tag{7.2}$$

in second quantization, with every site having an internal spin (σ) and electron-hole (τ) degree of freedom. Explicitly, the different terms are

$$H_{onsite} = [2(t_x + t_y) - \mu] \tau_z + E_z \sigma_y / 2 + \Gamma(x) \tau_x \tag{7.3}$$

$$H_{hopx} = \left(-t_x + \left(\frac{i\alpha_R \hbar}{2a_x} \sigma_y + h.c. \right) \right) \tau_z \tag{7.4}$$

$$H_{hopty} = \left(-t_y + \left(-\frac{i\alpha_R \hbar}{2a_y} \sigma_x + h.c. \right) \right) \tau_z \tag{7.5}$$

$$t_{x_i} \equiv \frac{\hbar^2}{2m^* a_{x_i}^2}, \quad x_i = x, y. \tag{7.6}$$

We construct a low-level system with the onsite and hopping potentials in eqs. (7.3) through (7.5) in *Kwant* (see the program flow in figure 6.6). A scaled down version of the system graph shown in figure 7.2b. The gap inside the left and right regions are $\Gamma_{Left} = \Gamma_{Right} = 180 \mu eV$, while the phase $\phi_{Left} = \phi_{Right}$ are taken to be zero. The Rashba spin-orbit strength is $\alpha_R = 1.42 \times 10^{-4} c$, the effective single-particle mass is $m^* = 0.023 m_e$, and the chemical potential is parked at $\mu = 0$. The system dimensions are $L_{Left} = L_{Right} = 1 \mu m$ and $L_M = 250 nm$ in the x -direction, and $L_y = 4 \mu m$ along the y -direction. $N_x = 260$ sites and $N_y = 160$ sites. The lattice spacings are $a_x = 8.7 nm$ and $a_y = 25 nm$.

The resulting energy spectra from diagonalizing this tight-binding Hamiltonian, using *Kwant* and *numpy*, do reproduce that obtained in [7]. By increasing the applied magnetic field along the y -direction, the energy spectrum for the lowest 50 eigenstates are as shown in figures 7.3a. With the increasing magnetic field, the energy gap closes and a near zero-energy mode emerges at the energy $E_{Z,critical} \sim 120 \mu eV$.

Next, the authors of [7] perform the same calculation, but with a gate where the rightmost proximitized region used to be. This is modeled with $L_R = 0$. The symmetric device belongs to the symmetry class *BDI*. Removing the right superconducting region breaks inversion symmetry along the x -axis, which brings the system into class *D* [23]. Using *Kwant*, the resultant dispersion versus field is shown in figure 7.3b. Even though the antisymmetric device belongs to a different symmetry class, the topological region starts at a similar value $E_{Z,critical} \sim 100 \mu eV$. The authors note that the effective gap is significantly smaller than Γ for both devices. In the chapter

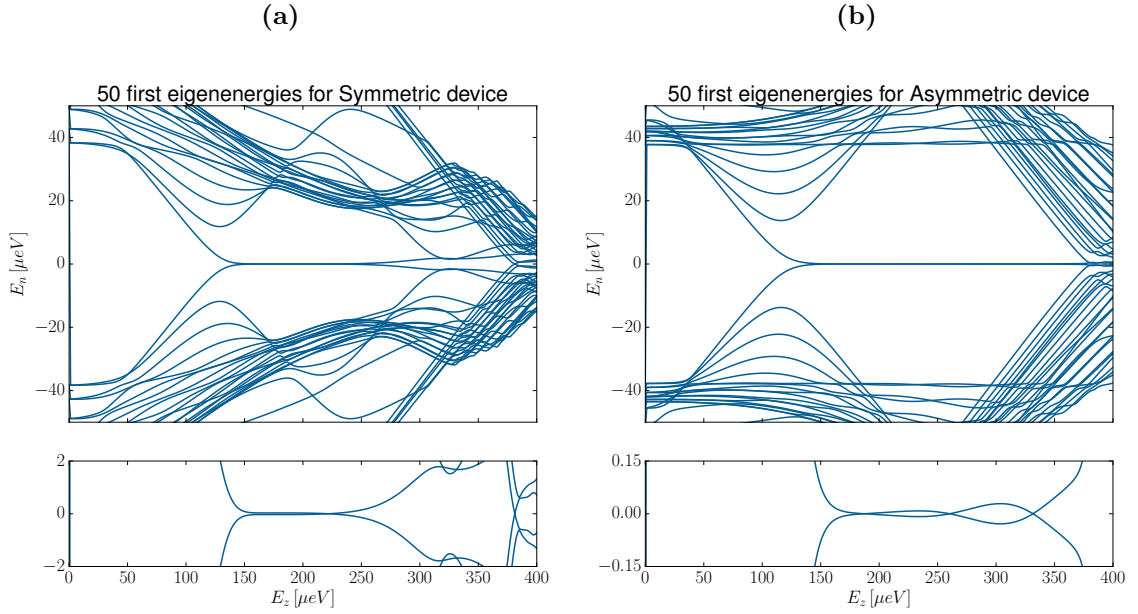


Figure 7.3: Energy spectra of (a) symmetric and (b) asymmetric devices. The topological phase transition occurs when the gap closes. The lower panels are close-ups of the upper panels. The gapped states have energies oscillating close to zero energy.

on the normal-superconductor proximity effect, we assume that every site in the semiconductor is tunnel coupled to the superconductor. Andreev bound states (ABS) only experience a pairing potential with a superconductor, for sites being tunnel coupled to the superconductors. The only sites where ABS experience a pairing potential, are those which are nearest neighbors to the superconductor sites. Since the system is quasi one-dimensional, not every site in the central strip is actually coupled to the superconducting regions. Therefore, the induced gap is smaller than what is expected for a device where all ABS are influenced by a pairing potential. The finite geometry of the sample is also what gives rise to the difference in $E_{Z,critical}$, from what one would expect for an infinite, one-dimensional Oreg-Lutchyn Hamiltonian (see chapter 4.3.3).

Any small discrepancies between figure 7.3 and the spectrum obtained in [7, fig. 2] should be numerical errors, either from a slightly different discretization choice (for instance defining each site as being on the edge of the primitive cells depicted in figure 7.2a, such that $a_{x_i} = L_{x_i}/(N_{x_i} - 1)$), or from the numerical diagonalization routine used (here, `scipy.sparse.linalg.eigsh`, see the *scipy v1.3.0* documentation).

While there is much more physics that can be explored for this system, such as conductance simulations or how changing different parameters in the system can

enhance the effective topological gap, we learned from the perspective of performing simulations using *Kwant* that

We can reproduce the emergence of a near zero-energy modes with a graph that has both superconducting and semiconducting regions arranged in two dimensions.

We note that the finite-size effect is important: the gapped energies oscillate and are non-zero for the majority of the domain for the field (see the lower panels in figure 7.3). This effect is governed by the system length, and not the inter-site spacing or number of lattice sites. (The latter only affects the boundary conditions and the tight-binding approximation.) In other words, choosing a_x and a_y slightly differently from what is implemented here, while keeping the number of lattice points constant, can significantly affect the overlap between end states, because the system length changes. As long as the number of sites is large enough that the boundary conditions do not change more than the energy scale of the features of interest (for instance the oscillatory behavior of the near-zero energy mode), the influence of changing the tight-binding approximation, is much smaller than the effect from slightly altering the system length. The finite-size effect is significant for all near-Majorana systems simulated throughout this thesis.

Part III

Results

Chapter 8

Nonlocal conductance spectroscopy of Andreev bound states

This chapter is divided into three main parts. The first describes the theoretical machinery going into analysing the differential conductance from the scattering matrix of the hybrid system depicted in figure 8.1 for energies below the induced superconducting gap. Afterwards, the focus shifts over to numerical conductance calculations and what information can be extracted from the near-zero energy conductance peaks. The third part evaluates in more detail to what degree the delocalization of the system state is encoded in the discrepancy between local and integrated quantities. The work in this chapter has been done in collaboration with the authors of [15]. My contribution to this article was mainly the numerical simulations. I also checked the analytical results done by the other authors.

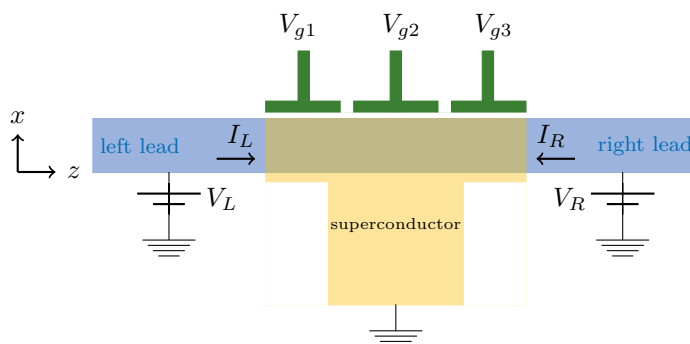


Figure 8.1: Example set-up of a hybrid device consisting of a semiconducting wire (blue) in proximity to a grounded superconductor (yellow). Local gates (green) can be used to introduce local potentials. Bias voltages V_L and V_R may be applied to the left and right leads, and I_L and I_R are the respective bias-dependent currents measured in the leads.

In experiments, local gates at the ends of the proximitized region (pinchers) are used to create a local potential barrier, while a gate along most of the central region (plunger) may be used to shift the chemical potential of the proximitized region.

8.1 Scattering and conductance

8.1.1 Scattering matrix

In the system depicted in figure 8.1, electrons and holes in the left (L) and right (R) normal metal leads are incident at the normal-superconductor (NS) junction. These single particles may reflect off the boundary at either ends, or transmit through to the opposite lead. For energies below the superconducting gap, $\omega < \Delta$, only Cooper pairs can carry current through the superconducting scattering region, and therefore the device has two terminals in terms of single particle current for these energies.

The S-matrix contains the reflection and transmission (scattering) amplitudes of single particle states incident on the superconducting scattering region. Below the gap, the S-matrix may be expressed as a 2×2 block matrix

$$\mathbf{S}(\omega) = \begin{pmatrix} \mathbf{r}_L(\omega) & \mathbf{t}_{LR}(\omega) \\ \mathbf{t}_{RL}(\omega) & \mathbf{r}_R(\omega) \end{pmatrix} \quad (8.1)$$

in lead space, which was discussed in detail in chapter 5. Each block \mathbf{r}_α ($\mathbf{t}_{\bar{\alpha}\alpha}$) has dimension $N_\alpha \times N_\alpha$ ($N_{\bar{\alpha}\alpha}$), where N_α is the number of channels in lead α (including spins). From tracing over the diagonal blocks from the unitarity relations of the scattering matrix, we found the relations

$$R_\alpha^e(\omega) + A_\alpha^e(\omega) + T_{\bar{\alpha}\alpha}^e(\omega) + A_{\bar{\alpha}\alpha}^e(\omega) = N_\alpha \quad (8.2)$$

$$R_\alpha^e(\omega) + A_\alpha^h(\omega) + T_{\bar{\alpha}\alpha}^e(\omega) + A_{\bar{\alpha}\alpha}^h(\omega) = N_\alpha \quad (8.3)$$

These probability current conservation laws (see figure 5.4), as well as particle-hole symmetry, are used later to demonstrate a symmetry between the antisymmetric components of local and nonlocal differential conductances which may be measured in this device.

8.1.2 Weidenmüller formula for the S-matrix

The proximitized wire in figure 8.1 is described by the Hamiltonian

$$H = H_S + H_{leads} + H_T \quad (8.4)$$

where H_S is the system Hamiltonian, H_{leads} that of the metallic leads and H_T is the tunneling matrix. The latter is given in terms of electron creation operators Ψ_σ^\dagger in the system, and c_{ka}^\dagger of the leads

$$H_T = \sum_{ka} t_a (\Psi^\dagger(x_a) c_{ka} + h.c.) \quad (8.5)$$

where a is the channels of the leads (which is different from the lead index α), x_a is the position of the channel in the system, and t_a is the tunneling amplitude between electrons in the lead and the system channel a . We may re-write the creation and annihilation operators as a linear combination

$$\Psi^\dagger(x_a) = \sum_n (\gamma_n^\dagger u_n(x_a) + \gamma_n v_n(x_a)) \quad (8.6)$$

in terms of the Bogoliubon operators γ_n (see eq. (2.15)). Respectively, the u_n and v_n factors are electron and hole probability amplitudes for a given quantum number n . Inserting for eq. (8.6) into eq. (8.5), we can re-write the tunneling Hamiltonian as

$$H_T = \frac{1}{2} \sum_{kna} (\gamma_n^\dagger \ \gamma_n) \mathbf{W}_{na} \begin{pmatrix} c_{ka} \\ c_{ka}^\dagger \end{pmatrix} + h.c., \quad (8.7)$$

where

$$\mathbf{W}_{n,a} = t_a \begin{pmatrix} u_n(x_a) & -v_n^*(x_a) \\ v_n(x_a) & -u_n^*(x_a) \end{pmatrix}, \quad (8.8)$$

is the coupling matrix in the channel a . The coupling matrix elements tunnel couples electrons and holes of the leads to the Bogoliubon quasiparticle excitations in the proximitized superconductor.

For wide-band leads, the density of states of the leads is approximately constant, thus the lead Hamiltonian can be linearized around the Fermi wavevector. Assuming the leads are perfectly transmitting, and the density of states in both leads are identical, the S-matrix for an incident mode with energy ω , is given by the Weidenmüller formula[29]

$$\mathbf{S}(\omega) = 1 - 2\pi i \nu \mathbf{W}^\dagger (\omega - H_{BdG} + i\pi \nu \mathbf{W} \mathbf{W}^\dagger)^{-1} \mathbf{W}. \quad (8.9)$$

The derivation of this formula is outlined in appendix D, for a general scattering region connected to an arbitrary number of perfectly transmitting leads. \mathbf{W} is the coupling matrix which parametrizes the tunnel coupling between the scattering region

and the leads as in eq. (8.8), ν is the density of states of the leads, and H_{BdG} is the BdG system Hamiltonian. $i\pi\nu\mathbf{W}\mathbf{W}^\dagger$ is the self-energy, which incorporates the renormalization in the energy of the central scattering region, due to it being proximitized by the leads[24, 29]. The form of this self-energy is analogous to the self-energy, see eq. (3.17), resulting in the normal-superconductor proximity effect. $(\omega - H_{BdG} + i\pi\nu\mathbf{W}\mathbf{W}^\dagger)^{-1}$ is thus the effective Green's function of the system being proximitized by the leads.

In the following, we make the assumption that tunneling only takes place between the leads and the end sites. The coupling matrix lives explicitly in lead \otimes electron – hole space. Therefore, every coupling to the respective lead is weighed by the electron and hole probability amplitudes as in eq. (8.8). With the given set-up, all except the leftmost and rightmost sites of the system are coupled to the leads, and thus the coupling matrix (in site-space) $\mathbf{W} = (W_{n,L} | W_{n,R})$ (see eq. (8.8)) only couples the electron and hole amplitudes at these very leftmost and rightmost sites. Assuming the number of channels $N_L = N_R = 1$ (that is, assuming only one internal degree of freedom in each site, such as spin), the total coupling matrix is

$$\mathbf{W} = \left(\begin{array}{cc|cc} t_L u_L & -t_L v_L^* & t_R u_R & -t_R v_R^* \\ t_L v_L & -t_L u_L^* & t_R v_R & -t_R u_R^* \end{array} \right) \quad (8.10)$$

where, respectively, u_α and v_α are the electron and hole amplitudes with the lead index α . We have suppressed the index n in all elements of this matrix. This form of the coupling matrix is used to determine the S-matrix for a single Andreev level in section 8.3.1.

8.1.3 Particle-hole symmetry of the S-matrix

The scattering matrix obeys particle-hole symmetry, $\mathcal{P}S(-\omega)\mathcal{P}^{-1} = S(\omega)$, where $\mathcal{P} = \tau_x \mathcal{K}$ is the particle-hole symmetry operator, τ_{x_i} ($x_i = x, y, z$) are Pauli matrices acting on electron-hole space and \mathcal{K} is the complex conjugation operator¹. The particle-hole symmetry in each block of the S-matrix,

$$\mathbf{r}_\alpha = \tau_x \mathbf{r}_\alpha^*(-\omega) \tau_x \quad \text{and} \quad \mathbf{t}_{\alpha\bar{\alpha}} = \tau_x \mathbf{t}_{\alpha\bar{\alpha}}^*(-\omega) \tau_x,$$

which explicitly reads

$$\begin{aligned} r_{ee}(\omega) &= r_{hh}^*(-\omega), & r_{eh}(\omega) &= r_{he}^*(-\omega), \\ t_{ee}(\omega) &= t_{hh}^*(-\omega), & t_{eh}(\omega) &= t_{he}^*(-\omega) \end{aligned} \quad (8.11)$$

¹This can be shown by noting $\tau_x (\mathbf{W}\mathbf{W}^\dagger)^* \tau_x = \mathbf{W}\mathbf{W}^\dagger$, $\tau_x \mathbf{W}^* \tau_x = -\mathbf{W}$ (see eq. (8.8)), and $\tau_x H_{BdG} \tau_x = -H_{BdG}$.

for the individual probability amplitudes, where the lead index has been suppressed. Inserting this in the definitions for the probabilities in terms of traces (see eq. (5.30)), one obtains

$$\begin{aligned} R_\alpha^e(\omega) &= R_\alpha^h(-\omega), \quad T_{\bar{\alpha}\alpha}^e(\omega) = T_{\bar{\alpha}\alpha}^h(-\omega) \\ A_\alpha^e(\omega) &= A_\alpha^h(-\omega), \quad A_{\bar{\alpha}\alpha}^e(\omega) = A_{\bar{\alpha}\alpha}^h(-\omega). \end{aligned} \quad (8.12)$$

This equivalent statement of particle-hole symmetry explicitly tells us that, for every electronic process at energy ω , there is a corresponding hole process at the negative energy $-\omega$ which is equally likely. Eq. (8.12) becomes key in the next section.

8.2 Differential Conductance and its Symmetries

The differential conductance is defined as

$$G_{\alpha\beta} = \frac{dI_\alpha}{dV_\beta} \quad (8.13)$$

with lead indices $\alpha, \beta \in \{L, R\}$, from which a differential conductance matrix

$$\mathbf{G} = \begin{pmatrix} G_{LL} & G_{LR} \\ G_{RL} & G_{RR} \end{pmatrix} \equiv \begin{pmatrix} \frac{dI_L}{dV_L} & \frac{dI_L}{dV_R} \\ \frac{dI_R}{dV_L} & \frac{dI_R}{dV_R} \end{pmatrix} \quad (8.14)$$

may be constructed. We assume that all scattering probabilities are independent of the bias voltages on either side of the wire. Consequently, the Fermi-Dirac distributions $\tilde{f}_\alpha(\omega) = f(\omega + eV_\alpha) - f(\omega)$ are the only voltage-dependent ingredients of the current

$$\begin{aligned} I_\alpha &= -\frac{e}{h} \int_{-\infty}^{\infty} d\omega \tilde{f}_\alpha(\omega) [N_\alpha - R_\alpha^e(\omega) + A_\alpha^e(\omega)] \\ &\quad + \frac{e}{h} \int_{-\infty}^{\infty} d\omega \tilde{f}_{\bar{\alpha}}(\omega) [T_{\alpha\bar{\alpha}}^e(\omega) - A_{\alpha\bar{\alpha}}^e(\omega)]. \end{aligned} \quad (8.15)$$

Eq. (8.15) was derived in chapter 5. The lead indices $\alpha \neq \bar{\alpha}$, while β and α are free. Performing the derivative with respect to V_α , the voltage dependence of the other lead, $V_{\bar{\alpha}}$, drops out. Thus, in general:

The conductance matrix element

$$G_{\alpha\beta} = \frac{dI_\alpha}{dV_\beta} = G_{\alpha\beta}(V_\beta)$$

is always a function of V_β .

Performing the derivative of the current in eq. (8.15) explicitly, the conductance matrix is

$$\mathbf{G} = \frac{e^2}{h} \int_{-\infty}^{\infty} d\omega \begin{pmatrix} h_L(\omega) [N_L - R_L^e(\omega) + A_L^e(\omega)] & -h_R(\omega) [T_{LR}^e(\omega) - A_{LR}^e(\omega)] \\ -h_L(\omega) [T_{RL}^e(\omega) - A_{RL}^e(\omega)] & h_R(\omega) [N_R - R_R^e(\omega) + A_R^e(\omega)] \end{pmatrix} \quad (8.16)$$

where

$$h_\alpha(\omega) = -\frac{df(\omega + eV_\alpha)}{d(\omega + eV_\alpha)}, \quad -\frac{df(\omega)}{d\omega} = \frac{1}{4k_B T \cosh^2(\omega/2k_B T)}. \quad (8.17)$$

In the zero-temperature limit, $df(\omega)/d\omega$ approaches a Dirac-delta function $\delta(\omega)$. This limit will be considered in section 8.3.1. For now, the temperature is a free parameter.

The antisymmetric part of the conductance exhibits an important symmetry, which was the first main result in the publication [15]. Define the symmetric and antisymmetric conductance as

$$G_{\alpha\beta}^{sym/asym}(\omega) \equiv \frac{G_{\alpha\beta}(\omega) \pm G_{\alpha\beta}(-\omega)}{2} \quad (8.18)$$

for a general energy ω measured relative to the chemical potential in the scattering region. Setting the left and the right bias voltages equal to one another and imposing particle-hole symmetry, it follows that the *antisymmetric local* conductance, G_{LL}^{asym} , equals the *antisymmetric nonlocal* conductance, G_{LR}^{asym} , up to a minus sign. In order to demonstrate this, consider the sum (see eq. (8.16))

$$G_{LL}(V) + G_{LR}(V) = -\frac{e}{h} \int_{-\infty}^{\infty} d\omega f'(\omega + eV) H(\omega), \quad (8.19)$$

where $H(\omega) = N_L - R_L^e(\omega) + A_L^e(\omega) - T_{LR}^e(\omega) + A_{LR}^e(\omega)$. Inserting for $N_L - R_L^e(\omega)$ as expressed from the conservation of probability current in eq. (8.3),

$$H(\omega) = A_L^e(\omega) + A_L^h(\omega) + A_{LR}^e(\omega) + A_{LR}^h(\omega)$$

becomes the sum of only Andreev reflection and CAR probabilities. Therefore, $H(\omega)$ can be viewed as a completely nonlocal quantity.

Particle-hole symmetry, expressed in terms of these Andreev reflections (see eq. (8.12)), implies that $H(\omega)$ is an even function of ω . Also noting that $f'(\omega)$ is even

(see eq. (8.17)), we can see that the integral in eq. (8.19) is also even in V :

$$\begin{aligned}
G_{LL}(-V) + G_{LR}(-V) &= -\frac{e}{h} \int_{-\infty}^{\infty} d\omega f'(\omega - eV) H(\omega) \\
&= \frac{e}{h} \int_{\infty}^{-\infty} d\omega' f'(-\omega' - eV) H(-\omega') \\
&= -\frac{e}{h} \int_{-\infty}^{\infty} d\omega' f'(\omega' + eV) H(\omega') \\
&\equiv G_{LL}(V) + G_{LR}(V).
\end{aligned}$$

In the second and third equalities, the substitution $\omega = -\omega'$ is made, and the fact that $f'(\omega)$ and $H(\omega)$ are even functions is employed. The same holds interchanging the left and right indices. Thus, the total conductance

$$G_{\alpha\alpha}(V) + G_{\alpha\bar{\alpha}}(V) \quad \text{is even in } V, \quad (8.20)$$

which is equivalent to

$$G_{\alpha\alpha}^{asym}(V) = -G_{\alpha\bar{\alpha}}^{asym}(V), \quad \alpha \neq \bar{\alpha} \quad (8.21)$$

(which can be seen by subtracting $-G_{LL}(V) - G_{LR}(-V)$ from both sides of eq. (8.20)). This is what we wanted to show, and is our first key result in this chapter. Note that this is only possible because we have a two-terminal set-up: with a single lead, we cannot define a nonlocal conductance, per construction.

We stress that the symmetry eq. (8.21) only holds in the case $V_L = V_R = V$. We made the important assumption throughout that, the scattering probabilities are independent of the bias energy V , which is valid if the system is truly non-interacting. Therefore, any measured deviation from the symmetry in eq. (8.21), in for example experiment, must be due to interaction effects.

In the next section, we show that for a single Andreev level, the symmetric and antisymmetric nonlocal conductances have a specific dependence on the charge that is probed at the ends of the wire.

8.3 Probing charge by explicit calculation of conductance

8.3.1 Single Andreev level

In order to more easily understand the physical properties of the system, while being able to calculate the conductance analytically, we choose to model a simple central

region that only has a single Andreev level coupled to the leads. We construct the Hamiltonian in its diagonal basis,

$$H_{BdG} = \begin{pmatrix} E_0 & 0 \\ 0 & -E_0 \end{pmatrix} \quad (8.22)$$

and thus the energy E_0 of the Andreev level is taken to be a known parameter. Inserting for the Hamiltonian (eq. (8.22)) and the coupling matrix (in eq. (8.10)) into eq. (8.9), we may completely determine the S-matrix for this simple model, at a given temperature.

Inserting for eqs. (8.22) and (8.10) into the effective Green's function in (8.9), we obtain

$$\begin{aligned} & [\mathcal{G}_{\text{eff}}^0(\omega)]^{-1} \stackrel{\text{def.}}{=} [\omega - H_{BdG} + i\pi\nu \mathbf{W} \mathbf{W}^\dagger]^{-1} \\ &= \frac{1}{\det(\mathcal{G}_{\text{eff}}^0(\omega))} \begin{bmatrix} \omega + E_0 + i\gamma & -2\pi i\nu (|t_L|^2 u_L v_L^* + |t_R|^2 u_R v_R^*) \\ -2\pi i\nu (|t_L|^2 u_L^* v_L + |t_R|^2 u_R^* v_R) & \omega - E_0 + i\gamma \end{bmatrix} \end{aligned} \quad (8.23)$$

with $\gamma_\alpha = \pi\nu |t_\alpha|^2 n_\alpha$ (see below) and $\gamma = \gamma_L + \gamma_R$, and where we have used that the inverse of a two-by-two matrix

$$A = \begin{pmatrix} a & b \\ c & d \end{pmatrix} \quad \text{is given by} \quad A^{-1} = \frac{1}{\det(A)} \begin{pmatrix} d & -b \\ -c & a \end{pmatrix},$$

where a through d are numbers. The determinant is²

$$\det(\mathcal{G}_{\text{eff}}^0(\omega)) = (\omega + i\gamma)^2 - E_0^2 + \gamma_L^2 + \gamma_R^2 - \xi^2 + 8\text{Re}[\xi_{LR}^2] \quad (8.24)$$

We have introduced the weights $n_\alpha = |u_\alpha|^2 + |v_\alpha|^2$ and charges $q_\alpha = |u_\alpha|^2 - |v_\alpha|^2$ at either end of the wire. Respectively, $\gamma_\alpha = \pi\nu |t_\alpha|^2 n_\alpha$ and $\xi_\alpha = \pi\nu |t_\alpha|^2 q_\alpha$ parametrize the coupling of these weights and charges to the leads. The quantities $\gamma = \gamma_L + \gamma_R$, $\xi^2 = \xi_L^2 + \xi_R^2$, and $\xi_{LR}^2 = \pi^2 \nu^2 |t_L t_R|^2 u_L u_R^* v_L^* v_R$ are also defined for ease of notation. Temperature is only accounted for once we integrate the Fermi function over energies ω in the current (see eq. (8.15)).

²Simply consider the matrix:

$$\mathcal{G}_{\text{eff}}^0(\omega) = \begin{pmatrix} \omega - E_0 + i\gamma & 2\pi i\nu (|t_L|^2 u_L v_L^* + |t_R|^2 u_R v_R^*) \\ 2\pi i\nu (|t_L|^2 u_L^* v_L + |t_R|^2 u_R^* v_R) & \omega + E_0 + i\gamma \end{pmatrix}$$

Zero temperature

For zero temperature, the derivative of the shifted Fermi-Dirac function appearing in the conductance in eq. (8.16) is approximated by a Dirac-delta function, $h_\alpha^0(\omega) = \delta(\omega + eV_\alpha)$, yielding the dimensionless conductance matrix $\mathbf{g}^{T=0}$:

$$\mathbf{g}^0 = \begin{pmatrix} N_L - R_L^e(-eV_L) + A_L^e(-eV_L) & -[T_{LR}^e(-eV_R) - A_{LR}^e(-eV_R)] \\ -[T_{RL}^e(-eV_L) - A_{RL}^e(-eV_L)] & N_R - R_R^e(-eV_R) + A_R^e(-eV_R) \end{pmatrix}. \quad (8.25)$$

Algebraically, it is a great deal of work to obtain the explicit form for the scattering matrix and hence the conductance matrix in eq. (8.25), even in this simple model. One needs to multiply the Green's function (see eq. (8.23)) by the coupling matrix as in eq. (8.9), and then calculate the absolute square of each term in the S-matrix with itself, yielding the probability amplitudes defined in eq. (5.30).

Instead of doing the whole calculation by hand, a *Mathematica* script (see [3]) may be used instead. In the script, the probability amplitudes are obtained from constructing the scattering matrix eqs. (8.9) in lead \otimes electron – hole space. These are inserted in the differential conductance matrix in eq. (8.25)³. Evaluating the same expressions, but substituting for $\omega \rightarrow -\omega$, one can use eq. (8.18) to find the symmetric and antisymmetric components of these local $g_{\alpha\alpha}^0$ and nonlocal $g_{\alpha\alpha}^0$ conductances. Simplifying the expressions with the *Mathematica* function `FullSimplify` finally yields:

$$g_{LR}^{0,sym}(\omega) = -4\xi_L\xi_R \frac{E_0^2 + \xi^2 - 8Re\{\xi_{LR}^2\} + 2\gamma_L\gamma_R + \omega^2}{(E_0^2 + \xi^2 - 8Re\{\xi_{LR}^2\} + 2\gamma_L\gamma_R - \omega^2)^2 + 4\gamma^2\omega^2} \quad (8.26)$$

$$g_{LR}^{0,asym}(\omega) = -4\xi_L\omega \frac{2E_0\gamma_R + 8Im\{\xi_{LR}^2\}}{(E_0^2 + \xi^2 - 8Re\{\xi_{LR}^2\} + 2\gamma_L\gamma_R - \omega^2)^2 + 4\gamma^2\omega^2} \quad (8.27)$$

$$g_{LL}^{0,sym}(\omega) = -\frac{\gamma_L\gamma_R - 4Re[\xi_{LR}^2]}{\xi_L\xi_R} g_{LR}^{0,sym}(\omega) + 8\omega^2 \frac{\gamma_L^2 - \xi_L^2 + 4Re[\xi_{LR}^2]}{(E_0^2 + \xi^2 - 8Re[\xi_{LR}^2] + 2\gamma_L\gamma_R - \omega^2)^2 + 4\gamma^2\omega^2} \quad (8.28)$$

$$g_{LL}^{0,asym}(\omega) = -g_{LR}^{0,asym} \quad (8.29)$$

³In defining the complex numbers $\{u_\alpha, v_\alpha\}$, we make sure to explicitly define one variable for the amplitude, and another for the complex phase. In this way, the *Mathematica* algorithms can more easily make useful simplifications of the expressions, such as trigonometric identities and canceling of terms.

8.3.2 Differential conductance spectroscopy

We are interested in probing the properties of the single Andreev bound state with energy E_0 . Thus, we now consider the case where the energy is close to resonance, $\omega \approx E_0$. With this assumption, the squared bracket in $1/|\det(\mathcal{G}_{\text{eff}}^0)|^2$ from eq. (8.23) can be Taylor-expanded to zeroth order in $\delta = E_0^2 - \omega^2$ around zero. That is, $(\delta + \text{constant})^2 \approx \delta^2 + \mathcal{O}(\delta + \text{constant})$, such that $1/|\det(\mathcal{G}_{\text{eff}}^0)|^2$ is

$$\frac{1}{\left([E_0^2 - \omega^2] + \underbrace{\xi^2 - 8\text{Re}\{\xi_{LR}^2\} + 2\gamma_L\gamma_R}_{\text{constant}} \right)^2 + 4\gamma^2\omega^2} \approx \frac{8E_0^2}{(E_0^2 - \omega^2)^2 + 4\gamma^2E_0^2} \equiv L^0(\omega) \quad (\omega \approx E_0). \quad (8.30)$$

The line function $L^0(\omega)$ describes the shape of the conductance peaks as a function of ω for a given set of parameters. $L^0(\omega)$ is symmetric in ω and is peaked around $\pm E_0$, where it has a peak value $2/\gamma^2$. Hence⁴, its full width at half maximum (FWHM) is approximately 2γ .

For small level broadenings ($E_0 \gg \pi\nu|t_\alpha|^2$), the line-function approximates to

$$L^0(\omega) \approx \frac{2\pi}{\gamma\delta(E_0 - |\omega|)}. \quad (8.31)$$

With this approximation, the differential conductances (eqs. (8.26) through (8.29)), are

$$g_{LR}^{0,\text{sym}}(\omega) \approx -\xi_L\xi_R L^0(\omega) \quad (8.32)$$

$$g_{LR}^{0,\text{asym}}(\omega) \approx -\xi_L\gamma_R L^0(\omega)\text{sign}(\omega) \quad (8.33)$$

$$g_{LL}^{0,\text{sym}}(\omega) \approx [\gamma_L\gamma_R + \gamma_L^2 - \xi^2] L^0(\omega) \quad (8.34)$$

$$g_{LL}^{0,\text{asym}}(\omega) \approx \xi_L\gamma_R L^0(\omega)\text{sign}(\omega). \quad (8.35)$$

Finite temperature

In fact, the common denominator $1/|\det(\mathcal{G}_{\text{eff}}^0)|^2$ can always be factorized in front of the conductance matrix, *for any temperature*, because it arises from taking the absolute square of the elements of the scattering matrix (eq. (8.9)). This scattering matrix

⁴ $FWHM(L^0(\omega)) = |\pm(\omega_1 - \omega_2)|$, where $\omega_{1/2} = \sqrt{E_0}\sqrt{E_0 \pm 2\gamma}$ are the values that positive ω takes at the points where $L^0(\omega)$ is at half its maximum value. Taylor-expanding in small γ , $\omega_{1/2} \approx E_0 \pm \gamma$.

contains the inverse of $\mathcal{G}_{\text{eff}}^0(\omega)$, given by eq. (8.23), for which $1/\det(\mathcal{G}_{\text{eff}}^0)$ is clearly factorized outside the whole expression.

At finite temperature, the conductance matrix in eq. (8.16) can be expressed in terms of the zero-temperature conductance matrix elements from eq. (8.25) as

$$\mathbf{g}(V_L, V_R) = \int_{-\infty}^{\infty} d\omega \begin{pmatrix} h_L(\omega) g_{LL}^0(\omega) & -h_R(\omega) g_{LR}^0(\omega) \\ -h_L(\omega) g_{LR}^0(\omega) & h_R(\omega) g_{RR}^0(\omega) \end{pmatrix}$$

The finite temperature conductance matrix is also multiplied by the line-function in eq. (8.30). The finite-temperature result is then obtained by convoluting the line-function by the function $h_\alpha(\omega)$ (see eq. (8.17))

$$\frac{d\tilde{f}_\alpha(\omega)}{dV_\beta} = \frac{df(\omega + eV_\beta)}{dV_\beta},$$

where β is the second index in $g_{\alpha\beta}^0$. Thus, the energy integral of eq. (8.31) is

$$\begin{aligned} L(V_\beta, T) &= \frac{1}{e} \int_{-\infty}^{\infty} d\omega \frac{df(\omega + eV_\beta)}{d(\omega + eV_\beta)} \frac{d(\omega + eV_\beta)}{dV_\beta} \times \frac{2\pi}{\gamma} \delta(E_0 - |\omega|) \\ &= \frac{\pi}{2k_B T \gamma} \int_{-\infty}^{\infty} d\omega \operatorname{sech}^2 \left(\frac{\omega + eV_\beta}{2k_B T} \right) \delta(E_0 - |\omega|) \\ &= \frac{\pi}{2k_B T \gamma} \operatorname{sech}^2 \left(\frac{\pm E_0 + eV_\beta}{2k_B T} \right), \end{aligned}$$

or equivalently, one may re-write the bias at the arbitrary lead β as ω , and write $L(\omega, T) = \frac{\pi}{2k_B T \gamma} \operatorname{sech}^2 \left(\frac{E_0 - |\omega|}{2k_B T} \right)$. In other words, having a finite temperature re-shapes the zero-temperature conductance in the same way for all energies $E_0(\lambda)$, even though the independent variable λ , which in some manner parameterizes the energy, may vary.

Importantly, the nonlocal symmetric conductance is proportional to the charge coupling at both leads, while the antisymmetric component is only proportional to that of the left lead. The relations also hold interchanging L and R . *Therefore, in this approximation, the local charge q_α scaled by n_α at either end of the wire, (Q_α) , can be probed by measuring the nonlocal symmetric and antisymmetric conductances and taking their ratio*

$$Q_\alpha = \frac{g_{\bar{\alpha}\alpha}^{0,\text{sym}}(E_0)}{g_{\bar{\alpha}\alpha}^{0,\text{asym}}(E_0)} \operatorname{sign}(E_0) = \frac{q_\alpha}{n_\alpha}. \quad (8.36)$$

This is another key result. In section 8.4, we demonstrate this relation and when it is valid with a numerical simulation for a one-dimensional Oreg-Lutchyn tight-binding model.

8.3.3 1D Oreg-Lutchyn model: Eigenenergy dependencies

The Oreg-Lutchyn Hamiltonian in one dimension

$$H = \left(-\frac{\hbar^2 \partial_z^2}{2m^*} - \mu - i\alpha_R \partial_z \sigma_y \right) \tau_z + \Delta \tau_x + V_Z \sigma_z \quad (8.37)$$

models a proximitized topological superconducting wire along the z -direction and lives in Nambu (the combined electron – hole and spin) space. The chemical potential of the wire is μ , α_R is the Rashba spin-orbit coupling strength, and $V_Z = B_Z/2$ parametrizes the Zeeman field, where $B_Z = g\mu_B B$ is the Zeeman splitting of an electron due to the applied parallel magnetic field B , and g is the gyromagnetic ratio in the wire. Δ is the induced superconducting gap, taken to be real for convenience, and σ and τ are Pauli matrices in spin and electron-hole space, respectively. If the wire is infinite, the system is in the topological phase for

$$\mu < \sqrt{V_Z^2 + \Delta^2}, \quad (8.38)$$

as discussed in chapter 4.3.3. The dispersion relation is given by eq. (4.20).

Consider again the local gates depicted in the set-up in figure 8.1. Each gate produces a local potential between points a and b along the wire. We model this potential by adding $V(z, a, b)\tau_z$ to the Hamiltonian, where $V(z, a, b) = V_{g,i}$ is constant for $z \in [a, b]$ and zero elsewhere.

Using the Hellmann-Feynman theorem $\frac{dE}{d\lambda} = \langle \frac{dH}{d\lambda} \rangle$, where $|\psi\rangle = (u_\uparrow, u_\downarrow, v_\uparrow, -v_\downarrow)^T$ is the Nambu spinor and λ is an arbitrary independent variable that parameterizes the eigenenergy E , the added gate term yields

$$\begin{aligned} \frac{dE_n}{dV_g} &= \frac{d}{dV_g} \langle \psi | V(z, a, b)\tau_z | \psi \rangle \\ &= \langle \psi | \int_a^b dz | \psi \rangle \langle \psi | \tau_z | \psi \rangle \\ &= \int_a^b dz (q_\uparrow(z) + q_\downarrow(z)), \end{aligned} \quad (8.39)$$

where the local charge at the spacial coordinate z with spin σ is $q_\sigma(z) = |u_\sigma(z)|^2 - |v_\sigma(z)|^2$. In the second equality, a resolution of identity is inserted and the derivative has been performed. We stress that

The energy dependence on the gate voltage is given by the *integrated* charge between points a and b and is therefore not a local quantity.

If the gate voltage is constant and along the whole wire, it can be mapped to the chemical potential of the wire up to a sign: In the Hamiltonian, μ couples to $-\tau_z$, while the gate potential is coupled to τ_z , and therefore

Mapping from a constant global gate potential to μ introduces an extra sign.

This is useful to note because μ will be an independent variable in the numerical simulations.

We are also interested in the energy dependence on the Zeeman field. Using the same ingredients as above, one obtains

$$\frac{dE_n}{dV_Z} = \int dz (q_{\uparrow}(z) - q_{\downarrow}(z)). \quad (8.40)$$

We emphasize that

The energy dependence on Zeeman field is given by the *integrated* spin polarization.

For strong fields, the topological phase is in an almost fully spin-polarized regime⁵. With higher spin polarization, one would expect the energy dependence in eq. (8.40) to be governed by the integrated *charge* $-\int dz q_{\downarrow}(z)$. When this is indeed the case, there is effectively also an extra minus sign to account for if we try to relate dE_n/dV_Z and the charge of the ground state.

Any deviation between the integrated charge in eq. and the actual, local end charges q_{α} *in this model* (obtained from diagonalizing the Hamiltonian in eq. (8.37)) is affected by two factors: (i) the degree of spin-polarization in the ground state, and (ii) the degree of which the integrated and actual local charges q_{α} differ, due to the end state not being completely localized at the edge sites α . On the other hand, when the independent variable is the global gate voltage, that is, μ in the Hamiltonian, the deviation can only be attributed to (ii) (delocalization, because the chemical potential couples directly to the integrated charge in eq. (8.39), and not to spin polarization). These findings, from applying the Hellmann-Feynman theorem to the Hamiltonian with added gate potentials that couple equally to electrons and holes, are used to aid in interpreting the numerical results in section 8.4.

⁵If the system is perfectly spin polarized, the model can be mapped onto the Kitaev chain. This is a way one can argue that the Oreg-Lutchyn model describes a topological system for the appropriate choice of spin-orbit coupling and (strong) applied field in a superconducting wire (see chapter 4.3.3).

8.4 Numerical Results

8.4.1 Construction of the S-matrix

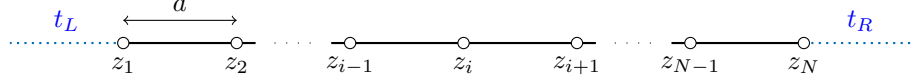


Figure 8.2: Discretization of the one-dimensional Hamiltonian into hopping (solid black lines) and onsite (circles) terms, depicted in real space. Each onsite term sits on a site at the z -coordinate z_i , where $i = 1, 2, \dots, N$. The inter-site distance is a . Normal leads are attached at the left and right end sites. The coupling to the leads is modeled by the hoppings t_α (blue dotted lines).

In performing the numerical simulations, the coupling matrix and the Hamiltonian are discretized for every fictitious site. The inter-site hopping is approximated as nearest-neighbor, yielding the tight-binding version of the Oreg-Lutchyn Hamiltonian

$$H_{\text{num}} = \sum_{i=1}^N H_{\text{onsite}} |z_i \sigma \tau\rangle \langle z_i \sigma \tau| + \{H_{\text{hop}} |z_{i+1} \sigma \tau\rangle \langle z_i \sigma \tau| + h.c.\} \quad (8.41)$$

where

$$H_{\text{onsite}} = (2t - \mu) \tau_z + V_Z \sigma_z + \Delta \tau_x \quad (8.42)$$

$$H_{\text{hop}} = \left(-t + \left\{ \frac{i\alpha_R}{2a} \sigma_y + h.c. \right\} \right) \tau_z. \quad (8.43)$$

If the total number of sites is N and the length of the wire is L , the inter-site distance is $a = L/N$. The kinetic hopping amplitude is $t \equiv \hbar^2/2m^*a^2$ in electron-hole space, while the hopping contribution from the spin-orbit coupling is $t_R \equiv \alpha_R/2a$.

Like the S-matrix, the coupling matrix is a block matrix in lead space

$$\mathbf{W}_{\text{num}}^\dagger = \begin{pmatrix} \mathbf{W}_L^\dagger \\ \mathbf{W}_R^\dagger \end{pmatrix}.$$

In our model, as depicted in figure 8.2, the lead only couples to the left and right edge sites. Thus, the coupling to the leads is zero for all other sites, and we implement

$$\mathbf{W}_L^\dagger = \begin{pmatrix} \mathbf{1} & \mathbf{0} & \dots & \mathbf{0} & \mathbf{0} \end{pmatrix}$$

$$\mathbf{W}_R^\dagger = \begin{pmatrix} \mathbf{0} & \mathbf{0} & \dots & \mathbf{0} & \mathbf{1} \end{pmatrix},$$

$\underbrace{\hspace{10em}}_{N \text{ blocks}}$

where each block are specified in Nambu space and are thus 4×4 matrices. Contrary to the single Andreev level model, the energies of the system nor the diagonal basis are known by construction in the numerical model, and have to be determined by numerical diagonalization. Only after the diagonalization routine can the $\{u_\sigma(z_i), v_\sigma(z_i)\}$, $i = 1, 2, \dots, N$ factors be extracted from the eigenstates.

The weaker the tunnel couplings are to the leads, the sharper the measured conductance peaks become. In other words, one may choose the lead coupling such that the conductance peaks are more narrow than a typical energy spacing of the states one finds useful. If, on the contrary, the peak width is too large, the conductance peaks may overlap significantly, and one may lose information due to interference between peaks, or alternatively put, interference in the effective Green's function $\omega - H + i\pi\nu\mathbf{W}\mathbf{W}^\dagger$ in the S-matrix. When constructing the coupling matrix in the simulations that follow, the coupling terms are chosen as $2\pi\nu|t_L|^2 = 2\pi\nu|t_R|^2 = t/2$, such that $|t_\alpha|$ are significantly smaller than the system hopping. With this particular choice of symmetric tunnel couplings, the S-matrix (see eq. (8.9)) assumes the form

$$\mathbf{S}_{\text{num}}(\omega) = \mathbf{1} - i \frac{t}{2} \mathbf{W}_{\text{num}} \left(\omega - H_{BdG} + i \frac{t}{4} \mathbf{W}_{\text{num}} \mathbf{W}_{\text{num}}^\dagger \right)^{-1} \mathbf{W}_{\text{num}}. \quad (8.44)$$

Implementing a non-symmetric lead coupling can be done by $\mathbf{W}_\alpha \rightarrow t_\alpha \mathbf{W}_\alpha$ and specifying ν as a separate variable from t and t_α .

From $\mathbf{S}_{\text{num}}(\omega)$, we calculate the conductance as a function of μ and V_Z for a range of energies ω of incident single particles in the leads, which is given by the bias voltages applied at either side. We take the bias to be the same $V = V_L = V_R$ at each side, similarly to in section 8.2. This is done for a specific set of system parameters. As outlined in section 8.3.1, the zero-temperature conductance matrix in eq. (8.25) is calculated from accessing these probabilities in the scattering matrix $\mathbf{S}_{\text{num}}(\omega)$. The results are presented in section 8.4.2.

By diagonalizing the low-level system Hamiltonian in eq. (8.41), the Nambu spinor at site i and the eigenenergy E_n of the n 'th eigenstate

$$|\psi_i^{E_n}\rangle = (u_{i,\uparrow}^{E_n}, v_{i,\downarrow}^{E_n}, u_{i,\downarrow}^{E_n}, -v_{i,\uparrow}^{E_n})^T \quad (8.45)$$

are obtained, from which the charges and weights

$$q_i^{E_n} = \sum_\sigma |u_{i,\sigma}^{E_n}|^2 - |v_{i,\sigma}^{E_n}|^2, \quad n_i^{E_n} = \sum_\sigma |u_{i,\sigma}^{E_n}|^2 + |v_{i,\sigma}^{E_n}|^2 \quad (8.46)$$

at for instance the end sites can be calculated and compared to two key quantities: the integrated charge in eqs. (8.39) and (8.40), and to the charge probed by the nonlocal symmetric and antisymmetric conductances, using eq. (8.36).

8.4.2 Nonlocal antisymmetric differential conductance

We implement a tight-binding Hamiltonian with the Rashba-spin orbit strength $\alpha_R = 0.28 \text{ eV}\text{\AA}$, induced superconducting gap $\Delta = 180 \mu\text{eV}$, and effective mass $m^* = 0.023 m_e$, with m_e the electron mass. The wire is 1500 nm long and has $N = 800$ sites. Thus, the inter-site distance (lattice constant) is $a = 1.875 \text{ nm}$. Hence, the intersite hopping energy from the kinetic term in the Hamiltonian is $t = 471 \text{ meV}$, while $t_R = 7.5 \text{ meV}$, the hopping due to the spin-orbit term, is two orders of magnitude smaller.

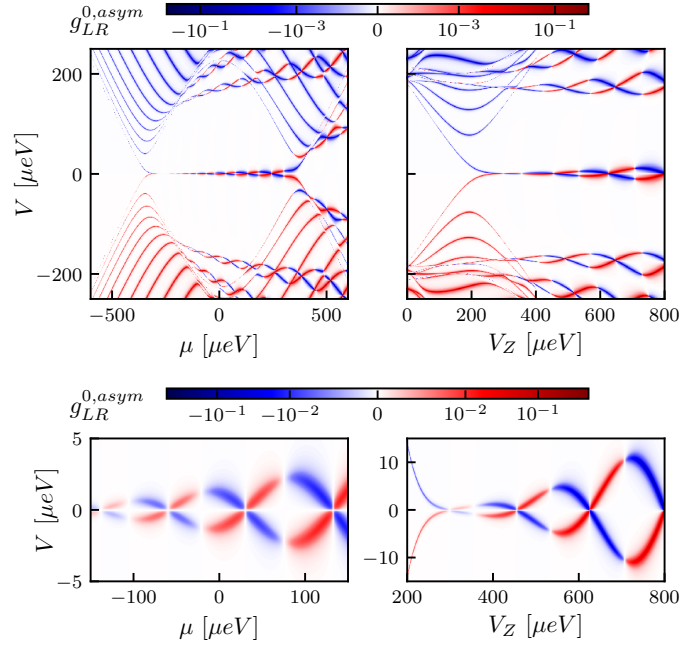


Figure 8.3: The nonlocal antisymmetric conductance plotted as a function of bias V , and chemical potential μ in (a) and (c), with $V_Z = 400 \mu\text{eV}$, and as a function of V_Z for $\mu = 0$ in (b) and (d). Panels (c) and (d) show a zoom in of the near-zero bias peaks in the conductance, for segments of the topological region.

Figure 8.3 displays the results from the simulations for both trivial and topological regions. The peaks of the nonlocal antisymmetric conductance (red and blue broadened lines) overlap with the energies found by numerical diagonalization of the tight-binding Hamiltonian. The topological phase transition takes place at $|\mu| \approx 350 \mu\text{eV}$ in (a) and $V_Z \approx 200 \mu\text{eV}$ in (b). Inside the topological region, near-zero bias peaks in the conductance emerge. These peaks oscillate around zero bias due to the finite size of the system, which renders the end state wavefunctions with a finite overlap.

The sign in the conductance changes close the maxima of the energy. This can be understood as being the manifestation of the Hellman-Feynman theorem, which can be re-stated as eqs. (8.39) and (8.40). When the derivative of the energy is zero (at the maxima and minima of the energy E_0), the integrated charge is necessarily zero, according to the theorem. Similarly, when V_Z is variable, the derivative in the energy should follow the integrated spin-polarization. In the high field limit, an increase in the spin-polarization may strengthen the correlation between dE/dV_Z and the integrated charge.

Considering figures 8.3c and (d) more closely, the sign changes in the conductance do not coincide exactly with any of the energy maxima. This 'shift' is completely attributed to the discrepancy between how we measure conductance, and what the Hellman-Feynman theorem states: conductance is only probed at the end sites, while $dE/d\lambda$ is the exact, *integrated* charge for the closed system. The nature of local and integrated quantities are discussed in section 9.2.

8.4.3 Numerical conductance spectroscopy and local BCS charge

The antisymmetric and symmetric components of the nonlocal conductance in figures 8.3c and (d), are read off along the lowest energy E_0 . This energy is calculated from diagonalizing the Hamiltonian (in eq. (8.41)), and is shown in figure 8.4a, together with the conductances. Numerically speaking, this trace along the lowest energy E_0 is given by the set of points $\{\lambda[i], V[j]\}$ in the space spanned by $\{\lambda, V\}$ in figure 8.3c and (d). The resolution is $i = 1, 2, \dots, 1000$ in the λ -direction, and $j = 1, 2, \dots, 800$ in the V -direction for this particular simulation. For every point $\lambda[i]$, the algorithm picks j such that $|V[j] - E_0[i]|$ is minimized.

The lattice spacing a has been chosen to be so short that the eigenenergies do not change significantly by decreasing the lattice constant further. Specifically, the eigenenergies changes less than the difference between the local and integrated charges, both of which are shown in figure 8.4. For our purposes, the continuous model is therefore represented accurately enough by the tight-binding Hamiltonian.

The antisymmetric component (blue line) oscillates between positive and negative values, and has two types of zeros: one where the energy crosses zero, and another when the energy is close to one of its extrema.

★ At the *eigenenergy zero crossing*, the zero in the conductance $g_{LR}^{0,asym}[i, j]$ manifests as a *dip*.

△ Near the *extremal points* of the eigenenergy, the conductance $g_{LR}^{0,asym}[i, j]$ crosses zero and the sign of the conductance changes.

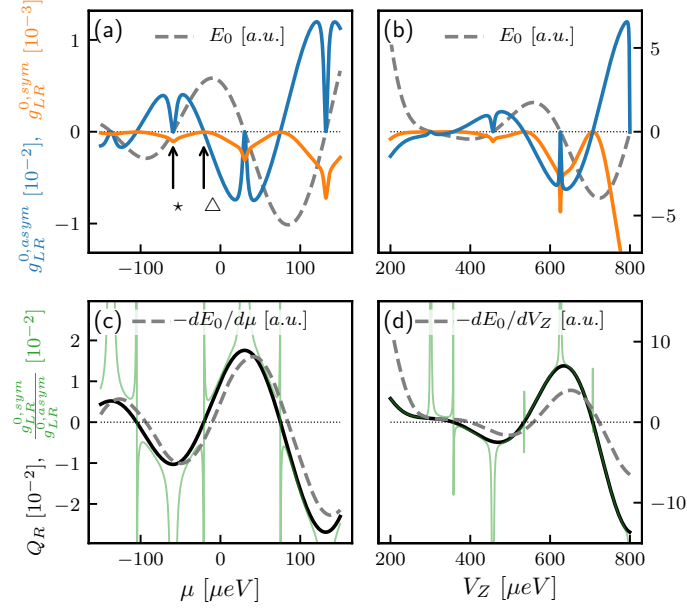


Figure 8.4: (a) and (b) show the nonlocal symmetry-decomposed differential conductances traced along the energy E_0 , in the same domains of μ and V_Z as in figures 8.3c and 8.3d. In (c) and (d), their ratio (green line) is shown, together with the exact end charge Q_R (black line) and the derivative of the energy (gray dashed line), both determined from numerically diagonalizing the effective system Hamiltonian 8.41.

Numerically, the symmetric component (orange line) only has near zeros around the energy extrema points Δ . In particular, when the tunnel coupling to the leads is not negligible, the traced symmetric component does not completely reach zero in our numerical simulations. We attribute this to small numerical inaccuracies⁶.

In figure 8.4c and (d), we probe the local charge at the right edge site, Q_R , both from estimating it using the ratio of the conductances as in (8.36) (green line), and from diagonalizing the system (black line). For significant domains in μ and V_Z , the charge is indeed probed by the nonlocal conductance, as is expected in the single Andreev bound state model (see section 8.3.1).

The charges align better the further away from the divergencies they are. For example, for the higher μ values, the effective distance *traced* in V , μ space is longer between each divergence because the amplitude of the energy oscillations increases.

⁶The resolution in the biasenergies ($3 \times 10^{-2}/800$) is finite. We can minimize $|V[j] - E_0[i]|$ and find the best j for the given resolution, but this does not mean we have the true value of the biasenergy for which the conductance is, for instance, *exactly* zero.

Therefore, charges coincide better for higher μ in this case. This is another way of saying that probing the charge using the conductances is more reliable when the energy spacing becomes larger compared to a given level broadening. The nature of the divergences is discussed further in section 9.1.

For comparison to the integrated system, the derivative of the energy is shown (gray dashed lines). Its sign roughly follows that of the charges, although it is shifted significantly to the right. One reason for this discrepancy can be interpreted as being due to the charge not being completely localized at the ends. The energy is related to the *integrated* charge, while the charge Q_R and the ratio $g_{LR}^{0,sym}[i,j]/g_{LR}^{0,asym}[i,j]$ are probed at the ends of the wire. As a result, *the shift in the energy from the charge may quantify the degree of which the near-zero mode charge is localized at the ends of the wire.*

Observe that the discrepancy between the integrated ($-dE/dV_Z$) and local (Q_R and $g_{LR}^{0,sym}/g_{LR}^{0,asym}$) quantities is larger when the magnetic field is the independent variable. In section 8.3.3, we argued that any discrepancy between the derivative of the energy and the local end charge must stem from either delocalization, or the system not being completely spin-polarized. That is, spin polarization may also contribute to the shift between $-dE/dV_Z$ and Q_R observed in figure 8.4d.

This observed shift is further discussed in light of the real-space dependence of probability density, spin polarization and charge in sections 9.2.2 through 9.2.4.

8.5 Nonlocal conductance simulations using *Kwant*

We now turn back to working with the *Kwant* package. We first build the tight-binding system, given by the onsite Hamiltonian in eq. (8.42), and the nearest-neighbor hoppings in eq. (8.42). The zero-temperature expression (see eq. (8.25)) for the local and non-local differential conductances are calculated from accessing the transmission and reflection probabilities from the S-matrix, which *Kwant* outputs for the model (see [3]). The relevant entries in the S-matrix are, for a given biasenergy and independent variable λ (these variables, indexed by i and j , respectively, are both looped over):

$$\begin{aligned}
 R_L^e[i,j] &= \text{smatrix.transmission}((0,0),(0,0)) \\
 A_L^e[i,j] &= \text{smatrix.transmission}((0,1),(0,0)) \\
 T_{LR}^e[i,j] &= \text{smatrix.transmission}((0,0),(1,0)) \\
 A_{LR}^e[i,j] &= \text{smatrix.transmission}((0,1),(1,0))
 \end{aligned}
 \tag{8.47}$$

The left (right) lead corresponds to the 0 (1) index. See figure 6.6 for a refresher on the indexing convention, and for how the electron-hole symmetry is defined for the

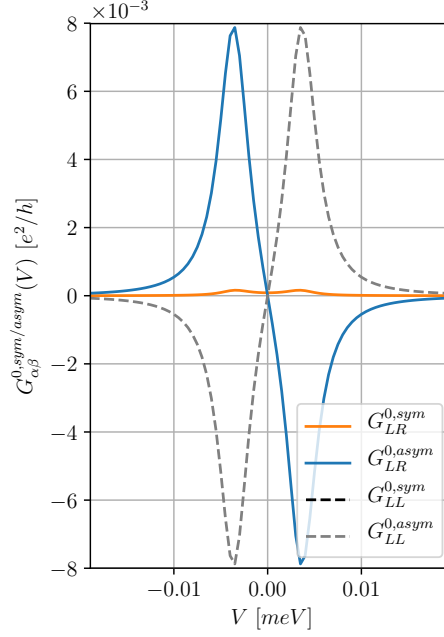


Figure 8.5: A line-cut of the in-gap conductance calculated for the same system as in the main results, but now using *Kwant*. The local, symmetric conductance, $G_{LL}^{0,sym}$, is outside the range of the values plotted on the conductance axis.

lead **Builder** objects. This symmetry is necessary to provide explicitly, in order to access the electron and hole components as done in eq. (8.47). The program flow is as outlined in chapter 6.3.

We use the same system parameters as in the earlier results, but with a much coarser discretization of 60 sites for a 1500 nm wire, thus $a = 25\text{ nm}$, and $t = 6.80\text{ meV}$. The tight-binding parameter of the leads is $t_{\text{leads}} = 1\text{ meV}$, which corresponds to a band-width of 2 meV . The pincher is implemented with $t_{\text{pincher}} = 3 t_{\text{sys}}$. We reproduce the symmetry relation $G_{LR}^{0,asym}(V) = -G_{LL}^{0,asym}(V)$, for a line-cut at $\mu = 0.2\text{ meV}$. The different components are shown in figure 8.5. Whether the differential conductances are being accurately represented for energies above the gap, and to what degree the tight-binding Hamiltonian represents the continuous model, are different questions. The fact still stands: the symmetry between the local and nonlocal antisymmetric conductance is, per construction, a mathematical property of any non-interacting scattering region with a lead geometry that supports non-local measurement.

Chapter 9

Discussions and Conclusions

9.1 Divergent peaks in the ratio $g_{LR}^{0,sym} / g_{LR}^{0,asym}$

From figure 8.4, we saw that the value $g_{LR}^{0,sym}[i, j] / g_{LR}^{0,asym}[i, j]$ diverges near the zero-energy crossings (at points Δ), and near the energy maxima (at points \star). Decreasing the tunnel coupling further, the traced symmetric component more strongly approaches zero at the zero-energy crossings. As a result, the divergent peaks become more narrow. The width of these peaks can, in principle, be made arbitrarily narrow, by decreasing the tunnel coupling to the leads. One may have to adjust the resolution in λ and the biasenergy to see the peaks if they become very narrow.

We note that, when computing the fraction $g_{LR}^{0,sym}[i, j] / g_{LR}^{0,asym}[i, j]$ around the points Δ , it diverges towards positive or negative values, depending on which side this point is approached from. Whether the sign is positive or negative on either side of points Δ , is determined by $\text{sign}(g_{LR}^{0,asym}[i, j] \times g_{LR}^{0,sym}[i, j])$, where the symmetric component always has the same sign when traced along E_0 .

Around the energy zero crossings at points \star , where the symmetric component is finite, the fraction also diverges. At these points, the two lowest energy states given by $\pm E_0(\lambda)$ cross. The conductances $g_{LR}^{0,asym}$ as a function of $E_0(\lambda) \rightarrow 0$, and $g_{LR}^{0,asym}$ of $-E_0(\lambda) \rightarrow 0$, destructively interfere at the points \star . In fact, this destructive interference must be a feature in the effective Green's function $\mathcal{G}_{\text{eff}}^0(\omega)$.

From the Hellmann-Feynman theorem, we expect the charge to be maximal when the derivative $dE/d\lambda$ has a local maximum or minimum (at points \star). However, this theorem can only be applied to a single eigenstate with energy $\pm E_0(\lambda)$. Therefore, any interference effect in the differential conductance is unaccounted for by this theorem. In addition, the points \star coincide with regions where the energy spacing $\sim 2E_0$ is not much larger than the broadening of the conductance peaks. Due to both these factors, the ratio $g_{LR}^{0,sym}[i, j] / g_{LR}^{0,asym}[i, j]$ does not actually probe the charge given by

eq. (8.36), close to the points \star .

The lowest two eigenenergy solutions are inherent physical properties of the closed system. While divergences at points Δ are a consequence of how we choose to probe the system, the divergence at the zero energy-crossings cannot be removed by letting the tunnel coupling to the leads approach zero.

9.2 Real space considerations

In figure 8.4, we have already seen that there is a discrepancy between the integrated charges ($dE/d\lambda$, for $\lambda = \mu, V_Z$) and local end charges (the exact charge $Q_R = Q_L$ and the fraction $g_{LR}^{0,\text{sym}}(\lambda)/g_{LR}^{0,\text{asym}}(\lambda)$ probing it). When the discrepancy is significant, the bound state must have non-zero weights away from the ends of the wire: if it did not, there is no way in which the integrated charge could be different from the end charges, because there would be no charges to integrate over away from the ends. Had the two charge signals been completely aligned, we cannot tell conclusively that the wavefunction is localized at the ends. A state with significant weight away from the ends of the wire may also produce a charge profile in real space that, when integrated over, yields exactly the same charge as the end charges.

In this section, we seek to quantify the degree of localization of the actual wavefunction and charge profiles in real space, so that we can compare it to the shift between $dE/d\lambda$. We additionally compute the spin polarization in real space, to see whether this polarization may have influenced the integrated charge when $\lambda = V_Z$ (see figure 8.4d). In broader terms, the aim of this investigation is also to demonstrate in more detail the nature these two quantitative measures.

9.2.1 A function quantifying the localization of a signal

Consider a one-dimensional complex signal $\phi_i^{E_0}(\lambda)$, specified on a discrete lattice as a function of the lattice site i . E_0 is the energy quantum number specifying the state, and λ is an independent variable. In our simulations, this variable is either μ or V_Z . We seek a function which encapsulates whether or not a signal is localized around some point(s) in the lattice.

Following the formulations in [30], the degree of localization can be modeled by the localization function $A_L^\beta(\lambda)$ for a given set of quantum numbers β . In our case, $\beta = E_0$. The proposed localization function is given by

$$A_L^{E_0}(\lambda) = \frac{1}{L} \sum_{l=1}^L \exp(2\pi i P_l^{E_0}(\lambda)). \quad (9.1)$$

The total number of sites in the system is L , and the phase-factor

$$P_l^{E_0}(\lambda) = \sum_{i=1}^l |\phi_i^{E_0}(\lambda)|^2. \quad (9.2)$$

is expressed as the sum of the absolute square of the signal, summed accumulatively up to and including site l .

By considering some examples of signals, we can get an idea of how well $A_L^{E_0}(\lambda)$ may distinguish between signals in our simulations. Comparing certain signals, one may expect the 'degree of localization' to be widely different. This is illustrated now.

If the wavefunction is completely delocalized, it is a constant as a function of real space, as illustrated in the second plot from the left in figure 9.1a. These are arbitrary signals, thus we omit the E_0 index. In this case, $P_l(\lambda) \propto l/L$ for all l (see the second plot from left in figure 9.1b). Assuming that the number of sites is sufficiently large, the set of all complex numbers $\{exp(2\pi i P_l)\}_l$ will swipe out the whole unit circle in the complex plane, yielding $|A_L| = 0$. See the same column in figure 9.1c, which shows how the real and complex components of A_L accumulates as a function of l .

On the contrary, if the wavefunction is completely localized at one site i_0 ($\phi_i^{E_0}(\lambda) = \delta_{i,i_0}$ is a Kronecker delta), the phase is $P_l(\lambda) = 0$ for $l < i_0$ and $P_l(\lambda) = 1$ for $l \geq i_0$. All these phases contribute with elements $exp(2\pi i P_l) = 1$, such that $|A_L^{E_0}(\lambda)|$ evaluates to 1 (see the first column in figure 9.1 (a) through (c)). For these two examples, $A_L^{E_0}(\lambda)$ is a perfect measure of the degree of localization of the signal $\phi_i^{E_0}(\lambda)$. It assumes the values

$$A_L^{E_0}(\lambda) \begin{cases} = 1, & \text{if completely localized,} \\ = 0, & \text{if completely delocalized,} \end{cases} \quad (9.3)$$

which perfectly reflect our expectations about these signals.

We also want a function that reflects whether a signal is neither completely localized nor delocalized. When the function in eq. (9.1) evaluates to a value between 0 and 1, it may be that the signal is, to a certain extent, delocalized. However, there are some cases where the phase cancels in a symmetrical way, yielding $|A_L| = 0$, even though the signal is not perfectly constant.

Three sinusoidal signals are analyzed in figure 9.1, in the three last columns from the right. We choose to categorize them as being delocalized signals with features. Due to the first two sinusoidal signals (from the left) being half-periodic, $|A_L|$ becomes exactly zero in these cases, because of cancellation that occurs from summing over the phase factor. This exemplifies a potential short-coming of quantifying localization in this way. However, for the sinusoidal signal that is *not* half-periodic, the localization function is finite. We therefore conclude that, although $|A_L^{E_0}(\lambda)|$ seems to quantify

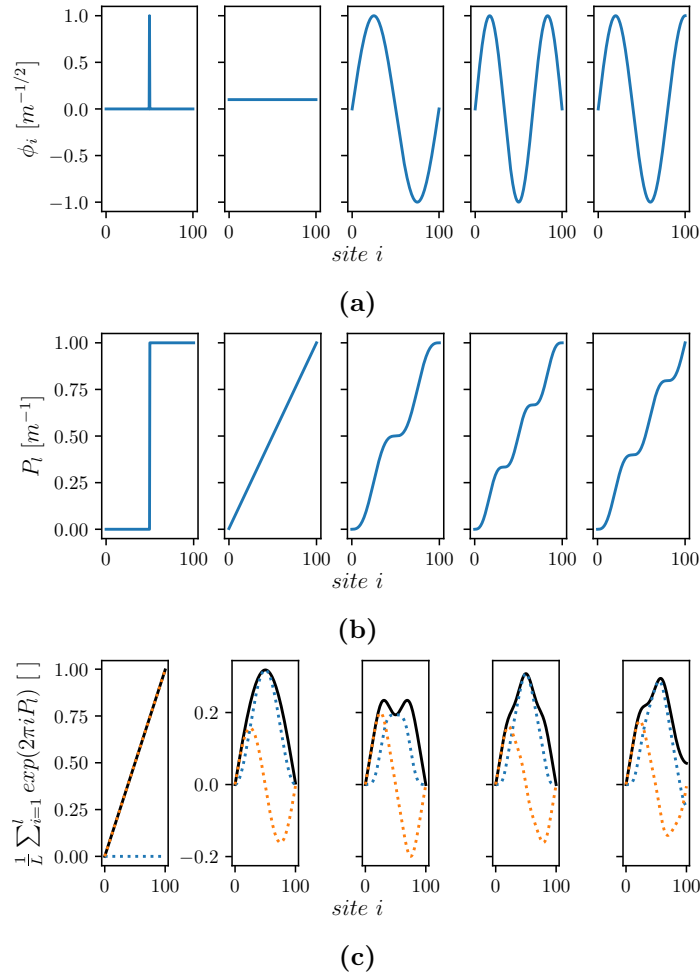


Figure 9.1: (a) Example signals for a non-normalized wavefunction ϕ_i . From left to right ($N = 100$): $\delta_{i,N/2}$ (completely localized, Kronecker-delta function), $i/\sqrt{(N)}$ (completely delocalized), $\sin(2\pi \times i)$, $\sin(1.5 \times 2\pi \times i)$, and $\sin(1.25 \times 2\pi \times i)$, where i is the site index. (b) Phases P_l from the normalized probability density of ϕ_i . (c) Cumulative value of the localization function $|A_L|$ (black line) as higher elements of the sum over sites is performed. The real and complex components are shown in blue and orange dotted lines, respectively. $|A_L|$ is the cumulative function at $i = 100$, and the completely localized (delocalized) signals yield $|A_L| = 1$ (0). The half-periodic sinusoidal signals yield $|A_L| = 0$, while the localization function for the sinusoidal signal that is not half-periodic (right-most plot) is finite.

that a delta-function is localized while a constant function is completely delocalized, it may not be a perfect measure for more complicated functions in general. On the other hand, it does capture delocalized signals, with or without features, when it takes values less than 1.

9.2.2 Probability density in real space

The probability density corresponding to the lowest energy mode E_0 (see figure 8.4) is shown in figure 9.2a and 9.2b for $\lambda = \mu$ and V_Z , respectively. The same parameters are used as in the previous simulations (see for example figure 8.3), but the number of sites used is reduced to $N = 200$ due to computation cost.

Before entering the topological region in *site*, μ -space in figure 9.2a, the lowest energy wavefunction satisfies the boundary conditions by going towards zero at the edges. The probability density largely assumes a single wavelength that is two times the system length.

Inside the topological region, $|\mu| \lesssim 350 \mu eV$, two end-states (red peaks) form near the ends. For larger positive μ -values still inside the topological region, the probability density becomes more 'textured', that is, smaller peaks also form between the end states. Note that the probability density is symmetric around the middle of the wire, because the model Hamiltonian does not distinguish between left and right sides in real space.

The effective topological gap, Δ_{top} , is estimated numerically (gray line). It is calculated by finding the minimum energy of the dispersion in the Oreg-Lutchyn model, given by eq. (4.20), for every value of λ . In devising the algorithm performing this calculation, it was crucial to include the appropriate domain of wave-numbers k that contains all the minima in the dispersion. The resolution in k , as well as the fact that this dispersion is intended to describe an infinite system, are the two main sources of error in the algorithm.

The effective superconducting gap and the localization function (black line) have similar dependencies on μ (figure 9.2c). The localization function $|A_N^{E_0}(\mu)|$ of the probability density is calculated analogously to earlier ($\phi_i^{E_0}(\lambda) = \psi_i^{E_0}(\mu)$ in (9.2)). Close to the two topological phase transitions, Δ_{top} approaches zero, but does not reach exactly zero within the numerical resolution in $\lambda = \mu$ and V_Z . However, the localization function does reach zero within this resolution¹.

For example, on both sides of the first topological phase transition at $\mu_{1,\Delta_{top}} = -357 \mu eV$ for the gap and $\mu_{1,|\psi|^2} = -348 \mu eV$ for the localization, both Δ_{top} and $A_N^{E_0}(\mu)$ monotonically increase until reaching a maximum value. In the topological region, a maximum of $max(\Delta_{top}(\mu)) = 179 \mu eV$ is reached at $\mu = -128 \mu eV$, after which it stays approximately constant (it increases by the order of 1% of $max(\Delta_{top}(\mu))$) until $\mu = 128 \mu eV$. Thereafter, the gap decreases monotonically until a second almost-zero point around the second phase transition at $\mu_{2,\Delta_{top}} = 357 \mu eV$. The localization

¹Note that in these numerical calculations, the numerical resolution in $A_L^{E_0}(\lambda)$ is set by the resolution in μ . Thus, the localization function being zero at $\mu_{1(2),|\psi|^2}$ means it is zero within its uncertainty set by its numerical resolution.

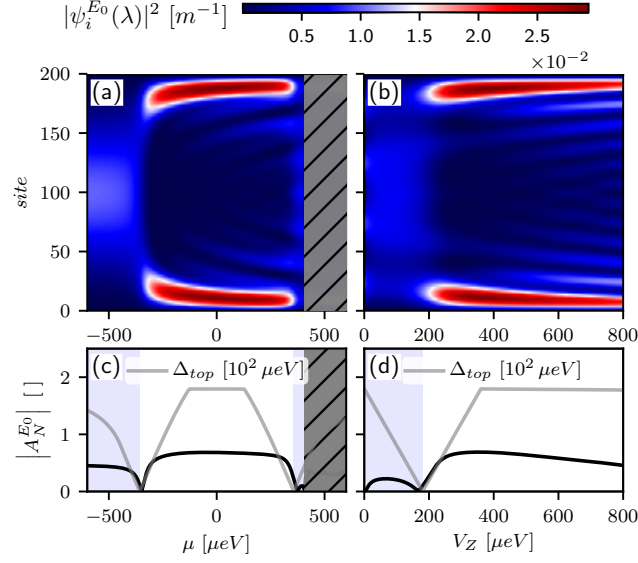


Figure 9.2: The normalized ($\sum_{i=1}^{N=200} |\psi_i^{E_0}(\lambda)|^2 = 1$) probability density $|\psi_i^{E_0}(\lambda)|^2 = |u_{i,\uparrow}^{E_0}(\lambda)|^2 + |u_{i,\downarrow}^{E_0}(\lambda)|^2 + |v_{i,\uparrow}^{E_0}(\lambda)|^2 + |v_{i,\downarrow}^{E_0}(\lambda)|^2$ is plotted in (a) and (b) as a function of site i and $\lambda = \mu, V_Z$. Level-crossings with a higher excited state has occurred in the grey area with black skewed lines. In (c) and (d), $|A_N|$ (black line) quantifies the degree of localization of the wavefunction for a line-cut in site-space at every μ - and V_Z -value. Eq. (9.1) (with $\phi_i^{E_0}(\lambda) = |\psi_i(\lambda)|^2$ in eq. (9.2)) has been implemented, obtaining this. The gray (white) background denotes the normal (topological) region as estimated from the topological gap Δ_{top} (gray line). This gap has been calculated numerically by finding the global minimum energy from the energy dispersion of the Oreg-Lutchyn Hamiltonian given by (4.20), making sure that all minima in the bands were present in the chosen momentum-domain. All model parameters, except the number of sites $N = 200$, is identical to the previous numerical results shown in this chapter.

reaches its maximum value $\max(A_N^{E_0}(\mu)) = 0.68$ at $\mu = -45 \mu\text{eV}$. In the region where this function looks mostly flat, $-200 \mu\text{eV} \lesssim \mu \lesssim 200 \mu\text{eV}$, it changes by about 0.03, or 4% of $\max(A_N^{E_0}(\mu))$. Close to the second phase transition, the localization function becomes zero at $\mu_{2,|\psi|^2} = 375 \mu\text{eV}$. Although the gap and the localization are similar, the latter saturates faster away from the topological phase transition, and it reaches zero at systematically higher chemical potentials (by the order of $10 \mu\text{eV}$).

Also note that the effective topological gap calculated numerically actually does not go completely to zero at the phase transitions. As a function of μ , it reaches its minimum value of $0.24 \mu\text{eV}$ or 0.1% of $\max(\Delta_{top}) = 179 \mu\text{eV}$, and as a function of V_Z , a minimum of $0.53 \mu\text{eV}$ or 0.3% of the same maximal value. Given that a closing

of the gap should signify a topological phase transition, these minima being non-zero could imply that the particular values of the very small minima or zeros found in $|A_N^{E_0}|$ are not so important for discussing whether or not the phase transition occurs. If this is the case, the most important take away from the localization function may be that it has a minimum close to where the phase transition is expected to occur. In what follows, we therefore restrain citing precise values in $|A_N^{E_0}|$.

For higher chemical potentials after the second phase transition, the localization function continues to increase until the lowest eigenenergy crosses with the second lowest one. At that point, the lowest energy eigenstate is a different state with a different localization profile, and should not be compared to the topologically protected lowest energy state. The areas of μ , *site*-space where level crossing has occurred is therefore not shown (gray, striped overlay).

Similarly to in 9.2a, end states form inside the topological region $|V_Z| \gtrsim 200 \mu eV$ (see figure 9.2b). For larger magnetic field, the probability density also becomes more textured. Outside the topological region, the lowest energy state is a superposition of several different frequencies, contrary to in 9.2.a, where it is more or less a single mode.

In figure 9.2d, the gap continues to increase in a linear fashion on both sides of $|V_Z| = 180 \mu eV$, where it has a minimum. For higher fields, it reaches a maximum $\max(\Delta_{top}) = 179 \mu eV$ at $V_Z = 360 \mu eV$, after which it stays approximately constant (it decreases by 1% of $\max(\Delta_{top})$). The localization reaches a maximum value 0.69 at $V_Z = 356 \mu eV$, and decreases significantly thereafter. *Because Δ_{top} stays constant for higher field, it may not be related to the observed decrease in $|A_N^{E_0}|$ for higher fields.*

Given that $|A_N^{E_0}|$ is a reliable measure for localization in this specific case, we may propose that the observed decrease in localization is affected by the total spin-polarization of the system because: As the system becomes more spin-polarized, the topological protection diminishes. In section 9.2.3, we show the spin-polarization, similarly to in figure 9.2. We investigate whether or not the total spin-polarization increases in this region of higher fields, where the localization function decreases.

9.2.3 Spin polarization in real space

Figure 9.3 shows the spin polarization for the same system parameters as before, and with sub-figures similarly as in figure 9.2. In the trivial region in figure 9.3a, the spin polarization is approximately a single mode. In the topological region, the end states are highly spin polarized, while in the bulk, the spin polarization oscillates between both positive and negative values. However, with field as the variable in 9.3b, the spin polarization alternates between positive and negative values as a function of real space in both the topological *and* the trivial region. The finite magnetic field has spin-split the energy band of the system.

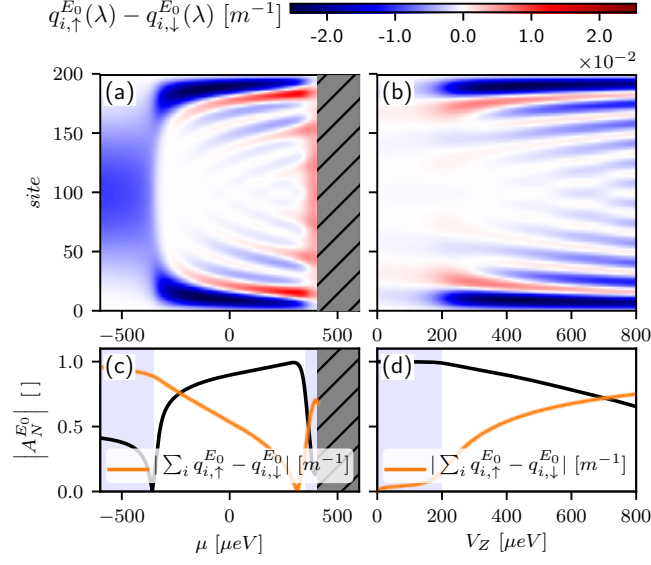


Figure 9.3: The normalized spin polarization $q_{i,\uparrow}^{E_0}(\lambda) - q_{i,\downarrow}^{E_0}(\lambda) = \left| u_{i,\uparrow}^{E_0}(\lambda) \right|^2 - \left| v_{i,\uparrow}^{E_0}(\lambda) \right|^2 - \left(\left| u_{i,\downarrow}^{E_0}(\lambda) \right|^2 - \left| v_{i,\downarrow}^{E_0}(\lambda) \right|^2 \right)$ in real space as a function of μ and V_Z are shown in (a) and (b), respectively. The localization function A_N (black line) of the spin polarization ($\phi_i^{E_0}(\lambda) \equiv q_{i,\uparrow}(\lambda) - q_{i,\downarrow}(\lambda)$ in eq. (9.2)) and the absolute value of the total spin summed over all sites (orange line) are shown in (c) and (d). The sign of the total spin polarization is first negative and then positive after the second topological phase transition in (c), while it is negative for all V_Z in (d).

The localization function of the spin polarization, and the absolute value of the total spin are shown in figure 9.3c and 9.3d as a function of μ and V_Z , respectively. In figure 9.3c, the localization function has a local minimum which is close to the first topological phase transition. At higher μ -values, the spin polarization signal transitions from being approximately single-mode to being multi-mode in real space. At the order of tens of μeV after the second phase transition of the continuous infinite Oreg-Lutchyn model (the interface from the white to the gray area in the figure), the localization has a second non-zero minimum.

In figure 9.3d, the localization function is approximately constant in the trivial region, and decreases steadily for increasing magnetic field in the topological region. Simultaneously with this decrease, the system becomes more negatively spin-polarized.

The key take away from the spin polarization is:

- *Even though the total spin polarization changes significantly as a function of μ inside the topological region, the localization of the probability distribution*

$|\psi_i^{E_0}(\mu)|^2$ does not. This suggests, but cannot verify, that the degree of localization of the wavefunction is independent of the total spin polarization when μ is the independent variable.

- *At the same time as the spin-polarization $|\sum_i q_{i,\uparrow}^{E_0}(V_Z) - q_{i,\downarrow}^{E_0}(V_Z)|$ increases for higher magnetic fields, the localization function of the probability density, $|\psi_i^{E_0}(V_Z)|^2$, decreases.* This supports the argument that the degree of localization of the wavefunction in general should depend on the spin-polarization when V_Z is the independent variable, see (8.40).

In section 9.2.4, the BCS charge is calculated in real space in order to evaluate how well the shift between the local and integrated charges is correlated to localizations in real space.

9.2.4 BCS charge in real space

In section ??, the delocalization of the bound state was suggested to explain the shift between $-dE_0/d\mu$ and Q_R . This was based on the energy dependence on the integrated charge shown in (8.39).

If the local and integrated BCS charges are almost the same, the localization around the local charge is high, and their difference is close to zero. Therefore, one minus this difference should quantify the degree of localization in the similar terms as the localization function $|A_L^{E_0}|$ from eq. (9.1):

$$1 - \left(Q_R + \frac{dE}{d\lambda} \right) \begin{cases} = 1, & \text{if completely localized.} \\ \in (0, 1) & \text{in between completely localized/delocalized.} \\ = 0, & \text{if completely delocalized or in between.} \end{cases} \quad (9.4)$$

If (9.4) overlaps with the localization function $|A_L^{E_0}|$ of the charge signal, these functions may seem to work similarly. If eq. in addition is similar to $|A_L^{E_0}|$ of the probability density (see figure 9.2), this would suggest, but not confirm, that the charge quantity is an appropriate measure of delocalization. Again, we stress that when eq. (9.4) is zero, the wavefunction may still have significant weights away from the ends of the wire.

The charge is plotted in figure 9.4.a and 9.4.b in real space as a function of μ and V_Z , respectively. Up to negligible numerical errors, the global charge $\sum_{i=1}^N Q_i$ overlaps completely with $-dE/d\lambda$ in these calculations (both are not shown). In the normal region, the charge is approximately single-mode and always positive in figure 9.4a, while its sign alternates in the corresponding region in figure 9.4b. In the non-trivial region, depending the given value of μ or V_Z , the charge either oscillates

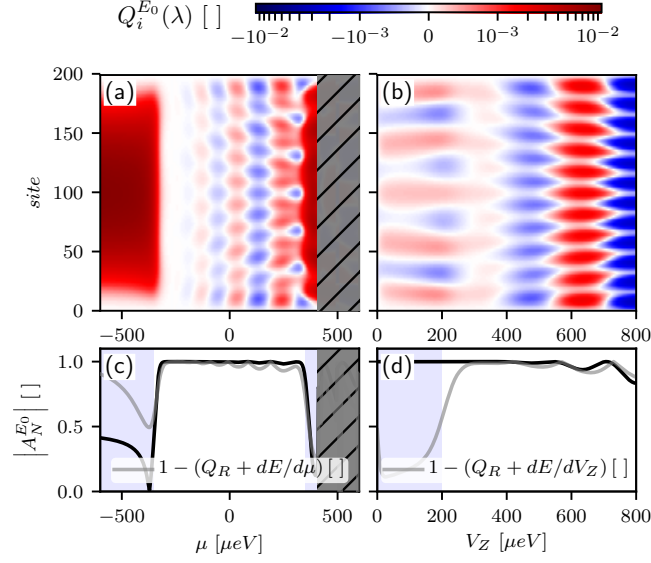


Figure 9.4: BCS charge $Q_i = |u_{i,\uparrow}^{E_0}|^2 + |u_{i,\downarrow}^{E_0}|^2 - |v_{i,\uparrow}^{E_0}|^2 - |v_{i,\downarrow}^{E_0}|^2$ in real space for $i = 1, 2, \dots, N$, $N = 200$ sites, as a function of μ in (a) and of V_Z in (b). The localization function A_N of the charge ($\phi_i^{E_0}(\lambda) \equiv Q_i(\lambda)$ in eq. (9.2)) is shown in black in (c) and (d). Identity minus the deviation between the local charge, Q_R , and the integrated charge, $-dE/d\mu$, is shown as a gray line.

between positive and negative values, or it oscillates, but the sign of the charge does not change. The charge becomes small, but finite, at the ends of the wire.

The localization function of the charge shows similar behavior as that of the probability density in figure 9.2c, and that of the spin polarization in figures 9.3c and 9.3d. In the topological region, it tends to oscillate around a slightly decreasing value. The amplitude of these oscillations also increases with higher values of μ and V_Z .

The alternative localization given by (9.4) (gray line) is similar to the localization function in figure 9.4c, including the oscillatory behavior. For instance, the first and second minima in both the localization function and the charge difference are non-zero numerically and do overlap. However, the charge shift reaches consistently larger values in the trivial regions compared to $A_N^{E_0}(\mu)$.

In figure 9.4d, the localization function $A_N^{E_0}(V_Z)$ stays approximately constant during the topological phase transition, similarly to the case of the spin polarization in figure 9.3d. In the same region, the charge shift (eq. (9.4)) changes significantly and is consistently smaller than $|A_N^{E_0}(V_Z)|$. Thus, the latter may be a better indicator of the topological phase transition than the former in this case.

For all the localization calculations combined:

- *The topological phase transition is associated with a local minimum in the localization function $A_N^{E_0}(\lambda)$, for $\phi_i^{E_0}(\lambda) = \psi_i^{E_0}(\mu)$, $q_{i,\uparrow}^{E_0}(\mu) - q_{i,\downarrow}^{E_0}(\mu)$, $Q_i(\mu)$, and $\psi_i^{E_0}(V_Z)$. However, the localization function for the spin polarization and the charge as a function of V_Z , does not change significantly around the topological phase transition.*
- *The fact that neither the probability density, spin polarization nor the charge is completely localized for any μ or V_Z , suggests that, by probing local quantities at for example the end sites, the information gained should not fully describe integrated quantities, such as $dE/d\lambda$.*

9.2.5 Reconciliation of numerical models: Green's function approach and *Kwant*

In this work, we have used both the Green's function approach, implementing the Weidenmüller formula (see eq. (8.9)), as well as the *Kwant* package. Both approaches are based on the same theoretical machinery, namely solving the scattering problem at the boundaries between a the sample region and the leads.

Apart from small numerical errors, one particular source of apparent inconsistency could stem from how the pincher is implemented. With *Kwant*, the tight-binding parameter for the onsite potential (see eq. (8.42)) at either side of the wire, $t_{\text{site L}}$ and $t_{\text{site R}}$, are increased above the tight-binding parameter for the remaining scattering region, t . In effect, a potential barrier exists on these end sites. The barrier strength is parameterized by $t_{\text{site } \alpha}/t$, which, in turn, alters the reflection and transmission coefficients, as we saw in chapter 3.2 (see for example figure 3.8). The transmission coefficient is also parameterized by the tunneling coupling in the Weidenmüller formula. Therefore, there exists a mathematically rigorous mapping between the strength of the potential barrier, implemented with *Kwant*, and the tunnel coupling in the Green's function approach. Hence, the main source of inconsistency between the particular *Kwant* model, generating the conductance line-cut in figure 8.5, and the other model, generating the data in for instance figure 8.3, should arise due to the difference in discretization, and not due to the rest of the model.

9.3 Conclusion

We have considered a device that is three-terminal, but effectively two-terminal in terms of single particle current for energies below the gap. The S-matrix obeys particle-hole symmetry. The unitarity of the S-matrix gives rise to two conservation laws, for the probability current traveling through a superconducting, one-dimensional

scattering region: one describing the incoming, another describing the outgoing electrons in a given normal lead.

Contrary to a two-terminal device, with one superconducting and one normal lead, the three-terminal setup allows for current, at one end of the wire, to be correlated with the bias applied at the opposite end. (In the real system, this bias is measured between the wire and the grounded superconducting lead.) In other words, a conductance matrix with both local and nonlocal components, can be constructed. Assuming that scattering probabilities are independent of the bias applied to each lead, the non-locality of the current is encoded only in the Fermi-Dirac distribution in the lead opposite to where the current is measured. Hence, the differential conductance $G_{\alpha\beta}$ is always a function of the voltage V_β .

We find that the differential conductance shows distinct symmetries for three-terminal devices with a superconducting scattering region. Setting the left and the right bias voltages equal to one another, and imposing particle-hole symmetry, it follows that the *antisymmetric local* conductance, G_{LL}^{asym} , equals the *antisymmetric non-local* conductance, G_{LR}^{asym} , up to a minus sign. The S-matrix formalism for non-interacting systems is used to calculate the local and nonlocal differential conductance, both analytically and numerically.

The conductance matrix of a single Andreev bound state is probed spectroscopically, and is shown to contain information about the charge at the points where the system is probed. At finite temperature, the conductance peaks of the symmetry-decomposed conductance matrix, is re-shaped by a line function that does not change as a function of energy (μ and V_Z in the Oreg-Lutchyn model). Close to resonance, the non-local conductance is related to the local end charge. Dividing its symmetric ($g_{LR}^{0,sym}(\omega \approx E_0) \propto q_L q_R$) by its antisymmetric ($g_{LR}^{0,asym}(\omega \approx E_0) \times \text{sign}(E_0) \propto q_L n_R$) component, the proportionality factors cancel, yielding only the charge $Q_\alpha \equiv q_\alpha/n_\alpha$ in (8.36). The energy of the Oreg-Lutchyn Hamiltonian derived with respect to the chemical potential, which can be thought of as a global gate along the whole wire, equals the charge of the system, integrated along the length of the gate. Similarly, the energy derived with respect to the energy V_Z is the integrated spin polarization.

The discrete version of the S-matrix is implemented numerically, with two different approaches to solving for the S-matrix: The Green's function approach, and with the *Kwant* package for the *Python* language. The conductance matrix is obtained with both approaches, and show similar results when applied to the three-terminal device. The conductance, mapped in bias- λ space, λ being either the chemical potential or the applied magnetic field, displays a closing of the gap around where the topological phase transition is expected from the Oreg-Lutchyn model of an infinite wire. In the topological region, the near-zero energy modes are gapped. These modes oscillate due to the finite-size effect. The spectroscopic conductance is obtained by tracing the conductance along the eigenenergy obtained from numerically diagonalizing the

Hamiltonian of the closed system. The non-local antisymmetric conductance changes sign near the local maxima in the energy oscillation of the gapped modes. This component alone specifies where the end charge changes sign.

The numerically calculated fraction $g_{LR}^{0,sym}/g_{LR}^{0,asym}$ overlaps with the end charge in the regions where the energy E_0 is much larger than the width of the non-local, antisymmetric conductance (around the energy maxima), and away from the zero-energy crossings. The divergences around the energy peaks, may be removed by decreasing the tunnel coupling to the leads. The divergences at zero-energy crossings are an integral feature of the system.

The energy, obtained by diagonalizing the tight-binding Oreg-Lutchyn Hamiltonian, is a global quantity, while the end charges, either probed by the non-local conductance or calculated from numerical diagonalization, are local. As a result, a non-zero shift in the energy from the charge may quantify the degree of which the near-zero mode wavefunction is localized at the ends of the wire. The shift between the derivative of E_0 and the local charge, is comparable to the result obtained from a toy localization function we introduce. As a function of V_Z , this shift becomes more complicated, and may be a combination of both the delocalization of the probability density, as well as the total spin-polarization of the system. The localization function exhibits a minimum for the real-space signals that change, from being mostly composed of the lowest possible frequency that satisfies the boundary conditions, to a higher frequency signal. For most signals considered (except the spin-polarization and the charge, both versus field), such a minimum appears close to the topological phase transition. The localization function for the probability density, decreases for increasing fields inside the topological region, even though the theoretically predicted effective topological gap (for an infinite, 1D Oreg-Lutchyn Hamiltonian) does not. This decrease could be attributed to the observed increase in spin polarization, which may diminish the effective gap.

9.4 Outlook

9.4.1 Including bias-dependence in the S-matrix.

The symmetry relation $G_{LL}^{0,asym}(V) = -G_{LR}^{0,asym}(V)$, has been demonstrated experimentally in a three-terminal hybrid device [1]. For sub-gap energies (of aluminum), the relation seems to hold slightly better for lower bias voltages. This could suggest that the effective potential in the system was bias-dependent in the experiment. For energies above the gap, the relation continues to deviate increasingly with bias. This may be explained by the fact that quasiparticles are allowed to carry current inside the superconducting lead, which is not captured by our model. In the experiment,

they also observe that the sub-gap energy conductance peaks depend on the plunger. In the numerical model here, the plunger is modeled by the tunnel coupling to the leads, which only changes the width of the conductance peaks, and not the energy of the peaks themselves.

Reverting our attention back to sub-gap energies, there are still some limitations of our model assumptions. When we use the Landauer-Büttiker formalism, we assume that the scattering probabilities (see eq. (5.30)) are energy-independent. As a result, the particle has a constant energy between the points where it enters and leaves the system. In a real system, there may be interaction effects that enables modes to transition between energy channels, for instance as is sketched in figure 9.5.

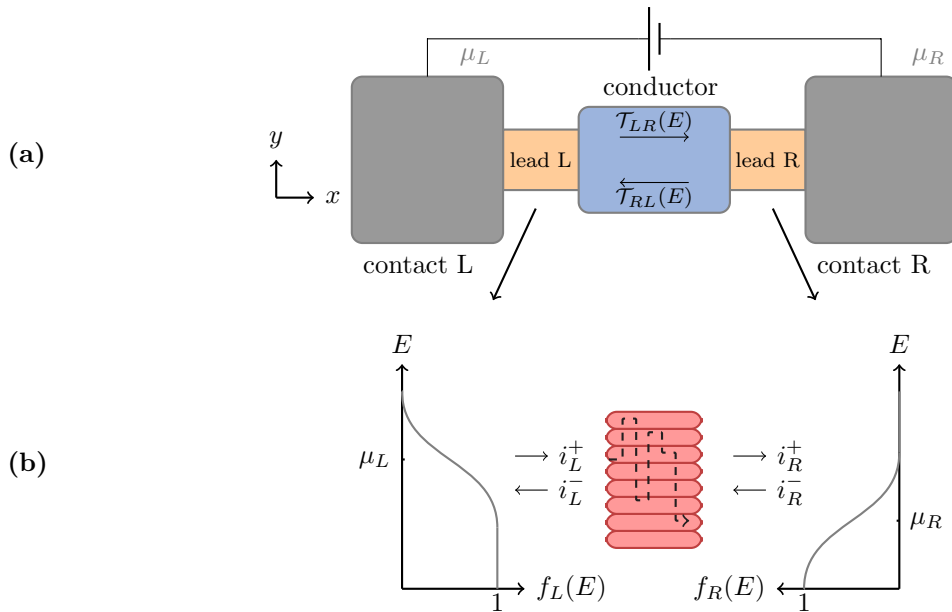


Figure 9.5: (a) A conductor is connected to two reflectionless contacts through leads. The transmission probabilities are energy dependent. (b) Energy distributions of leads at finite temperature. Several energy channels (red boxes) in the conductor can carry current. Dashed line: example of 'vertical flow' between energy channels.

An example where the scattering probabilities are energy-dependent is when an electron increases its energy by absorbing a phonon. This may lead to phonon-assisted tunneling. However, the picture in figure 9.5 only depicts one possible scattering mechanism, when in reality, one has to consider all non-negligible ways in which particles can travel between the leads. In fact, phonon-assisted tunneling may depend on many independent variables, such as biasenergy, temperature and phonon frequency[31].

Another example where increasing the interactions does not necessarily increase the conductance, is a Coulomb blocked system[32]. Strong Coulomb interactions prevents electronic charges from entering the system. Turning on the Coulomb interactions couples different scattering events, that were completely uncoupled in the non-interacting picture. With these interactions, processes where several electrons meet in time and space are very unlikely to take place. In the Landauer-Büttiker formalism, on the other hand, an arbitrary number of particles can scatter off the same point in space and time, as long as they belong to different channels. Therefore, this formalism does not capture the unlikeliness of these processes.

9.4.2 Three-terminal model for energies above the gap

Throughout the numerical simulations in this thesis, we have implemented the effective Hamiltonian, with an effective, proximity-induced superconducting gap. Perhaps, the proximity effect can be demonstrated with transport measurements using *Kwant*. To clarify, consider the low-level system shown in figure 9.6. With this system, one

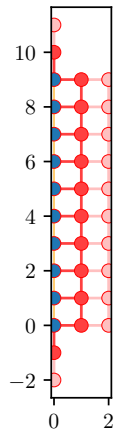


Figure 9.6: The graph of a low-level system, whose scattering region consists of 1D semiconducting onsite and hopping potentials (leftmost blue sites with vertical orange lines between each site), coupled to a 2D superconducting lead (on the right). The two one-dimensional leads are semiconducting.

could experiment with calculating the conductance between the two normal leads, and between one normal and the superconducting lead. One may be able to read off the induced gap inside the wire from the conductance, but not from diagonalizing the closed system.

An advantage of this low-level system, is that it accounts for the quasiparticle current for energies above the gap (see figure 3.8). Therefore, this three-terminal system could be simulated to possibly demonstrate a bias-dependent deviation from the symmetry relation, $G_{LL}^{0,asym}(V) = -G_{LR}^{0,asym}(V)$, as was observed in experiment, for energies above the gap. If a deviation in the symmetry relation is observed in such a simulation, the combination of supercurrent and quasiparticle current in the superconducting lead (see for instance eqs. (3.39) through (3.42)), should explain any such deviation.

9.4.3 Implementing tunnel-coupling to the leads in *Kwant*

The end sites in the effective Green's function model have the same onsite potentials as the rest of the scattering region. It is the tunnel couplings to the leads which are different, in fact smaller, than the hopping terms inside the closed system. This exact kind of pincher implementation is impossible²with *Kwant*, because the scattering region has to end with a site (not a hopping), and the leads are translationally invariant. One could try to circumvent this problem with the following steps, in order:

1. Build the scattering region like usual, but with one extra site on each end where the leads will be attached.
2. Overwrite the last hoppings, on both ends, by a hopping term with t substituted by $\tilde{t} < t$.
3. Overwrite the end sites, on both ends, by an onsite term with t substituted by the tight-binding parameter, t_{leads} , for the leads.
4. Attach normal leads, with onsite and hopping terms given in terms of t_{leads} .

One might wonder which site the end charges should be read off when using this graph. The real end charge, in the sense it has been considered in our analysis so far, should be that of the *second to last* end sites in this closed system. However, the non-local conductance probe would probe the very last sites. If the end sites indeed have the same onsite potential as the leads, there should not be a difference between the wavefunction solutions at this site and in the first site in the leads. However, the boundary condition actually changes: *Kwant* will solve the scattering problem,

²Recall from the code example in figure 6.6 that, in order to define a hopping term, *Kwant* requires two input sites between which the hopping term acts as a tunnel coupling. As far as the author knows, it is not possible to specify a hopping between two sites belonging to different *Builder*-objects in *Kwant v1.4.1*.

with the Dirichlet boundary conditions at the sites on the *outside of the barriers*. In the future, one could construct this type of graph, and see how the charge probed by non-local conductance measurements changes with this slight alteration of boundary conditions.

Appendices

Appendix A

BCS theory

A.1 Expectation value of the number operator

The expectation value of the total number operator, when measured by the BCS ground state, is derived explicitly in the following. The number operator $\hat{N}_{\mathbf{q}\sigma} = c_{\mathbf{q},\sigma}^\dagger c_{\mathbf{q},\sigma}$ quantifies whether or not the electronic state with momentum and spin \mathbf{q}, σ is occupied ($\langle \hat{N}_{\mathbf{q}\sigma} \rangle = 1$) or unoccupied ($\langle \hat{N}_{\mathbf{q}\sigma} \rangle = 0$). Thus, the total number of electrons is the expectation value of the sum

$$\hat{N} = \sum_{\mathbf{q},\sigma} c_{\mathbf{q},\sigma}^\dagger c_{\mathbf{q},\sigma} \hat{N} = 2 \sum_{\mathbf{q}} c_{\mathbf{q}\uparrow}^\dagger c_{\mathbf{q}\uparrow}. \quad (\text{A.1})$$

In the second equality, we have assumed spin symmetry. We seek to measure this number with the BCS ground state given by (2.7), that is, to explicitly calculate

$$\begin{aligned} \langle \hat{N} \rangle &= \langle \psi_{BCS} | \hat{N} | \psi_{BCS} \rangle \\ &= 2 \langle \psi_{BCS} | \sum_{\mathbf{q}} c_{\mathbf{q}\uparrow}^\dagger c_{\mathbf{q}\uparrow} \prod_{\mathbf{k}} (u_{\mathbf{k}} + v_{\mathbf{k}} c_{\mathbf{k}\uparrow}^\dagger c_{-\mathbf{k}\downarrow}^\dagger) | 0 \rangle. \end{aligned}$$

In the following, we adopt the notation $|\psi_{BCS,\mathbf{k}}\rangle = (u_{\mathbf{k}} + v_{\mathbf{k}} c_{\mathbf{k}\uparrow}^\dagger c_{-\mathbf{k}\downarrow}^\dagger) | 0 \rangle$.

Consider the factor in the BCS ground state bra and ket that has the same momentum-index as that in the number operator. Applying those components to the number operator yields a factor

$$2(u_{\mathbf{q}}^* + v_{\mathbf{q}}^* c_{-\mathbf{q}\downarrow} c_{\mathbf{q}\uparrow}) c_{\mathbf{q}\uparrow}^\dagger c_{\mathbf{q}\uparrow} (u_{\mathbf{q}} + v_{\mathbf{q}} c_{\mathbf{q}\uparrow}^\dagger c_{-\mathbf{q}\downarrow}^\dagger).$$

All but the $|v_{\mathbf{q}}|^2 c_{-\mathbf{q}\downarrow} c_{\mathbf{q}\uparrow} c_{\mathbf{q}\uparrow}^\dagger c_{-\mathbf{q}\downarrow}^\dagger$ term measure to zero when they meet the vacuum bra and ket with index \mathbf{q} , because all other terms apply an annihilation operator on the

vacuum. Hence,

$$\begin{aligned}\langle \hat{N} \rangle &= 2 \sum_{\mathbf{q}} |v_{\mathbf{q}}|^2 \left(\prod_{\mathbf{k}' \neq \mathbf{q}} \langle \psi_{BCS, \mathbf{k}'} | \right) \langle 1 |_{-\mathbf{q}\downarrow} \langle 1 |_{\mathbf{q}\uparrow} | 1 \rangle_{\mathbf{q}\uparrow} | 1 \rangle_{-\mathbf{q}\downarrow} \left(\prod_{\mathbf{k} \neq \mathbf{q}} | \psi_{BCS, \mathbf{k}} \rangle \right) \\ &= 2 \sum_{\mathbf{q}} |v_{\mathbf{q}}|^2.\end{aligned}\tag{A.2}$$

The bras and kets with identical momentum and spin indices, have identical occupations, and altogether normalize to 1.

A.2 Variance of the number operator

We seek the variance in the number operator, given by

$$\delta \hat{N}^2 = \langle \hat{N}^2 \rangle - \langle \hat{N} \rangle^2.\tag{A.3}$$

The second term is (A.2) squared. In determining the first term, note that the spin symmetry used in equation (A.1), when squared reads

$$\hat{N}^2 = 4 \sum_{\mathbf{q}, \mathbf{p}} c_{\mathbf{p}\uparrow}^\dagger c_{\mathbf{p}\uparrow} c_{\mathbf{q}\uparrow}^\dagger c_{\mathbf{q}\uparrow}.\tag{A.4}$$

Consider splitting up one of the sums from (A.4) in the expectation value

$$\begin{aligned}\langle \psi_{BCS} | \hat{N}^2 | \psi_{BCS} \rangle \\ = 4 \langle \psi_{BCS} | \left(\sum_{\mathbf{p}=\mathbf{q}} + \sum_{\mathbf{p} \neq \mathbf{q}} \right) \sum_{\mathbf{q}} c_{\mathbf{p}\uparrow}^\dagger c_{\mathbf{p}\uparrow} c_{\mathbf{q}\uparrow}^\dagger c_{\mathbf{q}\uparrow} \prod_{\mathbf{k}} | \psi_{BCS, \mathbf{k}} \rangle.\end{aligned}$$

Evaluating the $\mathbf{p} = \mathbf{q}$ sum is similar to what was done calculating the expectation value of \hat{N} , in that only the $|v_{\mathbf{q}}|^2$ -term is non-zero upon measurement. Now now, there are two, and not one, number-operator like ($c^\dagger c$) factor being measured, that is

$$\begin{aligned}4 (u_{\mathbf{q}}^* + v_{\mathbf{q}}^* c_{-\mathbf{q}\downarrow} c_{\mathbf{q}\uparrow}) c_{\mathbf{q}\uparrow}^\dagger c_{\mathbf{q}\uparrow} c_{\mathbf{q}\uparrow}^\dagger c_{\mathbf{q}\uparrow} (u_{\mathbf{q}} + v_{\mathbf{q}} c_{\mathbf{q}\uparrow}^\dagger c_{-\mathbf{q}\downarrow}^\dagger) \\ = 4 |v_{\mathbf{q}}|^2 (c_{-\mathbf{q}\downarrow} c_{\mathbf{q}\uparrow}) c_{\mathbf{q}\uparrow}^\dagger c_{\mathbf{q}\uparrow} c_{\mathbf{q}\uparrow}^\dagger c_{\mathbf{q}\uparrow} \left(c_{\mathbf{q}\uparrow}^\dagger c_{-\mathbf{q}\downarrow}^\dagger \right).\end{aligned}$$

It makes no difference having this extra number operator, as opposed to having only one of them, when applied to the ket on the right. In fact, having any integer number of such operators with the same quantum numbers multiplied with each other will

not change the measured result. Hence, closing with the whole BCS states, the first sum evaluates to

$$4 \langle \psi_{BCS} | \sum_{\mathbf{p}=\mathbf{q}} \sum_{\mathbf{q}} c_{\mathbf{p}\uparrow}^\dagger c_{\mathbf{p}\uparrow} c_{\mathbf{q}\uparrow}^\dagger c_{\mathbf{q}\uparrow} \prod_{\mathbf{k}} |\psi_{BCS,\mathbf{k}} \rangle = 4 \sum_{\mathbf{q}} |v_{\mathbf{q}}|^2. \quad (\text{A.5})$$

The second sum where $\mathbf{p} \neq \mathbf{q}$ is

$$\begin{aligned} & 4 \sum_{\mathbf{q}} \sum_{\mathbf{p} \neq \mathbf{q}} \langle \psi_{BCS} | c_{\mathbf{p}\uparrow}^\dagger c_{\mathbf{p}\uparrow} c_{\mathbf{q}\uparrow}^\dagger c_{\mathbf{q}\uparrow} | \psi_{BCS} \rangle \\ &= 4 \sum_{\mathbf{q}} \sum_{\mathbf{p} \neq \mathbf{q}} \prod_{\mathbf{k}'} \prod_{\mathbf{k}} \langle 0 | (u_{\mathbf{k}'}^* + v_{\mathbf{k}'}^* c_{-\mathbf{k}'\downarrow} c_{\mathbf{k}'\uparrow}) c_{\mathbf{p}\uparrow}^\dagger c_{-\mathbf{p}\downarrow}^\dagger c_{\mathbf{q}\uparrow}^\dagger c_{-\mathbf{q}\downarrow}^\dagger (u_{\mathbf{k}} + v_{\mathbf{k}} c_{\mathbf{k}\uparrow}^\dagger c_{-\mathbf{k}\downarrow}^\dagger) | 0 \rangle \\ &= 4 \sum_{\mathbf{q}} \sum_{\mathbf{p} \neq \mathbf{q}} |v_{\mathbf{p}}|^2 |v_{\mathbf{q}}|^2. \end{aligned} \quad (\text{A.6})$$

In the second equality, \hat{N} applied to the $\mathbf{k} = \mathbf{q}$ and $\mathbf{k} = \mathbf{p}$ parts of $|\psi_{BCS}\rangle$ yields

$$\begin{aligned} & \prod_{\mathbf{k}=\mathbf{q},\mathbf{p}} c_{\mathbf{p}\uparrow}^\dagger c_{\mathbf{p}\uparrow} c_{\mathbf{q}\uparrow}^\dagger c_{\mathbf{q}\uparrow} (u_{\mathbf{k}} + v_{\mathbf{k}} c_{\mathbf{k}\uparrow}^\dagger c_{-\mathbf{k}\downarrow}^\dagger) | 0 \rangle_{\mathbf{k}} \\ &= v_{\mathbf{q}} v_{\mathbf{p}} c_{\mathbf{p}\uparrow}^\dagger c_{-\mathbf{p}\downarrow}^\dagger c_{\mathbf{q}\uparrow}^\dagger c_{-\mathbf{q}\downarrow}^\dagger | 0 \rangle_{\mathbf{p}\uparrow, -\mathbf{p}\downarrow, \mathbf{q}\uparrow, -\mathbf{q}\downarrow}. \end{aligned}$$

When closed with the corresponding bra for $\mathbf{k}' = \mathbf{q}, \mathbf{p}$, all the operators measure to 1. In order to see this, consider first the case where $\mathbf{k}' = \mathbf{p}$. Only the $v_{\mathbf{k}'}$ -term from the $\langle \psi_{BCS,\mathbf{k}'} |$ survives the measurement when applied to the middle term, yielding

$$|v_{\mathbf{p}}|^2 \langle 0 | c_{-\mathbf{p}\downarrow} c_{\mathbf{p}\uparrow}^\dagger c_{-\mathbf{p}\downarrow}^\dagger | 0 \rangle_{\mathbf{p}\uparrow, -\mathbf{p}\downarrow} = |v_{\mathbf{p}}|^2$$

and similarly ($|v_{\mathbf{q}}|^2$) for the factor where $\mathbf{k}' = \mathbf{q}$. Hence, (A.6) is obtained. In sum, it has been demonstrated that

$$\langle \hat{N}^2 \rangle = 4 \sum_{\mathbf{q}} |v_{\mathbf{q}}|^2 \left(1 + \sum_{\mathbf{p} \neq \mathbf{q}} |v_{\mathbf{p}}|^2 \right) \quad (\text{A.7})$$

by adding up (A.5) and (A.6).

Inserting for (A.2) and (A.7) in the variance given by (A.3), one obtains

$$\begin{aligned} \delta \hat{N}^2 &= 4 \sum_{\mathbf{q}} |v_{\mathbf{q}}|^2 \left(1 + \sum_{\mathbf{p} \neq \mathbf{q}} |v_{\mathbf{p}}|^2 \right) - 4 \sum_{\mathbf{q}'} |v_{\mathbf{q}'}|^2 \sum_{\mathbf{p}'} |v_{\mathbf{p}'}|^2 \\ &= 4 \sum_{\mathbf{q}} |v_{\mathbf{q}}|^2 \left(1 + \sum_{\mathbf{p} \neq \mathbf{q}} |v_{\mathbf{p}}|^2 - \left[\sum_{\mathbf{p}' \neq \mathbf{q}} + \sum_{\mathbf{p}' = \mathbf{q}} \right] |v_{\mathbf{p}'}|^2 \right) \\ &= 4 \sum_{\mathbf{q}} |u_{\mathbf{q}}|^2 |v_{\mathbf{q}}|^2, \end{aligned} \quad (\text{A.8})$$

In the last equality, the $\mathbf{p}, \mathbf{p}' \neq \mathbf{q}$ sums cancel, and the normalization condition $1 - |v_{\mathbf{q}}|^2 = |u_{\mathbf{q}}|^2$ is invoked. As long as there exists at least one \mathbf{q} state in the superposition that is the BCS ground state, for which neither one of the coefficients are zero, the variation in the number operator (A.8) is finite. If for example one of the amplitudes squared is one, the other is necessarily zero. Such a component will not contribute to $\delta \hat{N}^2$, as is the case for energies $\epsilon_{\mathbf{k}}$ far away from ϵ_F , as illustrated in figure 2.3.

A.3 Explicit form of the free energy

Consider the expectation value eq. (2.13). The calculation for the first term is identical to what was done for $\langle \hat{N} \rangle$ (see appendix A.1), apart from the extra $\xi_{\mathbf{k}}$ -factor which resides in the sum of the Hamiltonian eq. (2.9). Therefore, we have

$$\langle \psi_{BCS} | \sum_{\mathbf{k}} \xi_{\mathbf{k}} \left(c_{\mathbf{k}\uparrow}^\dagger c_{\mathbf{k}\uparrow} + c_{\mathbf{k}\downarrow}^\dagger c_{\mathbf{k}\downarrow} \right) | \psi_{BCS} \rangle = 2 \sum_{\mathbf{k}} \xi_{\mathbf{k}} |v_{\mathbf{k}}|^2.$$

First considering the factor of $|\psi_{BCS}\rangle$ with the same index as the fermion operators (denoted \mathbf{p}) in the second term of the Hamiltonian, allows for the simplification (omitting the real $-\Delta_{\mathbf{p}}$ factor and $\sum_{\mathbf{p}}$)

$$\begin{aligned} & \langle \psi_{BCS} | \left(c_{\mathbf{p}\uparrow}^\dagger c_{-\mathbf{p}\downarrow}^\dagger + c_{-\mathbf{p}\downarrow} c_{\mathbf{p}\uparrow} \right) (u_{\mathbf{p}} + v_{\mathbf{p}} c_{\mathbf{p}\uparrow}^\dagger c_{-\mathbf{p}\downarrow}^\dagger) | 0 \rangle_{\mathbf{p}\uparrow, -\mathbf{p}\downarrow} | \psi_{BCS, \mathbf{k} \neq \mathbf{p}} \rangle \\ & = \langle \psi_{BCS} | \left(u_{\mathbf{p}} c_{\mathbf{p}\uparrow}^\dagger c_{-\mathbf{p}\downarrow}^\dagger + v_{\mathbf{p}} \right) | 0 \rangle_{\mathbf{p}\uparrow, -\mathbf{p}\downarrow} | \psi_{BCS, \mathbf{k} \neq \mathbf{p}} \rangle \end{aligned}$$

where $|\psi_{BCS, \mathbf{k} \neq \mathbf{p}}\rangle = \prod_{\mathbf{k} \neq \mathbf{p}} \left(u_{\mathbf{k}} + v_{\mathbf{k}} c_{\mathbf{k}\uparrow}^\dagger c_{-\mathbf{k}\downarrow}^\dagger \right) | 0 \rangle_{\mathbf{k}}$. Only the cross-terms survive, because all other terms annihilate the vacuum. Similarly decomposing $\langle \psi_{BCS} |$, the above expression is $(u_{\mathbf{p}}^* v_{\mathbf{p}} + v_{\mathbf{p}}^* u_{\mathbf{p}})$, using that the BCS kets are normalized to 1. Combining the first and the second terms yields the free energy

$$F = \sum_{\mathbf{k}} \left[\xi_{\mathbf{k}} 2|v_{\mathbf{k}}|^2 - \Delta_{\mathbf{k}} (u_{\mathbf{k}}^* v_{\mathbf{k}} + v_{\mathbf{k}}^* u_{\mathbf{k}}) \right]. \quad (\text{A.9})$$

For simplicity, take $\mu = 0$ and real $u_{\mathbf{k}}$ and $v_{\mathbf{k}}$, for which

$$F = \sum_{\mathbf{k}} \left[\epsilon_{\mathbf{k}} \{ \cos(2\theta_{\mathbf{k}}) + 1 \} - \Delta_{\mathbf{k}} \sin(2\theta_{\mathbf{k}}) \right] \quad (\text{A.10})$$

$\theta_{\mathbf{k}}$ is used to parameterize $u_{\mathbf{k}} = \sin(\theta_{\mathbf{k}})$ and $v_{\mathbf{k}} = \cos(\theta_{\mathbf{k}})$, which ensures that the normalization $u_{\mathbf{k}}^2 + v_{\mathbf{k}}^2 = 1$ holds¹. The identities $2\cos^2(\theta) = \cos(2\theta) + 1$ and

$2\cos(\theta)\sin(\theta) = \sin(2\theta)$ have been inserted for, in anticipation that F is to be derived with respect to $\theta_{\mathbf{k}}$.

Minimizing the free energy

F can be minimized with respect to $\theta_{\mathbf{k}}$ by first setting its first derivative to zero. Hence, for every \mathbf{k} inside the sum in $\partial F/\partial\theta_{\mathbf{k}}$,

$$\tan(2\theta_{\mathbf{k}}) = -\frac{\Delta_{\mathbf{k}}}{\epsilon_{\mathbf{k}}}. \quad (\text{A.11})$$

This enables one to (i) relate the parameter $\theta_{\mathbf{k}}$, and hence also $u_{\mathbf{k}}$ and $v_{\mathbf{k}}$, to (ii) the relevant energy parameters in the BCS theory, $\epsilon_{\mathbf{k}}$ and $\Delta_{\mathbf{k}}$.

(i) Using the trigonometric identity $\tan(x) = \pm\sin(x)/\sqrt{1 - \sin^2(x)}$ and the previously used trigonometric identities, the left-hand side of eq. (A.11) can be expressed in terms of $u_{\mathbf{k}}$ and $v_{\mathbf{k}}$ as follows

$$\begin{aligned} \tan(2\theta_{\mathbf{k}}) &= \pm \frac{2\sin(\theta_{\mathbf{k}})\cos(\theta_{\mathbf{k}})}{\sqrt{1 - 4\sin^2(\theta_{\mathbf{k}})\cos^2(\theta_{\mathbf{k}})}} \\ &= \frac{2u_{\mathbf{k}}v_{\mathbf{k}}}{v_{\mathbf{k}}^2 - u_{\mathbf{k}}^2}. \end{aligned} \quad (\text{A.12})$$

In the second line, we use $1 = u_{\mathbf{k}}^2 + v_{\mathbf{k}}^2$ to complete the square in the denominator.

(ii) Scaling the numerator and denominator on the right-hand side of eq. (A.11) by $E_{\mathbf{k}}$, we may identify

$$2u_{\mathbf{k}}v_{\mathbf{k}} = \frac{\Delta_{\mathbf{k}}}{E_{\mathbf{k}}}, \quad v_{\mathbf{k}}^2 - u_{\mathbf{k}}^2 = -\frac{\epsilon_{\mathbf{k}}}{E_{\mathbf{k}}}. \quad (\text{A.13})$$

Finally, combining the last equality in equation eq. (A.13) with $u_{\mathbf{k}}^2 + v_{\mathbf{k}}^2 = 1$ yields the desired relations for $u_{\mathbf{k}}$ and $v_{\mathbf{k}}$ in eq. (2.14).

A.4 BCS density of states derivation

The density of states

$$d(\omega) = \frac{dn}{d\omega} = \frac{1}{\mathcal{V}} \frac{dN}{d\omega} \quad (\text{A.14})$$

¹For simplicity, $u_{\mathbf{k}}$, $v_{\mathbf{k}}$ and $\Delta_{\mathbf{k}}$ are all assumed to be real numbers when we show the derivation in the next section. For the general case where these parameters are complex numbers, we can perform a rotation (Gauge transformation) in the Hamiltonian and the eigenvector in electron-hole space, $(u_{\mathbf{k}}, v_{\mathbf{k}})^T$. In doing so, gain a complex factor $|\Delta| \rightarrow e^{i\phi}|\Delta|$ and similarly in $v_{\mathbf{k}}$, for which we obtain the same result as eq. (2.14).

is a probability density. Thus, it can be expanded in terms of a sum over the *spectral* probability density $A(\mathbf{k}\sigma, \omega)$ (the spectral function). $k\sigma$ is the quasiparticle momentum and spin, while \mathcal{V} is the volume of the whole system. The spectral function is given by the retarded BCS Green's function. By analytical continuation, the density of states is

$$d(\omega) = \frac{1}{2\pi\mathcal{V}} \sum_{\mathbf{k}\sigma} A(\mathbf{k}\sigma, \omega) \rightarrow -\frac{1}{\pi\mathcal{V}} \sum_{\mathbf{k}\sigma} \text{Im} [\mathcal{G}_{\sigma\sigma}^R(\mathbf{k}, \omega + i\eta)].$$

where the Green's function is the BCS mean-field theory Matsubara Green's function[16, sec. 18.4]. Inserting for the explicit form of the Green's function, $\mathcal{G}_{\sigma\sigma}(\mathbf{k}, \omega + i\eta) = \frac{\omega + i\eta + \xi_{\mathbf{k}}}{(\omega + i\eta)^2 + E_{\mathbf{k}}^2}$, we can write the density of states in the form²

$$d(\omega) = -\frac{1}{\pi\mathcal{V}} \sum_{\mathbf{k}\sigma} \text{Im} \left[\frac{1}{\omega - E_{\mathbf{k}} + i\eta} - \frac{1}{\omega + E_{\mathbf{k}} + i\eta} \right] \frac{\omega + \xi_{\mathbf{k}}}{2E_{\mathbf{k}}}, \quad (\text{A.15})$$

Note that, in d dimensions, $d\mathbf{k} = \frac{(2\pi)^d}{\mathcal{V}}$. In the continuum limit, the sum over momenta can be converted into an energy integral as follows

$$\frac{1}{\mathcal{V}} \sum_{\mathbf{k}} \rightarrow \frac{1}{\mathcal{V}} \frac{1}{d\mathbf{k}} \int d\mathbf{k} = \frac{1}{(2\pi)^d} \int \frac{d\mathbf{k}}{d\xi_{\mathbf{k}}} d\xi_{\mathbf{k}}. \quad (\text{A.16})$$

Inside the energy integral, we can use the identity

$$\frac{1}{x + i\eta} = P \frac{1}{x} - i\pi\delta(x) \quad (\text{A.17})$$

to extract the imaginary component in eq. (A.15), where P is the principal value. Inserting for eq. (A.17) and eq. (A.16) into eq. (A.15), and performing the integral for $\omega < 0$ and $\omega > 0$ separately, yields the final result in eq. (2.16), for all ω .

²Having completed the square in the denominator of $\mathcal{G}_{\sigma\sigma}(\mathbf{k}, \omega + i\eta)$, one may do the following factorization:

$$\frac{\omega + i\eta + \xi_{\mathbf{k}}}{(\omega + E + i\eta)(\omega - E + i\eta)} = \left(\frac{A}{\omega + E_{\mathbf{k}} + i\eta} + \frac{B}{\omega - E_{\mathbf{k}} + i\eta} \right) \frac{\omega + \xi_{\mathbf{k}}}{2E_{\mathbf{k}}}.$$

Multiplying both sides by the full denominator of the left hand side, one can match terms on the left and right hand sides. This yields $A = -B = -1$ and, hence, eq. (A.15).

Appendix B

BTK theory

B.1 Algebraic manipulation leading to eq. (3.28)

First, all u terms in (3.27) are moved to one side, and all v terms to the other side of the equal sign. When both equations are squared, and then all terms are moved to one side, we have avoided making any cross-terms between u and v terms. Setting the equations equal to one another, we have

$$(E - \xi_k)^2 u^2 - \Delta^2 v^2 = (E + \xi_k)^2 v^2 - \Delta^2 u^2.$$

For example re-arranging for

$$u^2 = v^2 [(E + \xi_k)^2 + \Delta^2] / [(E - \xi_k)^2 + \Delta^2]$$

and inserting this into the normalization $u^2 + v^2 = 1$ gives

$$v^2 = \left[1 + \frac{(E + \xi_k)^2 + \Delta^2}{(E - \xi_k)^2 + \Delta^2} \right]^{-1} = \frac{1}{2} \left(1 - \frac{\xi_k}{E} \right) = 1 - u^2,$$

which is equivalent to (3.28).

B.2 Derivation of continuum equation for the probability density current

In order to see this more clearly, consider for example

$$\begin{aligned} \frac{\partial}{\partial t} (f f^\dagger) &= f \frac{\partial f^\dagger}{\partial t} + \frac{\partial f}{\partial t} f^\dagger \\ &= \frac{\hbar}{2im} [f \nabla^2 (f^\dagger) - \nabla^2 (f) f^\dagger] + \frac{\Delta}{i\hbar} (g f^\dagger - f g^\dagger). \end{aligned}$$

In the second line, $\partial f^{(\dagger)}/\partial t$ from the BdG equations eq. (3.24) and eq. (3.25) are inserted. The terms containing $\mu(x)$ and $V(x)$ cancel, as they are completely imaginary and their complex conjugates are added together.

The first two terms are

$$\begin{aligned} & \frac{\hbar}{2im} [f \nabla^2(f^\dagger) + f^\dagger \nabla^2(f)] \\ &= \frac{\hbar}{2im} [\nabla \cdot (f \nabla(f^\dagger)) - \nabla f \cdot \nabla f^\dagger + \nabla \cdot (f^\dagger \nabla(f)) + \nabla f \cdot \nabla f^\dagger] \\ &= \frac{\hbar}{2im} [\nabla \cdot (f \nabla(f^\dagger) - \nabla(f) f^\dagger)] \\ &= \frac{\hbar}{m} \nabla \cdot [Im(f^\dagger \nabla f)]. \end{aligned}$$

In the second term of the first line, the fermion operators f and f^\dagger have been commuted. In the second line, the identity $\phi \nabla^2 \psi = \nabla \cdot (\phi \nabla \psi) - \nabla \phi \cdot \nabla \psi$, for arbitrary wavefunctions ϕ and ψ , is inserted for. Again, the two last terms are commuted, giving an extra minus sign whence the very last term is canceled. Similarly,

$$\frac{\partial}{\partial t} (g g^\dagger) = -\frac{\hbar}{m} \nabla \cdot [Im(g^\dagger \nabla g)] - \frac{\Delta}{i\hbar} (g f^\dagger - f g^\dagger).$$

Hence,

$$\begin{aligned} \frac{\partial P}{\partial t} &= \frac{\partial}{\partial t} (f f^\dagger) + \frac{\partial}{\partial t} (g g^\dagger) \\ &= \frac{\hbar}{m} \nabla \cdot [Im(f \nabla f^\dagger) - Im(g \nabla g^\dagger)], \end{aligned}$$

where the term containing Δ has canceled. From this and the source-less continuum equation eq. (3.35), the probability current is identified as eq. (3.36).

B.3 The explicit probability currents for the scattering processes

For velocities equal to the Fermi velocity, any probability A through D is

$$\text{Probability } X = J_P^X / v_F \tag{B.1}$$

For instance, inserting for the particle momentum q^- at point (6) into the reflected wave in eq. (3.32), the Andreev reflected wavefunction is

$$\psi_{refl}(x) = a \begin{pmatrix} 0 \\ 1 \end{pmatrix} e^{iq^- x}, \text{ thus } f(x) = 0 \text{ and } g(x) = a e^{iq^- x}.$$

In this case, we can see that $|g(x)|^2 = a^*a$. Inserting for the electronic and hole components f and g and their spatial derivatives into the probability current in eq. (3.36) yields

$$J_P^A = -\frac{\hbar q^-}{m}|g(x)|^2 \approx v_F|a|^2. \quad (\text{B.2})$$

$-\hbar q^-/m$ is the velocity of the current, which is assumed to be sufficiently close to the Fermi velocity. Hence,

$$A = J_P^A/v_F = |a|^2. \quad (\text{B.3})$$

Similarly, we obtain

$$J_P^B = v_F|b|^2, \quad \frac{-\hbar q^+}{m} \approx v_F, \quad J_P^{C(D)} = v_F|c(d)|^2 (|u|^2 - |v|^2), \quad \frac{\hbar k^{+(-)}}{m} \approx v_F \quad (\text{B.4})$$

The probability currents for processes scattering into the superconductor, J_P^C and J_P^D , are proportional to the Cooper charge.

B.4 The explicit forms of the probability amplitudes

a through d are found by imposing the boundary conditions of eqs. (3.33),

$$\begin{aligned} \psi_{inc}(0) + \psi_{refl}(0) &= \psi_{trans}(0) \\ \begin{pmatrix} 1 \\ 0 \end{pmatrix} + \begin{pmatrix} b \\ a \end{pmatrix} &= \begin{pmatrix} uc + vd \\ vc + ud \end{pmatrix}, \end{aligned}$$

and (3.34)

$$\begin{aligned} \frac{\partial \psi_{trans}(x)}{\partial x} \Big|_{x=0} - \frac{\partial (\psi_{inc}(x) + \psi_{refl}(0))}{\partial x} \Big|_{x=0} &= \frac{2mH}{\hbar} \psi(0) \\ i \begin{pmatrix} k^+cu - k^-dv - (q^+ - q^+b) \\ k^+vc - k^-ud - (q^-a) \end{pmatrix} &= \frac{2mH}{\hbar} \begin{pmatrix} 1 + b \\ a \end{pmatrix}, \end{aligned}$$

and solving the resulting system of four equations:

$$\begin{pmatrix} 0 & -1 & u & v \\ -1 & 0 & v & u \\ 0 & q^+ - \frac{2mH}{i\hbar} & k^+u & -k^-v \\ -\frac{2mH}{i\hbar} - q^- & 0 & k^+v & -k^-u \end{pmatrix} \begin{pmatrix} a \\ b \\ c \\ d \end{pmatrix} = \begin{pmatrix} 1 \\ 0 \\ q^+ + \frac{2mH}{i\hbar} \\ 0 \end{pmatrix}. \quad (\text{B.5})$$

This set of equations can be solved by for example row-reducing the corresponding augmented matrix to its reduced echelon form¹. Imposing the approximation that all momenta are at the Fermi momentum, the general form of the probability amplitudes are

$$a = \frac{uv}{\gamma} \tag{B.6}$$

$$b = -\frac{(u^2 - v^2)(\hbar^2 Z^2 + i\hbar Z)}{\gamma} \tag{B.7}$$

$$c = \frac{u(1 - i\hbar Z)}{\gamma} \tag{B.8}$$

$$d = \frac{iv\hbar Z}{\gamma}, \tag{B.9}$$

with $\gamma = u^2 + (u^2 - v^2)\hbar^2 Z^2$.

Appendix C

Schrieffer-Wolff second order perturbation theory of the Oreg-Lutchyn Hamiltonian

Consider the second order perturbation theory of the Oreg-Lutchyn Hamiltonian in eq. (4.28), represented by a matrix H in the helical basis:

$$H \approx H^{(0)} + H^{(2)}.$$

$H^{(i)}$ is the i 'th order perturbation. The 0'th order perturbation is the low energy block,

$$H^{(0)} = \begin{pmatrix} \xi_k - \kappa & \Delta_p \\ \Delta_p & -\xi_k + \kappa \end{pmatrix},$$

while each mm' matrix element, $H^{(2)}$, is given by [33, app. B]

$$H_{mm'}^{(2)} = \frac{1}{2} \sum_l H_{ml}^{\text{off-diag}} H_{lm'}^{\text{off-diag}} \left(\frac{1}{E_m - E_l} + \frac{1}{E_{m'} - E_l} \right). \quad (\text{C.1})$$

$H_{ml}^{\text{off-diag}}$ is the off-diagonal, ml matrix element of H , where $m \neq l$. The sum over l runs over all elements, except m . E_m is the diagonal, mm element, which corresponds to one of the helical energy bands in this case. This second-order perturbation corrects for perturbations with the low-energy sector, spanned by $\{e^-, h^-\}$, to and back from the higher-energy sector, spanned by $\{e^+, h^+\}$. Carefully applying eq. (C.1) to H yields

$$H^{(2)} = \begin{pmatrix} \frac{\Delta_s^2}{2\xi_k} & 0 \\ 0 & -\frac{\Delta_s^2}{2\xi_k} \end{pmatrix}.$$

Define the high-field limit as $V_Z \gg \alpha_R k$. The diagonal terms in $H^{(2)}$, $\frac{\Delta_s^2}{2\xi_k} \approx \frac{\Delta^2}{2\xi_k}$, are constants as a function of the field. The diagonal terms of $H^{(0)}$, on the other hand, contain κ , which approximates to $|V_Z|$ in said limit. Since these latter terms blow up, while the diagonal terms in $H^{(2)}$ are constants as a function of the field, the system is approximately described by the lower-energy sector, $H^{(0)}$, in the high-field limit, as long as $|V_Z| \gg \frac{\Delta^2}{2\xi_k}$.

Appendix D

S-matrix of a scattering region connected wide-band leads

We outline the derivation of the S-matrix for a general scattering region, attached with an arbitrary number of normal leads. The approach used is based on [29].

The proximitized wire is described by the total Hamiltonian

$$H = H_S + H_{leads} + H_T \quad (\text{D.1})$$

where H_S is the Hamiltonian of the scattering region, H_{leads} that of the metallic leads and H_T is the tunneling Hamiltonian between the two. In this derivation, we assume both systems can be described by an effective, non-interacting theory, with fermionic excitations.

In the wide-band limit, we may linearize the lead Hamiltonian around the Fermi wavevector. That is, Taylor-expanding in small $|k - k_F| \ll k_F$ around k_F , we have

$$H_{leads} = \sum_{j=1}^{N_{ch}} \int \frac{dk}{2\pi} \frac{k^2}{2m} \psi_j^\dagger(k) \psi_j(k) \approx v_F \sum_{j=1}^{N_{ch}} \int \frac{dk}{2\pi} k \psi_j^\dagger(k) \psi_j(k),$$

where $\psi_j(k)$ are fermion operators in the lead. We assume the unit $\hbar = 1$ throughout this calculation. Every channel $j = 1, 2, \dots, N_{ch}$ incorporates both the transverse mode index, the lead index and the spin index. The deviation k from the Fermi wavevector is assumed to be identical for each channel.

With roman letter indices for the leads, and Greek letter indices for the system, the tunneling Hamiltonian between the system and the leads is

$$H_T = \sum_{j=1}^{N_{ch}} \sum_{\tilde{\alpha}=1}^M \int \frac{dk}{2\pi} \left[W_{\tilde{\alpha}j} \psi_{\tilde{\alpha}}^\dagger \psi_j(k) + h.c. \right],$$

where M is the number of channels in the closed system, and $W_{\tilde{\alpha}j}$ is a general matrix element parametrizing the tunnel coupling between channel $\tilde{\alpha}$ in the system and channel j in the leads. $\tilde{\alpha}$ is also a composite index, comprised from transverse mode, lead, and spin indices.

We obtain a Schrödinger equation

$$\epsilon \psi_{j(\tilde{\alpha})}(x) = H \psi_{j(\tilde{\alpha})}(x) \quad (\text{D.2})$$

by applying the Fourier transformed lead (scattering region) wavefunctions, $\psi_{j(\tilde{\alpha})}(k)$, to the total Hamiltonian in eq. (D.1). At $x \neq 0$, the Schrödinger equation for the leads reduces to a simple differential equation, whose solution is a left-moving plane wave with wave-vector $k = v_F/\epsilon$ [29, eq. (C.5)]. Assuming the leads are perfectly transmitting, the combined scattering matrix for all leads is identity: every particle stays inside the same channel throughout the leads. A second simplification arises from assuming the tunnel coupling is only present at $x = 0$, that is, at the interfaces between the scattering region and the leads. Thus, the scattering matrix for the scattering region is given by identity when $x \neq 0$. Hence, the lead wavefunction solutions assume the simple form

$$\psi_j(x) = \begin{cases} e^{-ikx} \sum_l a_l^{out} & \text{for } x < 0, \\ \frac{\psi(0^+) + \psi(0^-)}{2} & \text{at } x = 0, \\ e^{-ikx} \sum_l a_l^{in} & \text{for } x > 0, \end{cases} \quad (\text{D.3})$$

where

$$a_i^{out} = \sum_{j=1}^{N_{ch}} S_{ij} a_j^{in} \quad (\text{D.4})$$

is the outgoing scattering amplitude in channel i , which is the sum over all incident scattering amplitudes in channels j , weighed by the probability amplitude of scattering from channel j to i . Inserting for eq. (D.3) into both Schrödinger equations from eq. (D.2), the system of two equations can be solved for a_i^{out} . Bringing the expression for this amplitude on the form in eq. (D.4), the S-matrix can be read off, obtaining the $N_{ch} \times N_{ch}$ dimensional S-matrix:

$$S = 1 - 2\pi i \nu W^\dagger (\epsilon - H + i\pi \nu W W^\dagger)^{-1} W. \quad (\text{D.5})$$

Bibliography

- [1] G. C. Ménard, G. L. R. Anselmetti, E. A. Martinez, D. Puglia, F. K. Malinowski, J. S. Lee, S. Choi, M. Pendharkar, C. J. Palmstrøm, K. Flensberg, C. M. Marcus, L. Casparis, and A. P. Higginbotham. Conductance-matrix symmetries of a three-terminal hybrid device. *arXiv e-prints*, page arXiv:1905.05505, May 2019.
- [2] Esben Bork Hansen. *Majorana Bound States in Semiconductor-Superconductor Hybrid Devices*. PhD thesis, 2018.
- [3] Anna Birk Hellenes. Online repository containing scripts used in this thesis. See the README file for details. Sep 2019. DOI: 10.5281/zenodo.3380178.
- [4] A. Yu Kitaev. 6. QUANTUM COMPUTING: Unpaired Majorana fermions in quantum wires. *Physics Uspekhi*, 44(10S):131, Oct 2001.
- [5] Jason Alicea. New directions in the pursuit of Majorana fermions in solid state systems. *Reports on Progress in Physics*, 75(7):076501, Jul 2012.
- [6] Martin Leijnse and Karsten Flensberg. Introduction to topological superconductivity and Majorana fermions. *Semiconductor Science Technology*, 27(12):124003, Dec 2012.
- [7] Michael Hell, Martin Leijnse, and Karsten Flensberg. Two-Dimensional Platform for Networks of Majorana Bound States. *Physical Review Letters*, 118(10):107701, Mar 2017.
- [8] Liang Fu and C. L. Kane. Superconducting proximity effect and majorana fermions at the surface of a topological insulator. *Phys. Rev. Lett.*, 100:096407, Mar 2008.
- [9] Gal Harari, Miguel A. Bandres, Yaakov Lumer, Mikael C. Rechtsman, Y. D. Chong, Mercedeh Khajavikhan, Demetrios N. Christodoulides, and Mordechai Segev. Topological insulator laser: Theory. *Science*, 359(6381), 2018.

- [10] Tudor D. Stanescu, Roman M. Lutchyn, and S. Das Sarma. Majorana fermions in semiconductor nanowires. *Phys. Rev. B*, 84:144522, Oct 2011.
- [11] Yuval Oreg, Gil Refael, and Felix von Oppen. Helical liquids and majorana bound states in quantum wires. *Phys. Rev. Lett.*, 105:177002, Oct 2010.
- [12] Roman M. Lutchyn, Jay D. Sau, and S. Das Sarma. Majorana fermions and a topological phase transition in semiconductor-superconductor heterostructures. *Phys. Rev. Lett.*, 105:077001, Aug 2010.
- [13] Jay D. Sau, Roman M. Lutchyn, Sumanta Tewari, and S. Das Sarma. Generic new platform for topological quantum computation using semiconductor heterostructures. *Phys. Rev. Lett.*, 104:040502, Jan 2010.
- [14] C. Moore, Chuanchang Zeng, T. D. Stanescu, and Sumanta Tewari. Quantized zero bias conductance plateau in semiconductor-superconductor heterostructures without non-Abelian Majorana zero modes. *arXiv e-prints*, page arXiv:1804.03164, Apr 2018.
- [15] Jeroen Danon, Anna Birk Hellenes, Esben Bork Hansen, Lucas Casparis, Andrew P. Higginbotham, and Karsten Flensberg. Nonlocal conductance spectroscopy of Andreev bound states: Symmetry relations and BCS charges. *arXiv e-prints*, page arXiv:1905.05438, May 2019.
- [16] Henrik Bruus and Karsten Flensberg. *Many-body quantum theory in condensed matter physics - an introduction*. Oxford University Press, United States, 2004.
- [17] J. Bardeen, L. N. Cooper, and J. R. Schrieffer. Theory of superconductivity. *Phys. Rev.*, 108:1175–1204, Dec 1957.
- [18] C. Kittel. *Introduction to Solid State Physics*. Wiley, 2004.
- [19] A. I. Kiselev, L. A. Akashev, and V. I. Kononenko. Effective electron mass in melts of aluminum, cerium, and Al-3 at.% Ce binary system. *Technical Physics*, 49(3):302–305, Mar 2004.
- [20] Morten Kjærgaard. *Proximity Induced Superconducting Properties in One and Two Dimensional Semiconductors*. PhD thesis, Niels Bohr Institute, 2015.
- [21] G. E. Blonder, M. Tinkham, and T. M. Klapwijk. Transition from metallic to tunneling regimes in superconducting microconstrictions: Excess current, charge imbalance, and supercurrent conversion. *Phys. Rev. B*, 25:4515–4532, Apr 1982.

- [22] D.J. Griffiths. *Introduction to Quantum Mechanics*. Pearson international edition. Pearson Prentice Hall, 2005.
- [23] Alexander Altland and Martin R. Zirnbauer. Nonstandard symmetry classes in mesoscopic normal-superconducting hybrid structures. *Physical Review B*, 55(2):1142–1161, Jan 1997.
- [24] Supriyo Datta. *Electronic Transport in Mesoscopic Systems*. Cambridge Studies in Semiconductor Physics and Microelectronic Engineering. Cambridge University Press, 1995.
- [25] Leonard I. Schiff. *Quantum mechanics / Leonard I. Schiff*. McGraw-Hill New York, 3rd ed. edition, 1968.
- [26] J. J. Sakurai and Jim Napolitano. *Modern Quantum Mechanics*. Cambridge University Press, 2 edition, 2017.
- [27] Christoph W Groth, Michael Wimmer, Anton R Akhmerov, and Xavier Waintal. Kwant: a software package for quantum transport. *New Journal of Physics*, 16(6):063065, jun 2014.
- [28] Timothy A. Davis, Sivasankaran Rajamanickam, and Wissam M. Sid-Lakhdar. A survey of direct methods for sparse linear systems. *Acta Numerica*, 25:383–566, 2016.
- [29] I. L. Aleiner, P. W. Brouwer, and L. I. Glazman. Quantum effects in Coulomb blockade. *Physics Reports*, 358(5-6):309–440, Mar 2002.
- [30] Longyan Gong, Wenjia Li, Shengmei Zhao, and Weiwen Cheng. A measure of localization properties of one-dimensional single electron lattice systems. *Physics Letters A*, 380(1):59 – 64, 2016.
- [31] A. Khedri, V. Meden, and T. A. Costi. Influence of phonon-assisted tunneling on the linear thermoelectric transport through molecular quantum dots. *Physical Review B*, 96(19):195156, Nov 2017.
- [32] K. Miyaji and T. Hiramoto. 5.08 - silicon single electron transistors operating at room temperature and their applications. In Pallab Bhattacharya, Roberto Fornari, and Hiroshi Kamimura, editors, *Comprehensive Semiconductor Science and Technology*, pages 340 – 382. Elsevier, Amsterdam, 2011.
- [33] Roland Winkler. *Spin-orbit coupling effects in two-dimensional electron and hole systems*. Springer tracts in modern physics. Springer, Berlin, 2003.